AD-A257 762

②

THE ROCKET ELECTRIC FIELD SOUNDING (REFS) PROGRAM: PROTOTYPE DESIGN AND SUCCESSFUL FIRST LAUNCH

J. C. Willett   R. K. Longstreth   J. J. Jones
D. C. Curtis   W. Rison
A. R. Driesman   W. P. Winn

DTIC
S ELECTE D
OCT 2 3 1992
C

15 January 1992

92-28298

PHILLIPS LABORATORY
DIRECTORATE OF GEOPHYSICS
AIR FORCE SYSTEMS COMMAND
HANSCOM AIR FORCE BASE, MA 01731-5000

92 10 27 088

"This technical report has been reviewed and is approved for publication"

Arnold C. Barnes, Jr., Acting
for DONALD D. GRANTHAM
Branch Chief

Donald F. Chisholm for RAMc
ROBERT A./McCLATCHEY
Division Director

This document has been reviewed by the ESD Public Affairs Office (PA) and is releasable to the National Technical Information Service (NITS).

Qualified requesters may obtain additional copies from the Defense Technical Information Center. All others should apply to the National Technical Information Service.

If your address has changed, or if you wish to be removed from the mailing list, or if the addressee is no longer employed by your organization, please notify PL/IMA, Hanscom AFB, MA 01731-5000. This will assist us in maintaining a current mailing list.

Do not return copies of this report unless contractual obligation or notices on a specific document requires that it be returned.

REPORT DOCUMENTATION PAGE

Public reporting for this collection of information is estimated to average 1 hour per response, including the time for reviewing instructions, searching existing data sources, gathering and maintaining the data needed, and completing and reviewing the collection of information. Send comments regarding this burden estimate or any other aspect of this collection of information, including suggestions for reducing this burden, to Washington Headquarters Services, Directorate for Information Operations and Reports, 1215 Jefferson Davis Highway, Suite 1204, Arlington, VA 22202-4302, and to the Office of Management and Budget, Paperwork Reduction Project (0704-0188), Washington, DC 20503.

1. AGENCY USE ONLY (Leave blank)	2. REPORT DATE 15 January 1992	3. REPORT TYPE AND DATES COVERED Scientific Dec 89 - Sep 91

4. TITLE AND SUBTITLE

The Rocket Electric Field Sounding (REFS) Program: Prototype Design and Successful First Launch

5. FUNDING NUMBERS

PE 61101F
ILIROB1

PE62101F
66701211

6. AUTHOR(S)

J.C. Willett, D.C. Curtis, A.R. Driesman, R.K. Longstreth, W. Rison*, W.P. Winn*, and J.J. Jones*

7. PERFORMING ORGANIZATION NAME(S) AND ADDRESS(ES)

Phillips Laboratory, GPAA
Hanscom AFB, MA 01731-5000

8. PERFORMING ORGANIZATION REPORT NUMBER

PL-TR-92-2015
IP. No. 342

9. SPONSORING/MONITORING AGENCY NAME(S) AND ADDRESS(ES)

10. SPONSORING/MONITORING AGENCY REPORT NUMBER

11. SUPPLEMENTARY NOTES

* New Mexico Institute of Mining and Technology, Socorro, NM 87801

12a. DISTRIBUTION/AVAILABILITY STATEMENT

Approved for Public Release,
Distribution Unlimited

12b. DISTRIBUTION CODE

13. ABSTRACT (Maximum 200 words)

The motivation, design, and successful first flight of a sounding rocket to measure profiles of vector electrostatic field in the lower troposphere are described. The design employs eight shutter field mills and a corona-charging system in a manner similar to aircraft previously instrumented for the measurement of electric fields. A rocket offers significant advantages over an aircraft in simplicity and calibration. A single cylindrical rotor covering most of the payload acts as the shutter for all eight mills in this design. The cylindrical symmetry and circular cross section of the vehicle facilitate straightforward calibration. Also included in the payload are a pressure sensor, a longitudinal accelerometer, a transverse magnetometer, and a novel cloud-penetration detector. A fair-weather test flight at the NASA Wallops Flight Facility demonstrated the workability of the basic design and identified a few necessary modifications.

14. SUBJECT TERMS

Lightning, Field mills, Triggered lightning, Rocket, Electric fields

15. NUMBER OF PAGES

126

16. PRICE CODE

17. SECURITY CLASSIFICATION OF REPORT	18. SECURITY CLASSIFICATION OF THIS PAGE	19. SECURITY CLASSIFICATION OF ABSTRACT	20. LIMITATION OF ABSTRACT
Unclassified	Unclassified	Unclassified	SAR

NSN 7540-01-280-5500

Standard Form 298 (rev. 2-89)
Prescribed by ANSI Std Z39-18
298-102

Preface

The authors extend sincere thanks to Peter Martini and his expert crew at NASA/WFF for their help in achieving a successful test flight. The WFF radar and telemetry operators deserve special mention for their superb job of acquiring our small and rapidly accelerated vehicle. SSgt. James Anderson of PL/LC did much of the assembly and testing of the payloads and was an invaluable participant in the field deployment to WFF. Michelle Champion of RADC designed a first-rate telemetry antenna for the payload, and the Physical Science Laboratory of NMSU measured its radiation pattern. Wentworth Institute did an excellent job of mechanical layout and construction. Capt. Carl Frushon of PL/LC and Dr. George Jumper of Worchester Polytechnic Institute helped with the aerodynamic and trajectory analysis. William Jafferis of KSC lent invaluable support and encouragement. Funding for this effort was provided in part by the Air Force Office of Scientific Research.

DTIC QUALITY INSPECTED 2

Accession For

NTIS CRA&I	☑
DTIC TAB	☐
Unannounced	☐
Justification	

By

Distribution/

Availability Codes

| Dist | Avail and/or Special |

A-1

Dedication

This report is dedicated to the memory of J.J. (Dan) Jones, whose death in an automobilie accident on November 15, 1991, was a shock to us all. Dan's enthusiasm, energy, and good nature made him a pleasure to work with and an asset to any project. He will be sorely missed.

Contents

Illustrations

Tables

The Rocket Electric Field Sounding (REFS) Program: Prototype Design and Successful First Launch

1. INTRODUCTION

1.1 Background

The physics of lightning in general, and of triggered lightning in particular, is not understood. "Triggering" is defined here as the artificial (intentional or inadvertent) initiation of a lightning discharge by the rapid introduction of a conducting body into a region of high electrostatic field. A triggered discharge begins with a "leader" -- a self-propagating, highly ionized channel extending into virgin air -- initiated at, and propagating away from, the triggering object. Inadvertent triggered lightning is a severe threat to aerospace operations, as illustrated by the Atlas/Centaur-67 disaster[1] on March 26, 1987. On this occasion an un-manned booster carrying a Navy communications satellite was destroyed as the result of a direct lightning strike about 49 seconds after launch from the Eastern Test Range at Cape Canaveral, Florida. It is now known that the vast majority of lightning strikes to aircraft and missiles in flight are triggered.[2,3]

[1] NASA Goddard Space Flight Center (1987) Atlas/Centaur-67 FLTSATCOM F-6 Investigation Board, Report, NASA Goddard Space Flight Center, Greenbelt, MD 20771, 15 July 1987.

[2] Mazur, V., Fisher, B.D., and Gerlach, J.C. (1984) Lightning Strikes to an airplane in a thunderstorm, *J. Aircraft*, 21:607-611.

1

In reaction to the A/C-67 incident, a new set of launch-commit criteria (LCC) was designed to minimize the danger of triggered lightning.[4] In the absence of either operational systems to measure electric fields aloft or knowledge of precise "triggering thresholds" for individual launch vehicles, these constraints were written in terms of the meteorological conditions that have been observed to be associated with electrification and the field intensity measured at the ground. The new LCC are therefore quite conservative. Now that these rules have been imposed on both manned and un-manned operations at all test ranges, there is concern that the ability to launch will be unduly restricted, especially at the Cape, where electrification can occur in all seasons.

In an effort to improve this situation, the joint USAF/NASA Airborne Field Mill (ABFM) Program is now developing an instrumented aircraft to survey the electrostatic fields aloft in support of launch operations[5,6]. This platform will enable electrified clouds to be positively identified and the meteorological indicators of electrification to be better defined. To develop less conservative launch constraints that take maximum advantage of ABFM data, however, we still need to determine necessary and/or sufficient conditions for triggered lightning. Here, we envision electrostatic field thresholds like those proposed by Heritage [1988, Figure 7.1],[4] but tailored for specific vehicles and justified by actual measurements of triggering conditions. This cannot be accomplished by the ABFM alone.

Techniques to intentionally trigger lightning with small rockets towing either grounded ("classical" triggering) or un-grounded ("altitude" triggering) conducting wires are well worked out.[7,8] Classical triggering normally begins with a positively charged leader propagating upward from the tip of the grounded rocket into the upward-directed electric field beneath a thunderstorm. This technique has permitted direct measurements of currents at the channel base [9] and high resolution, time-resolved photographs of luminous processes[10] in cloud-to-

3   Boulay, J.L., J.P. Moreau, A. Asselineau, and P.L. Rustan, Analysis of recent in-flight lightning measurements on different aircraft, paper presented at the International Aerospace and Ground Conference on Lightning and Static Electricity, National Oceanic and Atmospheric Administration, Oklahoma City, OK, April, 1988.

4   Heritage, H., (1988) *Launch vehicle lightning/atmospheric electrical constraints post-Atlas/Centaur 67 incident*, Report No. TOR-0088(3441-45)-2, The Aerospace Corporation, El Segundo, CA 90245.

5   Bailey, J., D.M. Mach, and H.J. Christian (1990) *In flight vector calibration of shutter type field mills aboard a Lear 28/29 aircraft*, presented at the Fall Annual Meeting of the American Geophysical Union, Dec. 4, 1990, San Francisco, CA.

6   Mach, D.M., and H.J. Christian, Initial Electrification of a Florida cumulus, presented at the Fall Annual Meeting of the American Geophysical Union, Dec. 4, 1990, San Francisco, CA.

7   Fieux, R.P., C.H. Gary, B.P.Hutzler, A.R. Eybert-Berard, P.L. Hubert, A.C. Meesters, P.H. Perroud, J.H. Hamelin, and J.M. Person, (1978) *Research on artificially triggered lightning in France*, IEEE Trans. Power Appar. Syst., **PAS-97**:725-733, 1978.

8   Laroche, P., A. Eybert-Berard, and L. Barret, (1985) Triggered lightning flash characterization, in *Tenth International Aerospace and Ground Conference on Lightning and Static Electricity (ICOLSE), Paris*, pp.231-239, Les Editions de Physique, Les Ulis, France..

9   Leteinturier, C., C. Weidman, and J. Hamelin, (1990) Current and electric field derivatives in triggered lightning return strokes, *J. Geophys. Res.*, **95**:811-828, 1990.

ground lightning. Nearly all the quantitative leader observations to date have been made on classically triggered positive leaders, although negatively charged leaders can occasionally be produced by this technique in high fields of "fair-weather" polarity.

Altitude triggering produces leaders of both polarities, although the ungrounded wire, whose lower end can be 100 m or more above the ground, does not afford direct access to the currents flowing in these events. Altitude-triggered lightning begins with a positive leader propagating upward into the cloud from the tip of the rocket, followed after a few milliseconds by a negative leader propagating downward toward the ground from the bottom end of the wire.[11] This technique is believed to simulate triggered strikes to aerospace vehicles, which apparently also begin with a positive leader.[12] Unfortunately, little supporting data is available on the meteorological or atmospheric-electrical conditions in which lightning can or cannot be triggered by any of these techniques.

1.2   Triggering Conditions

The most important missing data on triggering conditions is the ambient electrostatic field distribution into which a lightning leader develops. An electrostatic energy density is associated with this field[13] and is the energy source for the ionization and gas heating involved in creating the leader channel. Together with the physical properties of the (atmospheric) gas and the boundary conditions imposed by nearby conducting objects, this energy distribution determines the occurrence and phenomenology of the resulting breakdown.

Since classical triggering is normally initiated by the same process (the positive leader) as both aircraft- and altitude-triggered flashes, it affords an ideal opportunity to study triggering under semi-controlled conditions. Classical rockets usually initiate a discharge only one or two hundred meters above the ground. At these altitudes, the leader is visible to optical instrumentation and develops in an electric field that is essentially vertical, thus, horizontally homogeneous. Unfortunately, little is known at present about the magnitude and spatial extent of the fields required for classical triggering.

The electrostatic field intensity is monitored at the surface during triggering operations to determine when to launch the rockets. One might expect this parameter to yield a useful triggering threshold. Surprisingly, however, classical rockets normally trigger when the surface field magnitude is only a few kilovolts per meter, as illustrated in Figure 1 [W. Jafferis,

---

[10]   Idone, V.P., R.E. Orville, P. Hubert, L. Barret, and A. Eybert-Berard, Correlated observations of three triggered lightning flashes, *J. Geophys. Res.*, 89:1385-1394, 1984.

[11]   Laroche, P., A. Boudiou, A. Eybert-Berard, L. Barret, J.P. Berlandis, G. Terrier, and W. Jafferis, (1989) Lightning flashes triggered in altitude by the rocket and wire technique, paper presented at the International Conference on Lightning and Static Electricity, Ministry of Defense Procurement Executive, U.K., Bath, England, Sept., 1989.

[12]   Mazur, V., (1988) Lightning initiation on aircraft in thunderstorms, paper presented at the 26th AIAA Meeting, Reno, NV, Jan., 1988.

[13]   Jackson, J.D., (1975) *Classical Electrodynamics*, John Wiley & Sons, New York.

personal communication]. Also evident in this figure is the fact that there is no strong correlation between the surface field intensity and the triggering probability.

This paradox can be explained in part by the build-up of a space-charge layer near the surface because of corona discharge from vegetation and structures on the ground.[14] Corona occurs whenever the local field exceeds the corona threshold of the ground cover, which is normally a few kV/m. The resulting space charge acts to shield the surface from much higher fields aloft, as illustrated schematically in Figure 2. The corona mechanism effectively limits the surface field intensity to about 10 kV/m or less.

At the other extreme, it is clear that the occurrence of breakdown-field intensity (about 3 MV/m at the surface, decreasing with height in proportion to atmospheric density) should constitute a necessary condition for electrical discharges. This has led some scientists to focus on the geometric field-enhancement factor[15] (sometimes called the "k-factor") as determining a "triggering threshold" for a particular vehicle. For classical triggering, one might predict triggering shortly after the rocket reached sufficient altitude to concentrate the field to 3 MV/m at its tip (see Figure 2).

Unfortunately, this approach does not appear to yield a <u>useful</u> lower bound on the ambient fields required for triggering. This can be seen by studying current records obtained in classical triggering experiments, of which the one in Figure 3 is typical. The positive leader begins propagating upward at time B, when the current rises toward a relatively steady level of a few hundred Amperes. Note, however, that transient current spikes begin at time A, several hundred milliseconds earlier than time B. These spikes are associated with small electrical discharges at the tip of the rocket starting when it is some 100 m lower in altitude. Evidently, electrical breakdown occurred at or before time A, but the rocket had to rise into a region of substantially higher ambient field (time B) before triggering could occur. This indicates that there are other, perhaps more important, necessary conditions for triggering than the occurrence of breakdown fields.

Another suggestion of the probable irrelevance of the breakdown-field criterion can be found in Thayer et al [1989, Figure 6].[15] They show the electrostatic potential, measured previously by J.E. Nanevics on a Titan III rocket during a fair-weather launch, saturating at 200 kV for nearly 5 s shortly after liftoff. The interpretation of this data offered by the authors is that the vehicle was being charged by its rocket motors and that its potential was probably limited by "corona discharges from vehicle extremities". Corona indicates the presence of breakdown fields at one or more locations on the surface of the vehicle, likely in any case at such a high vehicle potential. In the absence of a high ambient field, however, one would not expect a triggered lightning strike, nor are such discharges observed in fair-weather launches.

---

[14] Standler, R.B., and W.P. Winn, (1979) Effects of coronae on electric fields beneath thunderstorms, *Quart. J. Roy. Met. Soc.*, **105**:285-302, 1979.

[15] Thayer, J.S., J.E. Nanevics, and K.L. Giori, (1989) *Triggering of lightning by launch vehicles: determination of the ambient field vehicle enhancement factors*, SRI International, Menlo Park, CA 94025.

4

TRIGGERED LIGHTNING SUMMARY AT KSC FROM 1983 TO 1991

ROCKETS

60
50
40
30
20
10

LIGHTNING

1
10
20
30

ROCKETS

NO LIGHTNING

+KV/M

-KV/M
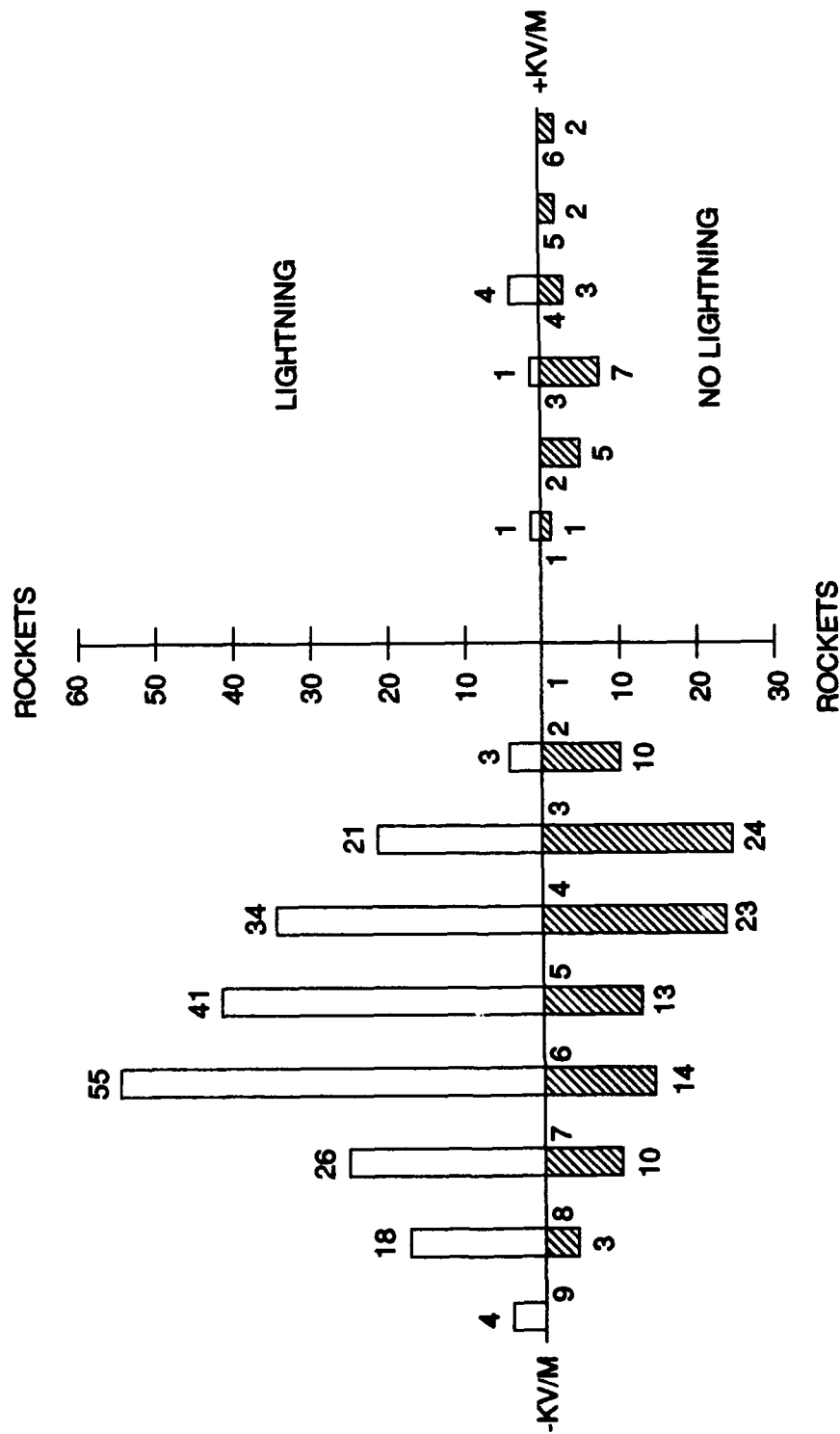
242 ROCKETS TRIGGERED LIGHTNING (READINGS NOT AVAILABLE FOR 34)
167 ROCKETS DID NOT TRIGGER LIGHTNING (READINGS NOT AVAILABLE FOR 50)

Figure 1. Histogram of Occurrence (White) and Non-occurrence (Hatched) of Triggered Lightning Plotted Against Surface Field Intensity. The sign convention here is that negative fields are produced by negative charge overhead, as is normal beneath thunderstorms. Thus, the normal fair-weather field is considered positive.

5

FIELD ENHANCEMENT OF TRIGGERING ROCKET

HEIGHT (m)
POTENTIAL (MV)

$E_z = 50kV/m$

$E_z = 5kV/m$
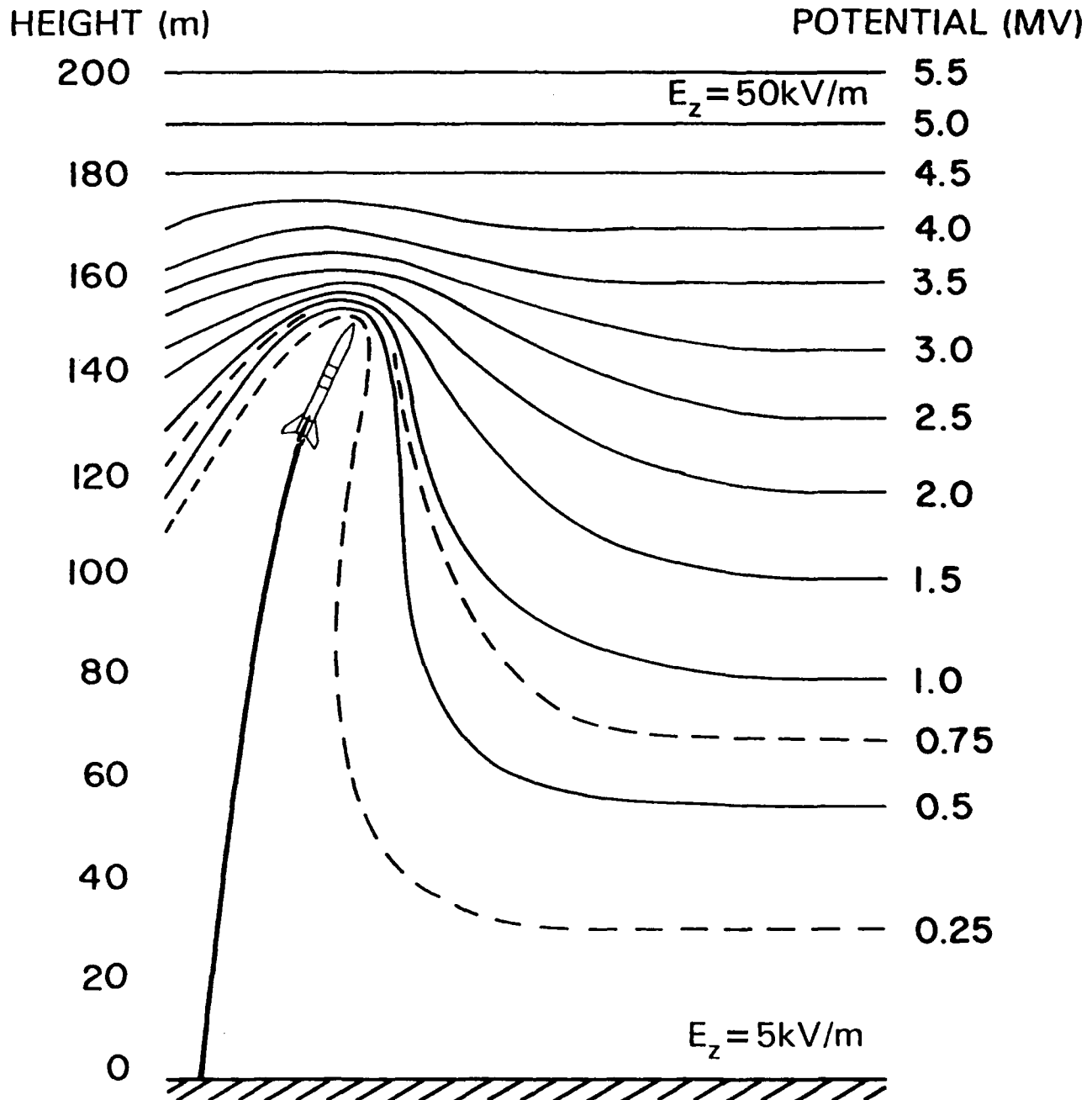
Figure 2. Schematic Illustration of the Equipotential Surfaces in the Lowest 200 m and Their Interaction With a "Classical" Rocket. The equipotentials are closely spaced aloft, where the vertical field is assumed to be 50 kV/m, and near the tip of the rocket, where they are concentrated geometrically. They are further apart near the ground, where the field is greatly reduced by corona space charge.
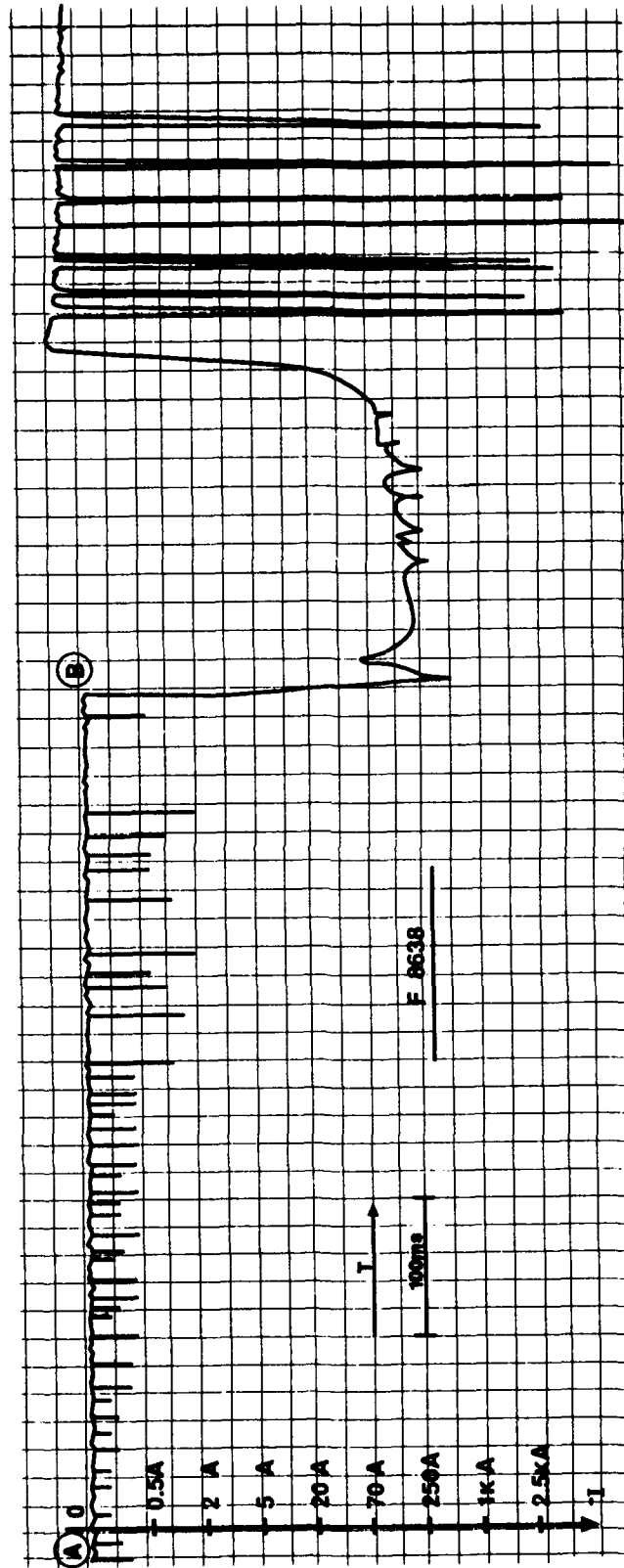
Figure 3. Current Measured at the Channel Base for a Typical Triggered Lightning Flash in Florida. Current is plotted on a logarithmic scale vs. time for a total of 1.3 seconds. The sign of the current indicates negative charge entering the ground, which is normal for cloud-to-ground discharges. "A" indicates the onset of "precursor" pulses. "B" indicates the beginning of the upward leader, which initiates the "continuing-current" phase. The discrete pulses that follow are "return strokes". These data were recorded by CENG, France.

Thus, we are drawn to the conclusion that it is one or more properties of the *ambient* field distribution, probably over some distance along the eventual leader-propagation path, rather than the local field intensity at the surface of the rocket, that determines the triggering conditions.

Several attempts have been made to measure the electric fields associated with lightning strikes to flying aircraft.[16,17] The accuracy of such measurements is problematic, however, because of the difficulty of measuring ambient electrostatic fields from aircraft in the hostile environment in which the data must be taken. Furthermore, we want not only the magnitude of the field at the location where the strike occurred, but also the vector component parallel to, and for some distance along, the direction of propagation of the discharge. Obviously, it can be difficult to determine this direction when the aircraft is flying in cloud and precipitation, and in any case, the aircraft may not be moving in the right direction to obtain this information.

1.3 Planned Approach

The most productive approach to understanding triggering appears to be obtaining near-instantaneous, vertical profiles of the vertical component of electrostatic field immediately prior to a large number of triggering attempts with both classical and altitude rockets. Such profiles, to an altitude of a few kilometers, will allow calculation of the electrostatic energy available for the visible development of the discharge and will permit identification of any other features of the spatial distribution of field that might be important in determining the triggering conditions. Measurements on classical triggering will lead to an understanding of the initiation and propagation of the positive leader -- the initial process in strikes to aerospace vehicles. Measurements on altitude triggering will facilitate determination of the influence of vehicle properties (field-enhancement factor, length, velocity, etc.) on the triggering conditions. In both cases, it is necessary to obtain the profiles rapidly, so that the field distribution has no time to change before the triggering rocket is launched. Sounding balloons ascend too slowly for this purpose. Multiple passes by an instrumented aircraft also take too long.

In principle, such profiles could be obtained with numerous individual sensors suspended from a tethered balloon. There are two problems with this procedure, however. First, it is difficult to assure that the tether cable does not influence the measurement. Even tether materials that are good insulators when new become weakly conducting with exposure to the weather, especially at a coastal site.[18,19] Second, there are significant safety and reliability

[16] Anderson, R.V., and J.C. Bailey, (1987) *Vector electric fields measured in a lightning environment*, Memorandum Report 5899, Naval Research Laboratory, Washington, DC 20375.

[17] Laroche, P., A. Delannoy, and H. Le Court de Beru, Electrostatic field conditions on an aircraft stricken by lightning, paper presented at the International Conference on Lightning and Static Electricity, Ministry of Defense Procurement Executive, U.K., Bath, England, Sept., 1989.

[18] Latham, D.J., (1974) *Atmospheric Electrical Effects of an on Tethered Balloon Systems*, Report 2176, Advanced Research Projects Agency, Arlington, Va. 22209.

problems with operating such a tethered-balloon system in a thunderstorm environment. This has been tried at KSC with limited success, most recently resulting in the loss of the balloon and most of the instrumentation in strong winds during August, 1991. It appears that great effort is required to obtain reliable profiles in this manner on a regular basis. Nevertheless, we expect to inter-calibrate our profiling instrumentation with such balloon-borne apparatus on a few occasions.

For all of the above reasons, we chose a rocket to make the required measurements. Rockets have been used successfully by Winn et al.[20] to obtain profiles of the *transverse* components (perpendicular to the direction of flight) of the electrostatic field. Unfortunately, these components are much less scientifically interesting than the longitudinal component (in the direction of flight), and they are not useful for the present purpose. There have been at least two prior attempts to develop rocket-borne sensors to measure the *longitudinal* component of the field. Ruhnke[21] designed a corona-discharge sensor for this purpose, but he was not able to demonstrate its accuracy and reliability in a thunderstorm environment. Scientists at the Office National d'Etudes et de Recherches Aerospatiales (ONERA) in France have also made an unsuccessful attempt to produce such a sensor [P. Laroche, personal communication].

New electric-field-sounding rockets based on shutter field mills are currently under development by the Geophysics and Aerospace Engineering Directorates (formerly the Geophysics Laboratory) of the Phillips Laboratory (PL), and separately by ONERA. This report describes the design, calibration, and successful first flight of our prototype Rocket Electric Field Sounding (REFS) payload aboard a 2.75-in. Folding-Fin Aircraft Rocket (FFAR) motor called the "Mighty Mouse". The intent of the REFS Program is to construct a number of these payloads and launch them as part of the Rocket-Triggered-Lightning Program (RTLP) at the Kennedy Space Center (KSC), Florida, where triggering operations have been under way since 1984.

It is hoped to use REFS instrumentation in the context of a larger investigation of the nature of triggering. In addition to electric field soundings, understanding the physics of leader propagation requires extensive diagnostics of the developing leaders. The goals here are to unambiguously identify some of the processes observed in triggered lightning with those occurring in long laboratory sparks and to completely characterize those phenomena not reproducible in the laboratory because their scale size is too large. High resolution optical observations of geometry, propagation speed, and stepping or non-stepping[22] are needed to tell us the dependence of leader behavior on field magnitude. Direct recordings of current at the

[19] Jonsson, H.H., (1990) Possible errors in electrical measurements made in thunderclouds with balloon-borne instrumentation, submitted to *J. Geophys. Res.*

[20] Winn, W.P., G.W. Schwede, and C.B. Moore, (1974) Measurements of electric fields in thunderclouds, *J. Geophys. Res.*, **79**:1761-1767.

[21] Ruhnke, L.H., (1971) *A Rocket Borne Instrument to Measure Electric Fields Inside Electrified Clouds*, NOAA/ERL, Boulder, CO, April 1971.

[22] Idone, V.P. and R.E. Orville (1988) Channel tortuosity variation in Florida triggered lightning, *Geophys. Res. Lett.*, **15**:645-648.

channel base,[23] as well as remote sensing of charge and current distributions in the growing channel by means of multiple-station, field-change recordings, are important to define the electrical characteristics of these discharges. Spectroscopic and radar observations would also yield valuable information about the physics of the leader channels.

2. CONCEPTUAL DESIGN OF PAYLOAD

2.1 Overview

The design of the REFS payload was based on a proposal originally submitted to NASA/KSC from the New Mexico Institute of Mining and Technology (NMIMT) [Winn, W.P., W. Rison, and J.J. Jones, A rocket-borne instrument to measure electric vectors in clouds, June, 1988, personal communication]. This section describes the overall design articulated in that proposal, as modified during further development in collaboration with PL.

The driving requirement of the design was to obtain *accurate* and *reliable* vertical profiles of the vertical component of electrostatic field $E_z(z)$. This is essentially the longitudinal component relative to the sounding rocket during most of its flight. The potential importance of these measurements to flight safely, their difficulty, and the lack of any convincing means of verification, as discussed above, require that the payload be self-calibrating and incorporate sufficient redundancy to detect errors in an individual sounding.

Redundancy is essential to rule out several different potential sources of error. Of most concern is the effect of the exhaust plume from the rocket motor during burn (the lowest few hundred meters of the profile). A highly conductive plume would tend not only to charge or discharge the rocket body but also to modify the enhancement factors for ambient field by changing the electrical geometry of the vehicle. Another significant concern is the effect of space charge produced by corona from the vehicle in regions of very high electric field. Charging of the sensors themselves and charge build-up on the insulators, because of particle impaction, corona discharge, or some other source, may also occur under certain conditions. Any of these processes might cause spurious readings that could not be differentiated from real ambient fields without redundancy.

Calibration of the longitudinal component of the field is made difficult by the facts that the vehicle is too long to suspend in readily available uniform-field chambers and that in-flight inter-comparison with other calibrated systems in a high-field environment is problematic. The NMIMT proposal pointed out the following clever means of self-calibration, assuming that all three components of the ambient vector field are measured. The components

[23] Laroche, P., A. Eybert-Berard, L. Barret, J.P. Berlandis, (1988) Observations of preliminary discharges initiating flashes triggered by the rocket and wire technique, paper presented at the 8th International Conference on Lightning and Atmospheric Electricity, National Science Research Council, Uppsala, Sweden, June 1988.

transverse to the rocket are relatively easy to calibrate because of its small diameter and nearly cylindrical geometry. Since the rocket will arc over fairly rapidly at apogee, when launched at a high elevation angle, it is possible to transfer this calibration from the transverse to the longitudinal component, provided only that the ambient field near apogee is slowly varying in time and space. The assumption of slow time variability can be verified by the lack of lightning field changes at field mills on the ground. The assumption of spatial homogeneity can be supported by the similarity of upward and downward profiles. Thus the longitudinal component can be calibrated in flight on many of the individual soundings.

The redundancy requirement on the longitudinal field component implies measurements at three or more longitudinal positions along the rocket body, forcing the choice of shutter field mills (as opposed to corona probes or cylindrical mills) as the basic sensors. This choice, together with the need for the transverse field components to satisfy the self-calibration requirement, implies a minimum of five such sensors. (It is possible to develop a hybrid system to meet these requirements. ONERA envisions shutter mills of novel design, each measuring the average radial field at one longitudinal position, plus a cylindrical mill to determine the two transverse components. Such an approach introduces additional complexities, however.) Having made these choices, we are designing what is essentially an ABFM system. The problems involved have been discussed recently by Kositsky et al.,[24] Jones,[25] Bailey and Anderson,[26] and Laroche.[27] Theoretically, suitable placement of five mills would allow determination of the three components of ambient field, after removal of the effects of vehicle charge, and still provide one redundant measurement. Fortunately, the almost perfect cylindrical symmetry of a rocket and the flexibility afforded by a custom-designed payload permit more nearly ideal mill locations than are possible on an aircraft.

2.2 Implementation

The most important innovation in the NMIMT proposal was the use of a single, long, cylindrical shell concentric with, and rotating about, the longitudinal axis of the rocket. This shell covers most of the payload and acts as the "rotor" for all the mills, as shown in Figure 4. With this design concept, the number of mills can be increased simply by gluing additional

[24] Kositsky, J., K.L. Giori, R.A. Maffione, D.H. Cronin, J.E. Nanevicz and R. Harris-Hobbs, (1991) Airborne Field Mill (ABFM) System Calibration Report, Project 1449, SRI International, Menlo Park, CA.

[25] Jones, J.J., (1990) Electric charge acquired by airplanes penetrating thunderstorms, J. Geophys. Res., 95:16,589-16,600.

[26] Bailey, J.C., and R.V. Anderson, (1987) Experimental Calibration of a Vector Electric Field Meter Measurement System on an Aircraft," Memorandum Report 5900, Naval Research Laboratory, Washington, DC.

[27] Laroche, P., (1986) Airborne measurements of electrical atmospheric field produced by convective clouds, Rev. Phys. Appl., 21:809-815.

ROCKET ELECTRIC FIELD SOUNDER (REFS)

ROTATING SHELL
(SHUTTER)

SHUTTER WINDOWS
(IN OPPOSING PAIRS)
FOR 8 FIELD MILLS

S-BAND TRANSMITTER
AND ANTENNA

"MIGHTY MOUSE"
ROCKET MOTOR

CORONA WIRE
FOR CHARGING

Z

Y

X
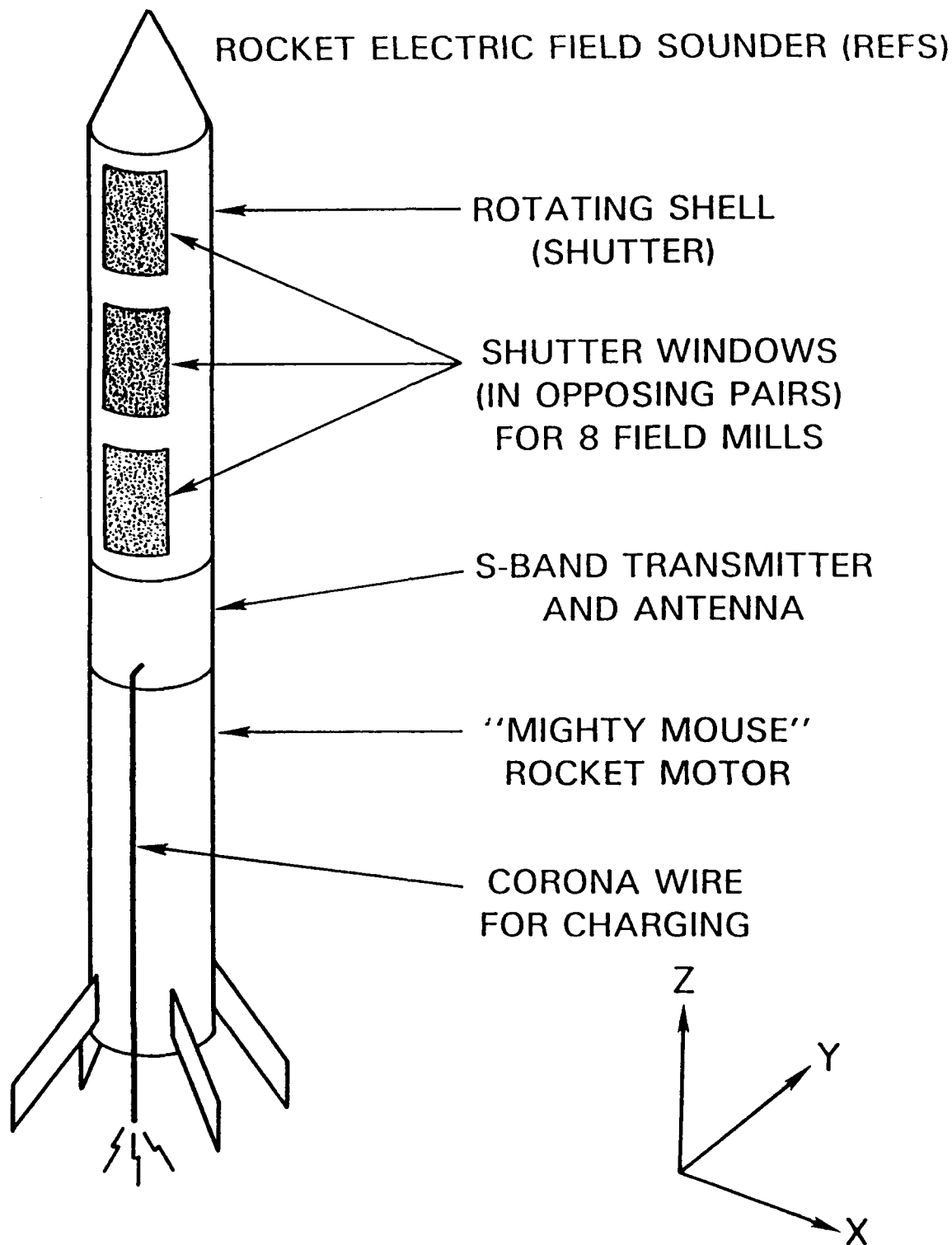
Figure 4. Schematic Illustration of the REFS Payload Mounted on its Rocket Motor. The outer, rotating shell ("rotor"), with its six cut-outs (three shown), periodically exposes eight "stator" electrodes, mounted on the inner shell, to the external field. The coordinate system defined in Section 4.1, with the z-axis pointing forward along the longitudinal axis of the rocket, the x-axis in the direction of the middle-top stator, and the y-axis in the direction of the top- middle- and bottom-right stators, is also shown.

"stator" electrodes onto the payload body and cutting corresponding holes in the rotor to chop the field to these stators.

In consideration of the low cost of adding sensors to the payload, it was decided to use a total of eight field mills on REFS, arranged in symmetrical pairs on opposite sides of the longitudinal axis (see Figure 4). These pairs are located at three different longitudinal positions: one near the forward end, one near the aft end (near the center of the vehicle, accounting for the motor), and two in the middle of the payload. One of the middle pairs has an azimuthal orientation perpendicular to that of the other three, allowing both transverse field components to be measured. This approach takes maximum advantage of the cylindrical symmetry. Opposing mill signals can be differenced to cancel vehicle charge and longitudinal field (giving three independent measurements of one transverse component and one measurement of the other) and can be summed to cancel transverse field (giving three independent quantities -- one redundantly -- from which to derive longitudinal field and vehicle charge). Furthermore, all eight stators can be covered and uncovered twice per revolution of the rotor by only three symmetrical pairs of opposing holes.

The considerable redundancy afforded by these eight mills allows the data to be checked against the electrostatic model of the rocket (see Section 6.1) for possible inconsistencies caused by the exhaust plume, space charge in the immediate vicinity of the vehicle, or spurious readings from individual mills. A good fit of model to data indicates proper functioning of the payload and, hence, reliable derived values for the ambient field components. These components can still be derived redundantly with as many as three bad mills, as long as the malfunctioning sensors are not grouped in an unfortunate way.

As with any other ABFM system, REFS must have the capability to charge itself artificially in flight. The NMIMT proposal called for an on-board, high-voltage power supply to energize a corona emitter that dumps ions into the air stream, periodically charging the vehicle to moderate potentials. It was considered possible that a single-polarity supply might rapidly drive the rocket to its corona threshold and be unable to significantly change its potential thereafter. Therefore, a dual-polarity supply was necessary, at least for the first flight, to guarantee a known charging cycle. Measurement of the voltage on the corona emitter as a function of time was also required. Such a cycle allows the self-charge coefficients of the various mills to be determined very accurately, enabling precise measurement of the ambient field regardless of vehicle charge. As an additional benefit, artificial charging provides a functional check and relative calibration of all the mills in flight.

Another valuable check is provided by telemetering the entire waveform from each mill (charge on the stator as a function of time) back to the ground, rather than performing the synchronous rectification on board. In this case, rotor-position information must also be telemetered. NMIMT suggested the use of passive optical detectors looking at the sky through a series of holes in the rotor. Since the entire vehicle rotates throughout the flight, constancy of the ambient light level can be used as an indicator of cloud penetration. Although this low-level approach to the signal processing requires a much wider telemetry bandwidth than the conventional one, it enables most potential malfunctions of the mills to be positively diagnosed, and it significantly reduces the size of the electronics package.

13

With simple glued-on stator plates, it is not practical to electrically shield the stator insulators from the shutter -- a common practice to minimize spurious signals in shutter field mills due to surface charge on these insulators. A refinement of the design has been introduced to solve this problem. Each hole in the rotor is made smaller than the corresponding stator plate. Thus, there are time intervals both when the stator is fully covered and when a constant area of stator is exposed. During these two intervals the insulators surrounding the stators, and stator edges themselves, are fully covered by the rotor, so that any effects of charge on the insulators are the same. Averaging the mill signal over each of these intervals and differencing the results accomplishes the synchronous rectification while canceling any contribution from surface charge.

Three more sensors have been added to define vehicle performance. A pressure transducer is used to determine altitude. The critical information here is the apogee time and height, from which the rest of the trajectory can be estimated with computer models. The ignition time and duration of motor burn are monitored by a longitudinal accelerometer. Finally, the rotation of the vehicle is defined with a single-axis magnetometer oriented transverse to the rocket axis. This completes the overall conceptual design.

3. ELECTRONIC DESIGN

This section includes descriptions of the REFS block diagram, electronics, Ground Support Equipment (GSE) and internal/external power-switching circuits. These circuits were originally designed by NMIMT, but were modified and improved by the Aerospace Engineering Division (SXA) of PL.

The REFS electronics can be broken down into ten different circuit types located on two separate PCBs. One PCB contains the analog circuitry, the other contains the digital circuits. The ten different types of circuits are:

	Circuit Type	Number of Circuits
1.	Stator Charge Amplifier	8
2.	Pressure Sensor	1
3.	Accelerometer	1
4.	Earth's Magnetic Field Sensor	1
5.	Optical Sensor (Shell Rotation Rate)	2
6.	High Voltage Control & Supply	1
7.	PCM Encoder	1
8.	RF Circuits (Transmitter, Antenna and modulation control)	1 ea.
9.	DC-DC Converter	1
10.	Battery	1

See the block diagram (Figure 5) for more detail.

3.1   Stator Charge Amplifier (Figure 6)

There is one Stator Charge Amplifier (SCA) for each field-mill stator located on the REFS payload. Each SCA is identical and contains three stages: a charge amplifier with lightning protection, a filter, and a current driver.

Two diodes in opposite orientations provide protection in the event of a nearby lightning strike. If the input of the charge amplifier is forced above or below "virtual" ground by more than 0.5 V, then these diodes will conduct and protect the amplifier. Lightning-protection diodes are placed on the inputs of all REFS analog circuits.

The charge amplifier provides a voltage output that is proportional to the electric field seen by the stator plate. When the shutter opens, the 0.01 µF capacitor in the feedback loop of the first operational amplifier (opamp) charges up to a voltage that is proportional to the charge induced on the stator by the electric field incident upon it. The 33 MOhm resistor in the feedback loop is there to provide bias current for the opamp. The resistor and capacitor pair must have a time constant sufficiently large so as not to discharge the capacitor significantly before the shutter is open again. The rotating shell openings have a period of 0.033 s. The 33 MOhm resistor provides a time constant of 0.33 s. This is sufficient to provide the bias current without compromising the measurement.

The second stage of this circuit is a low-pass filter. This filter will be discussed here, but it appears in all the other analog circuits. This filter has a gain of 1.26 and a cutoff frequency of 1 kHz. It is constructed using one LF444 and two 1000 pF capacitors that provide two poles. This configuration is usually called a Sallen/Key filter. It is used for removing high frequency noise from its channel. The filter is followed by a current driver with unity gain.

The sensitivity of the stator circuitry was set to provide a full-scale output in a field of 1 MV/m. This was done by setting the feedback capacitor C_f in the first stage of the charge amplifier. The smaller this capacitor, the more sensitive the amplifier. The capacitor was chosen according to the formula $V_{out} = Q/C_f$, where V_{out} is the output of the first stage of the charge amplifier, and Q is the charge induced on the stator plate. This charge is related to the field as discussed in Section 6.

The signal-to-noise ratio (S/N) of this circuit is calculated by taking the full-scale output range, corresponding to 1 MV/m, and dividing it by the noise level. The S/N for all of the stator channels was about 50 dB.

3.2   Pressure Sensor (Figure 7)

The pressure transducer was used to ascertain payload altitude, more specifically the moment and height of apogee. The circuitry centers on an SCX15AN pressure transducer made by Sensym, Inc. This absolute pressure transducer is a bridge device with a range of 0 to 15 PSI. It produces a change in bridge resistance that is proportional to pressure.
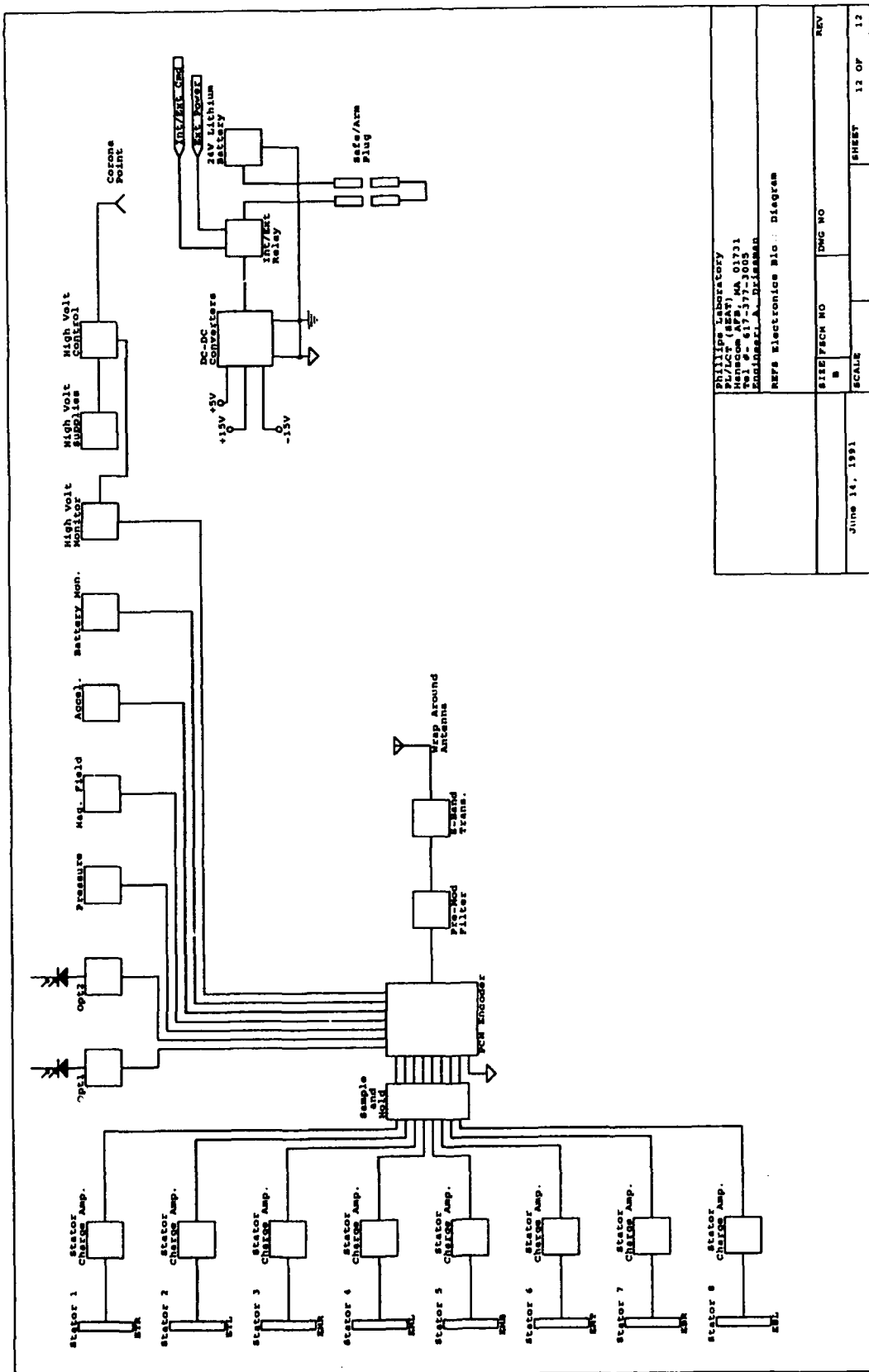
Figure 5. Block Diagram of the Electronic System
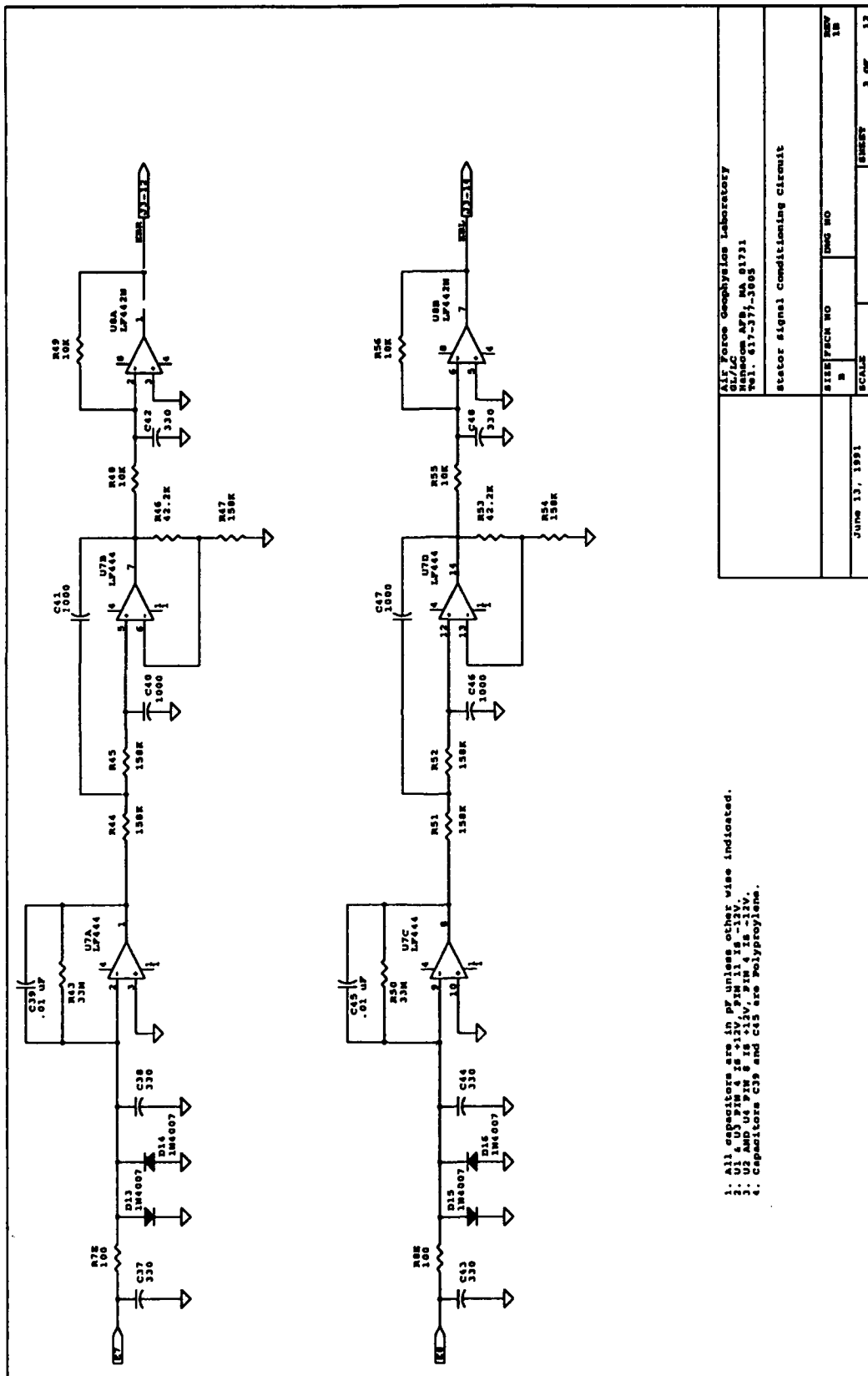
Figure 6. Typical Stator Charge Amplifier Circuit

Figure 7. Pressure Sensor Circuit Diagram

When powered by a +10 V supply voltage, this unit produces an output of 6 mV/PSI. The output of this device goes into an instrumentation amplifier and low-pass filter. The gain term for this instrumentation amplifier can be expressed as $V_{out} = 18.2 [V_{pp} - 1.055 V_{pm}]$, where V_{pp} is the positive output of the device and V_{pm} is the negative output. The low-pass filter has been discussed in Section 3.1.

The error due to noise in this circuit is calculated by taking the noise level in volts and translating it to a corresponding altitude error. The noise level of 10 mV corresponds to an altitude error of about 180 ft.

Calibration was performed in the SXA vacuum chamber at the Phillips Laboratory. Figure 8 shows the result.

3.3 Accelerometer (Figure 9)

The longitudinal accelerometer was intended to provide the experimenter with the exact times of liftoff and motor burnout. The principal device used in the accelerometer circuit is the SXL200G, again made by Sensym, Inc. This accelerometer is of the bridge variety and produces a voltage output that is proportional to acceleration. The typical output is 200 μV/g. The output of this device is run into an instrumentation amplifier with a gain term of $V_{out} = 170[V_{am} - 1.006 V_{ap}]$, where V_{ap} is the positive output of the device and V_{am} is the negative output. The signal is then run through the low-pass filter discussed in Section 3.1.

The error due to noise in this circuit is calculated by taking the noise level in volts and translating it to a corresponding acceleration error. The noise level of 10 mV translates to an error in acceleration of about 0.23 g.

Shock testing was used to calibrate the accelerometer. An 11.49 ms, half-sine shock pulse was applied to the base of the payload as part of environmental testing. It appeared during this test that the accelerometer was functioning properly and that its range was well within the limits that the payload was expected to see during flight. During the burn phase of the flight, however, the accelerometer saturated. It became obvious that the calibration technique used was insufficient. One probable cause for the error is that the internal structure damped the shock transmitted to the accelerometer (the sensor is mounted on the electronics boards). Therefore, 11.49 ms was too short a duration.

3.4 Magnetic Field Sensor (Figure 10)

The magnetic-field-sensing circuitry was designed to provide an uncalibrated measure of the transverse component of the ambient magnetic field. Through this circuitry, the orientation of the payload with respect to Earth's magnetic field can be estimated. In particular, payload rotation rate can be determined. The sensor used is a SAS231W made by Siemens, Inc. This sensor measures magnetic flux density and has a sensitivity of 100 mV/mT. Flux concentrators made of Mu-Metal were added on the top and bottom of the sensor

PRESSURE XDUCER CALIBRATION
board set #1
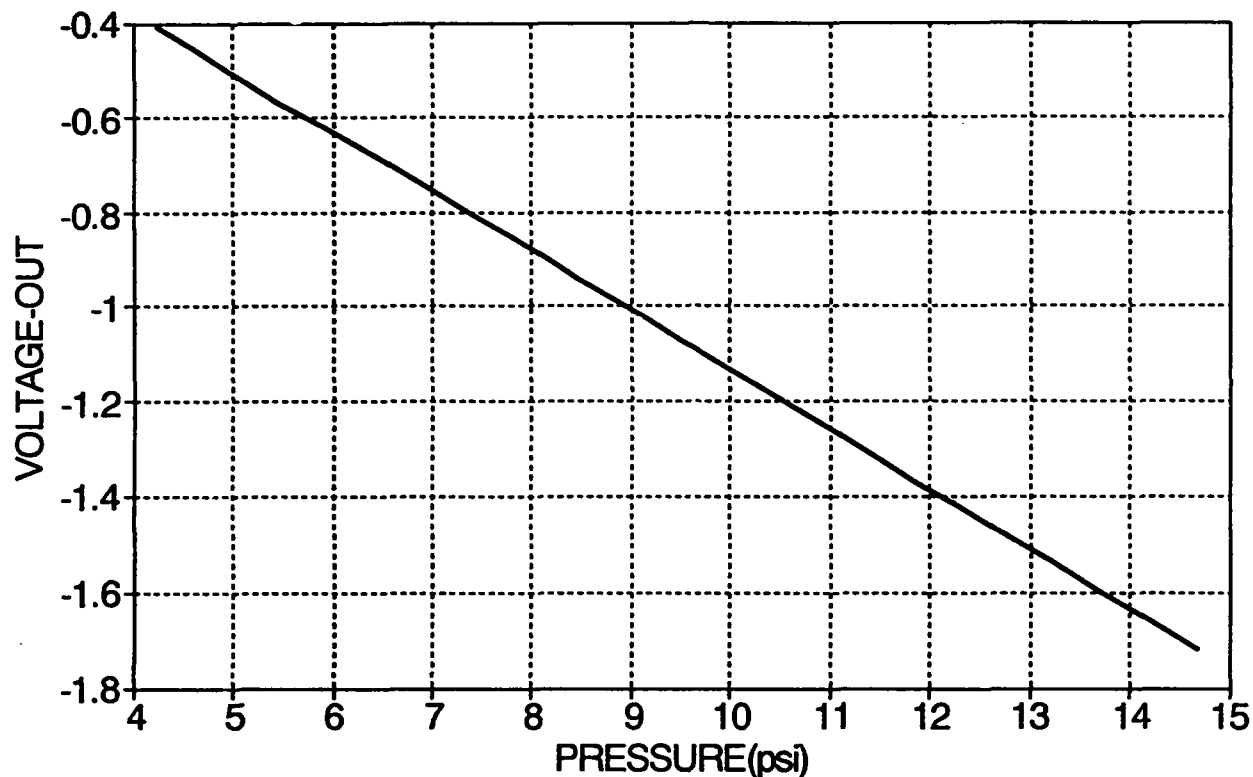
Figure 8. Calibration of the Pressure Transducer in PL/SXA Environmental Chamber

to bring Earth's magnetic field up to a level where the SAS231W could sense it. An amplifier with a gain of 22 was used to bring the output of the SAS231W to a scale of 0.6 V peak to peak. Because of the large temperature sensitivity of this sensor, the circuit showed a severe drift with temperature. It was necessary to add resistors R15B and R16B to force the circuit to operate over the appropriate temperature range.

Calibration was unnecessary for this circuit. S/N is calculated by dividing the signal level (0.6 V) by the noise (.01 V), giving 36 dB.

Figure 9. Accelerometer Circuit Diagram
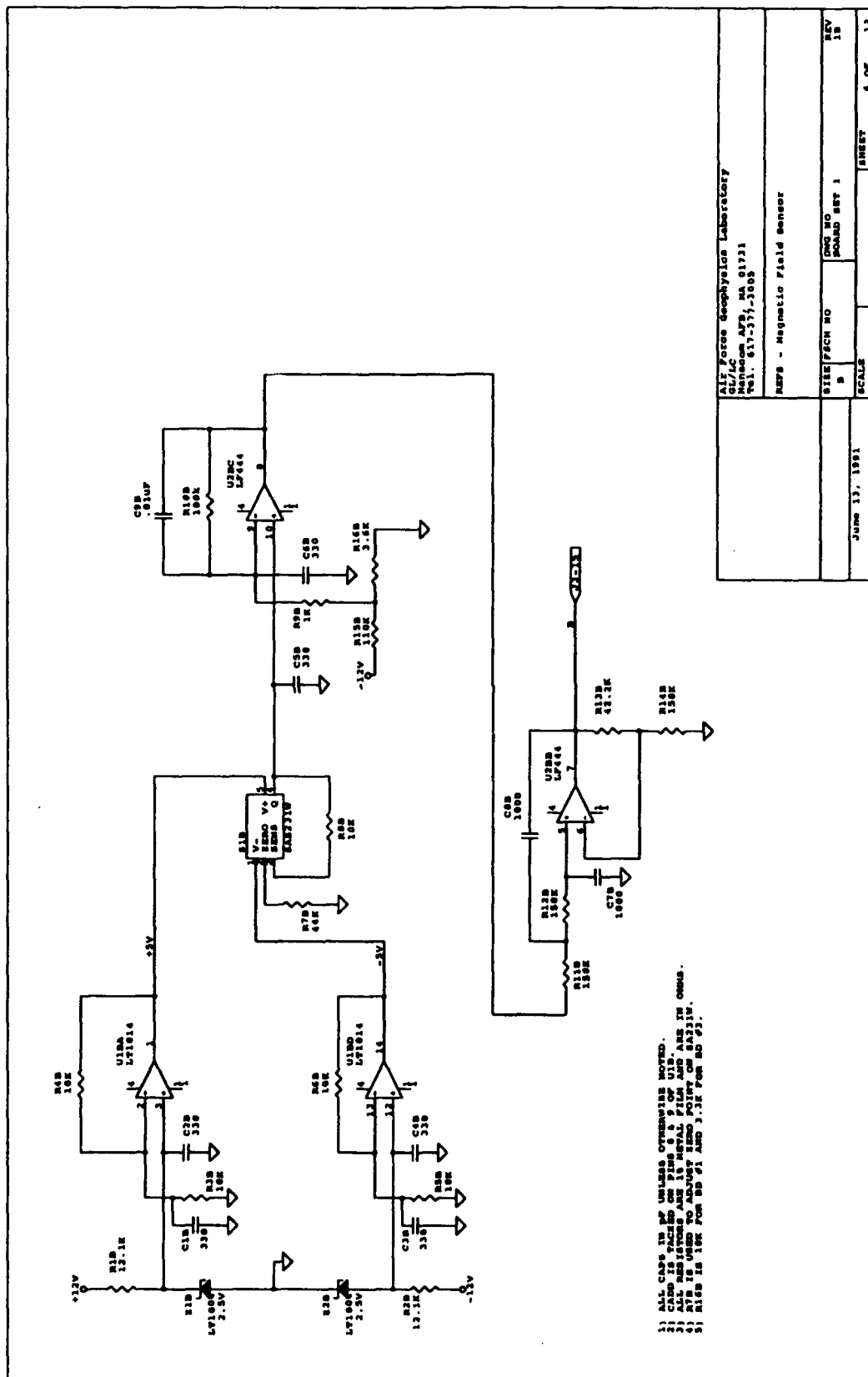
Figure 10. Magnetic Field Sensor Circuit Diagram

3.5 Optical Sensors (Figure 11)

Two optical sensors were developed to provide unambiguous data on the rotor position and to indicate when the payload penetrated a cloud. Each optical sensor looks outward through a hole in the inner shell of the payload. Light can reach the first sensor through a series of 16 evenly spaced holes in the outer (rotating) shell. The second optical sensor is illuminated only by a single hole aligned with the rotor cutouts. (See Section 4.2 for further description of the mechanical configuration of these sensors.) The first sensor provides rotor angular velocity; the second provides absolute angular position. The use of ambient light allows the sky/earth relative brightness to be monitored as the payload rotates. Because light intensity is nearly isotropic within a cloud, but seldom so outside one, it was expected to detect cloud penetrations with these sensors, independent of vehicle charging.

Each optical sensor is supported by an identical circuit. EG&G photodiodes are used to produce a voltage that is proportional to incident light. This voltage is applied to an amplifier with a gain of 7.67 and then into the low pass filter discussed earlier. Resistors R13X through R16X were added to provide a 0.298 V offset to center the two signals.

The signal difference between the covered and the uncovered state for these sensors was typically about 1 V in hazy sunshine. S/N was calculated by dividing this signal (1 V) by the noise (0.01 V), giving 40 dB.

3.6 High Voltage Supply and Control (Figure 12)

As explained in Section 2.2, two high-voltage power supplies were included in the payload. These supplies, plus and minus 10,000 V, respectively, were alternately connected through a resistor to a trailing corona wire for 0.1 s out of every 1.6 s. Provisions were also made to monitor the voltage on the corona wire during flight.

The original NMIMT design called for four control signals to be generated by a Programmable Logic Device (PLD). The first two applied power to the high-voltage supplies at different times. This reduced the duty cycle on the supplies, saving battery power. The third controlled a high-voltage relay to switch between the plus and minus supplies. The fourth drove another high-voltage relay to connect the voltage to the corona wire. These PLD outputs were connected to the gates of MOSFETS that applied power to the supplies and relays.

Soon after testing of the electronics began, three significant problems arose. First, when high voltage was applied to the relays, the PLDs would enter an unstable state that changed the circuit timing. This state could only be reset by cycling power. Second, the MOSFET drivers were constantly being "blown" by spikes induced on the power lines when the high-voltage relays switched. Third, a telemetry dropout of approximately 10 ms was induced every time a high-voltage relay was switched.
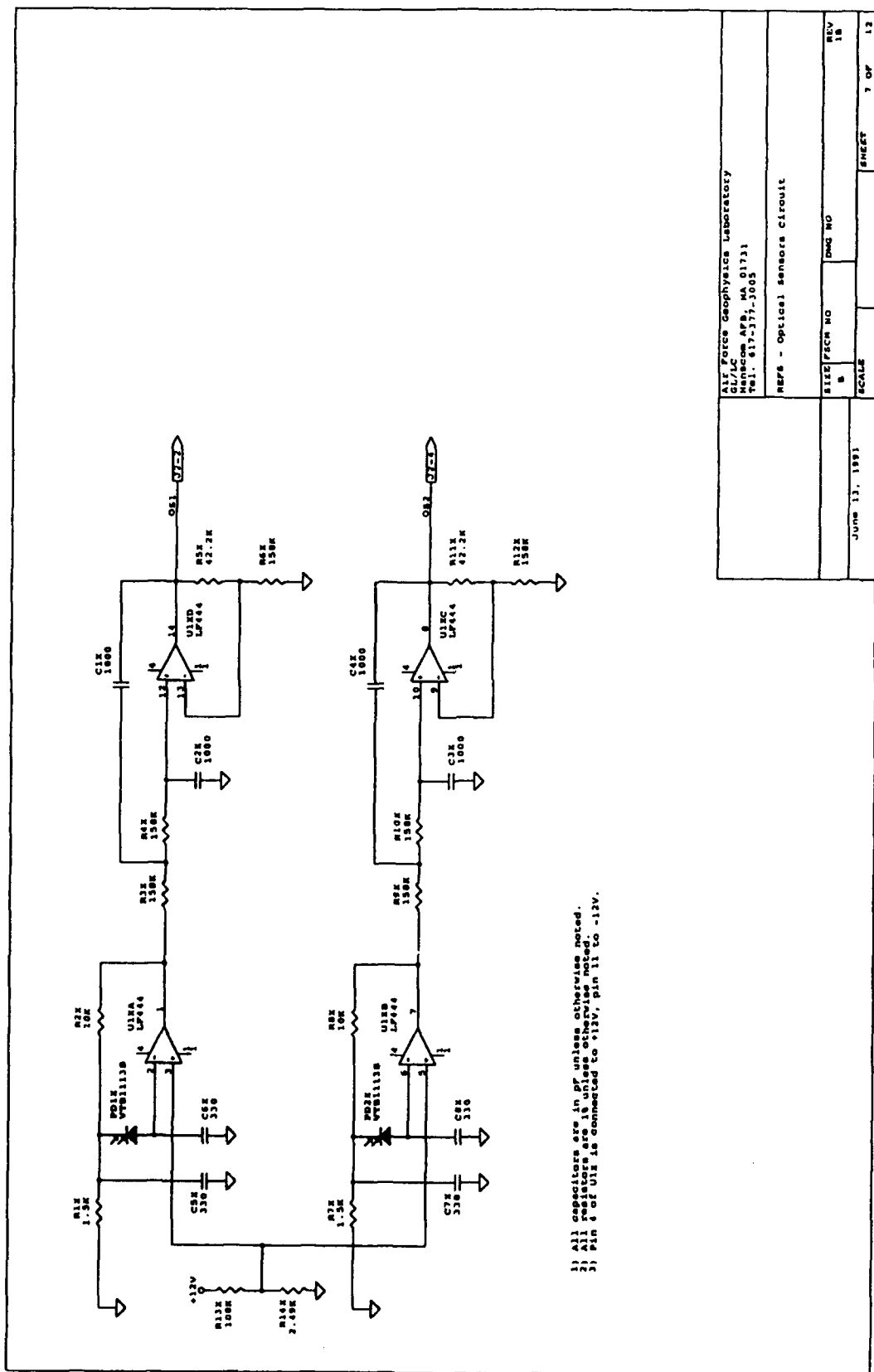
Figure 11. Optical Sensors Circuit Diagram

Figure 12. High Voltage System Circuit Diagram

After many hours spent in trying to isolate the high-voltage electronics from the control electronics, we decided to replace the PLDs with conventional CMOS circuitry. This CMOS circuitry consisted of a binary counter (54HC4020), three 3-input NAND gates and one 4-input AND gate. These three chips were used to generate V1, V2, VN and VP. This solution proved effective in preventing the erroneous timing state from occurring. To make the driving electronics less susceptible to high-voltage spikes, the MOSFETS were also replaced with standard NPN transistors that did not "blow" during high-voltage switching.

The original electronics design provided to the Air Force included no isolation between the high voltage system and the telemetry system. This lack of isolation caused dropouts to appear on the data channels whenever the high voltage was switched. Because of schedule and cost constraints, it was impossible to redesign the payload to add this isolation. Every effort was made to reduce these dropouts through the use of varistors and bypass capacitors, but it was impossible to remove them completely. The payload was flown with telemetry dropouts that were short enough to be considered bearable.

The voltage on the corona wire was monitored through an amplifier with a gain of 0.000258. Because of the series resistor R7B, however, this voltage was only $R_c/(2R_c + 250 \times 10^6)$ times that developed by the high-voltage supplies, where R_c is the "effective" resistance of the corona point. Thus, a maximum of around 5 kV could be applied to the corona point. The signal was again filtered, as discussed earlier.

3.7   PCM Encoder (Figure 13)

Since this payload was to be flown on government ranges using government equipment, it was convenient to use the IRIG 106 Type I telemetry standard for the REFS data-encoding scheme. After going over various technical constraints, it was decided that a 500 Kbit/s, 16-channel, Pulse-Code-Modulation (PCM) encoder was both technically possible and adequate for the task. Bi-Phase-L was specified to facilitate tape recording.

Because of the size and cost constraints imposed by the payload and the program office, it was decided not to use a commercially available encoder. An encoder consisting of approximately 10 chips, including three PLDs, was devised by NMIMT to fulfill the REFS requirement.

The encoder consisted of two quad sample-and-hold chips (AD684, U1D and U2D) that sampled all the stator channels simultaneously. The outputs of these circuits, plus the other analog channels, were placed on the inputs of an analog multiplexer (ADG506A, U3D) that was controlled by PLD U4D (PAL22V10). The output of the analog multiplexer was converted to digital data by an A/D converter (AD7870, U7D) that had a +3 to -3 volt full scale range. The timing for this converter was generated by another PLD (PAL22V10, U5D). The 12-bit digital output of the converter was then shifted into serial data by U8D and U9D (CD4014BF). Control signals for these shift registers were produced by U5D and U6D (another PAL22V10). The serial data was available on a test point in NRZ-L form. Its conversion to Bi-Phase-L occurred in

Figure 13. PCM Encoder Circuit Diagram
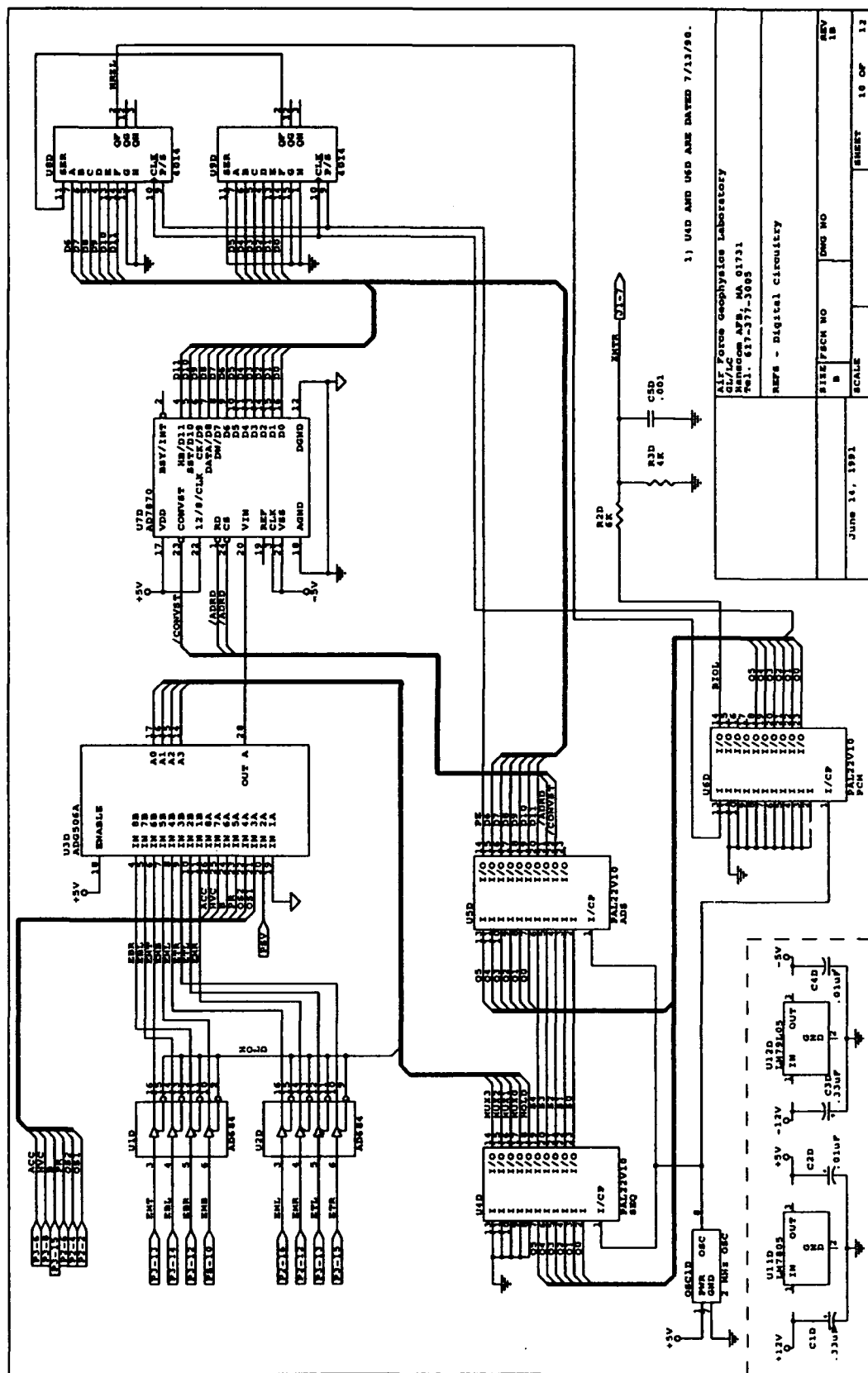
U6D. The whole system ran off a 2 Mhz oscillator and intermediate timing signals generated by U4D. For a detailed timing diagram see Figure 14.

3.8 RF System

Due to the small size and high acceleration of the REFS vehicle, the only transmitter available "off the shelf" was a ballistic, Phase-Modulated (PM), S-band transmitter, model T4X0-S, manufactured by Microcom, Inc. This transmitter was approximately 1.7 inches in diameter and was specified at 1000 g acceleration. It had a center frequency of 2235.5 Mhz and a minimum output power of 0.200 W. Table 1 shows range calculations for the REFS flight.

As previously stated, the T4X0-S is phase modulated. This type of modulation is not typically used for sounding-rocket telemetry. To standardize, it was necessary to convert our PM signal to a Frequency Modulated (FM) signal. A pre-modulation integrator network also shown in Figure 13 was placed between the output of the PCM encoder and the transmitter to make the output appear to be FM.

The telemetry antenna was required to conform to the cylindrical shape of the payload with no protrusions and to radiate a signal at 2235.5 Mhz that was independent of rocket rotation. It was developed for REFS by Rome Air Development Center (RADC) and consisted of four square patches that were each fed through impedance transformers on two sides 90 deg apart (see Figure 15). The antenna was printed on flexible printed-circuit board made of 0.015-in thick PTFE (dielectric constant 2.2) clad with copper on both sides, which was wrapped around the payload and epoxied in place. Unused portions of the antenna surface were left plated and were grounded to the shell by screws to reduce insulating surface area.

The Physical Science Laboratory at New Mexico State University measured the radiation pattern of the REFS antenna in flight configuration. As expected, radiation from the antenna was strongly right-hand-circularly polarized, left-circular power being more than 11 dB weaker overall. The right-circular radiation pattern was very uniform with longitude angle, as illustrated in Figure 16a. Narrow transmission nulls were apparent out of the fore and aft ends of the payload, as shown in Figure 16b. The radiated power was -2.97 dBi (normalized to an ideal spherical radiator) and the angular coverage at -10 dBi was 99.7 percent of the sphere.

Figure 14. Control Circuitry Timing Diagram

Table 1: Range Calculations For REFS Wallops-Island Launch

ITEM	VALUE
TRANSMITTER POWER	0.20 W
CABLE LOSS TO ANTENNA	1.00 dB
TRANSMIT ANTENNA GAIN	-8.00 dB
SLANT RANGE	12.00 km
FREQUENCY	2235.50 MHz
POLARIZATION LOSS	3.00 dB
* SIGNAL @ RECEIVING ANTENNA	-110.00 dBm
SKY NOISE TEMPERATURE	500.00 K
RECEIVING ANTENNA GAIN	41.01 dB
CABLE LOSS (ANT-PREAMP)	1.00 dB
PREAMP GAIN (NO AMP=0)	0.00 dB
PREAMP NOISE FIGURE (NO AMP=1)	1.00
CABLE LOSS (PREAMP-REC.)	3.00 dB
RECEIVER NOISE FIGURE	1.00
BANDWIDTH	1.50 MHz
* SYSTEM NOISE @ ANTENNA	-107.12 dBm
* SIGNAL TO NOISE RATIO	38.12 dB
MINIMUM S/N RATIO (BER 1e-6)	16.00 dB
* EXCESS S/N MARGIN @ RECEIVER	22.12 dB
DISH ANTENNA DATA	
DIAMETER	7.50 m
* GAIN	41.01 dB
* BEAM WIDTH	1.24 Deg
Site Distance	12.00 km
Field of View @ 12 Km	258.80 m
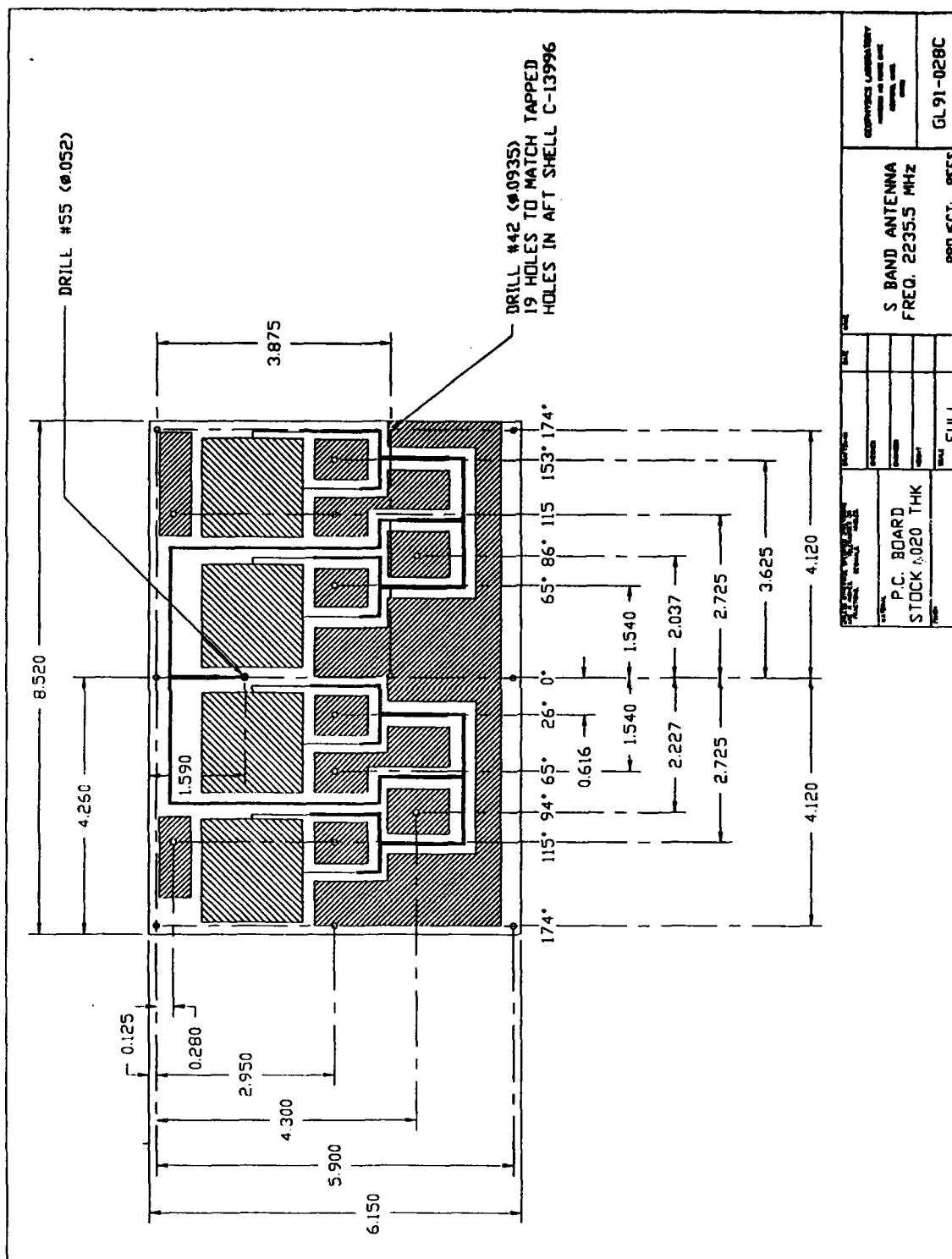
Figure 15. Printed-circuit-board Layout for the S-band Patch Antenna. This pattern was printed on thin PCB stock, which was then wrapped around the payload body to conform to its cylindrical surface. The plated areas not connected to the antenna feed were grounded to the payload shell with screws.

NOTE: FEED POINT AT
$\phi = 0$, $\theta = 90$

DATA FILE = D1REF S01B.CRC

POLARIZATION
☐ GAIN REF __ __ __ __
☐ Eθ _____
☐ Eφ _ _ _ _ _ _ _ _ _ _
☐ R.C. _ _ _ _ _ _ _ _ _ _
☐ L.C. _ . _ . _ . _ . _ .
☐ OTHER AS NOTED
   UNDER REMARKS.

THETA = 90.1 CUT

$\phi = 0$ • $\theta = 90$ •   COORDINATE
                             REFERENCE.

$\phi = 90$ •
$\theta = 90$ •

CALIBRATION
RELATIVE
FIELD STRENGTH
2 dB/DIV.

FIG 1
FREQUENCY 2235.5 MHZ
ANTENNA REF VEHICLE 2.75" DIA WRAPAROUND
REMARKS FULLSCALE(DBI) = 0
DATE = 05-08-1991
DATA MEAS = CHA = LHCP, CHB = RHCP, PHASE B-TO-A
COMPONENT CHB DATA
MAX (DB) = -1.4 AT 280.1
MIN (DB) = -2.8 AT 228.2

Figure 16a. Measured Intensity of Right-circularly Polarized Radiation From the REFS Antenna, as a Function of Longitude Angle in the Equatorial Plane (Perpendicular to the Payload Axis). Intensity is plotted in dBi (relative to an ideal isotropic radiator). The circular divisions are 2 dB with 0 dBi at the outer edge. The outer radial divisions are 5 degrees.

32

DATA FILE = D1REF S01B.CRC

POLARIZATION
- ☐ GAIN REF -- -- -- --
- ☐ Eθ _____
- ☐ Eφ _____
- ☐ R.C. _____
- ☐ L.C. _____
- ☐ OTHER AS NOTED
  UNDER REMARKS.

PHI = 0 CUT

φ = __0__ ∘   θ = __0__ ∘   COORDINATE
REFERENCE.

φ = __0__ ∘
θ = __90__ ∘

CALIBRATION
RELATIVE
FIELD STRENGTH
__2__ dB/DIV.
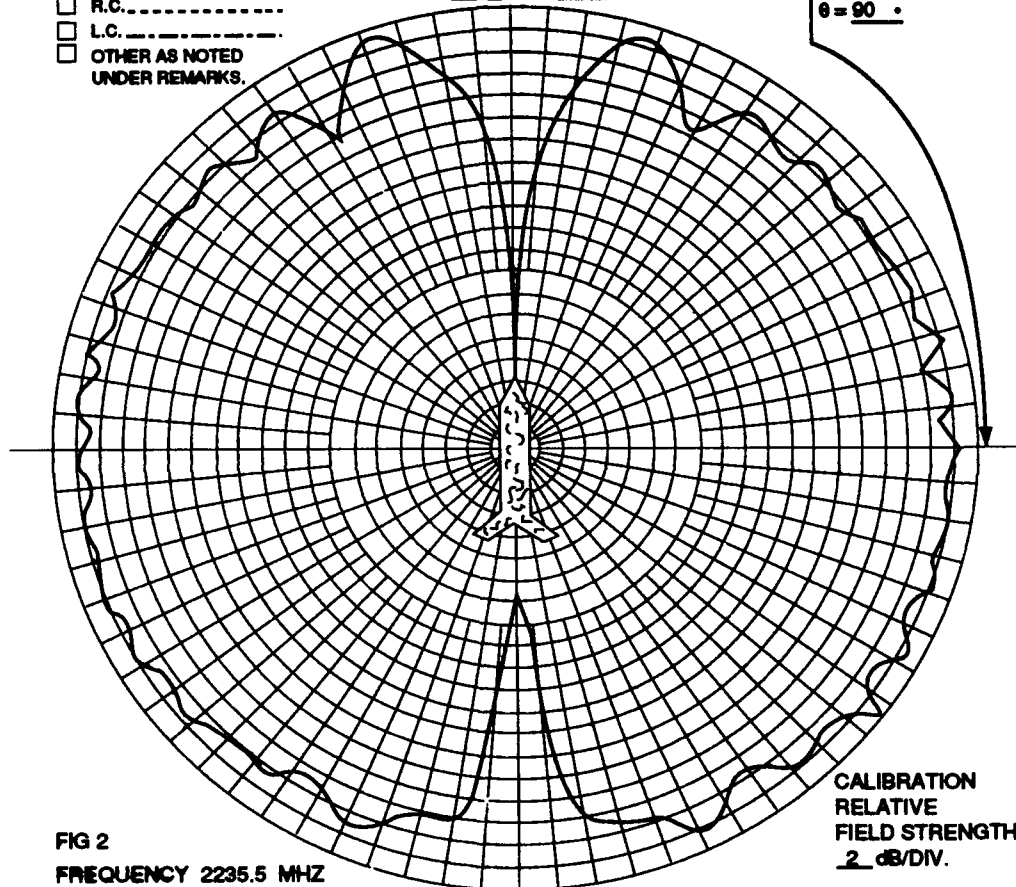
FIG 2
FREQUENCY 2235.5 MHZ
ANTENNA REF VEHICLE 2.75" DIA WRAPAROUND
REMARKS FULLSCALE(DBI) = 0
DATE = 05-08-1991
DATA MEAS = CHA = LHCP, CHB = RHCP, PHASE B-TO-A
COMPONENT CHB DATA
MAX (DB) = -.9 AT 341.8
MIN (DB) = -33 AT 359.9

Figure 16b. Similar to 16a, but Plotted as a Function of Latitude Angle in the Meridional Plane (Including the Payload Axis). The orientation of the payload is indicated by the sketch in the center of the plot.

33

3.9   DC-DC Converters (Figure 17)

Five voltages were necessary to run the REFS payload. They were +24, +5, +12, -12 and +15 V. The +24 V was used to power the DC motor and the 0.200 W S-Band transmitter. This +24 V was unregulated and varied from +31 V to +21 V as explained in Section 3.10.

The +5 V was used to power all the digital circuitry. The +5 V was brought down from the +24 V battery voltage through an IDEC DC-DC Converter (Model PSR-BD03005-24). This converter can provide 500 mA at 5 V, but had to provide only 260 mA.

The +/- 12 V lines were used to power the analog circuitry. The DC-DC converter chosen was an IDEC PSR-BD03033-24. This converter is capable of providing 125 mA from both the plus and minus 12 V outputs. The actual draw was approximately 75 mA per output.

The +15 V (Model: IDEC PSR-BD03015-24) converter was used to power the high voltage power supplies. Though the HV supplies have a maximum operating voltage of +12 V; they were given their own converter because of their large current draw (approximately 150 mA). The +15 V converter appeared in the original design, and because of the lead time in purchasing a +12 V converter, it was decided to retain the +15 V supply. The +15 V was reduced to approximately +12 V with diode drops.

3.10   Batteries (Figure 18)

The requirement placed on the batteries was to provide between +21 and +32 V under a 1 amp load for 15 min.

A thorough industry search was started to find a battery with the proper power characteristics that would fit in the small REFS payload. This industry search provided one source that would guarantee such a battery, but the cost ($1000 per battery) was deemed excessive.

After failing to find a complete battery on the market, we decided to construct a battery from off-the-shelf cells. Many different chemistries were tried. The result was a 22-cell battery made up of 2/3A size Lithium Poly-Carbon Mono-Fluoride cells manufactured by Matsushita Battery Company (model # BR-2/3A). This battery had a no-load voltage of 36 V and a load voltage of 21 V that, after 10 min. warm-up, reached 24 V. This combination of chemistry and quantity of cells provided the power that was necessary.

The REFS battery exceeded its requirement and appeared to work flawlessly through test and flight. It provided the 800 mA needed to operate the payload for 45 min. at a plateau voltage of 24 V.

34
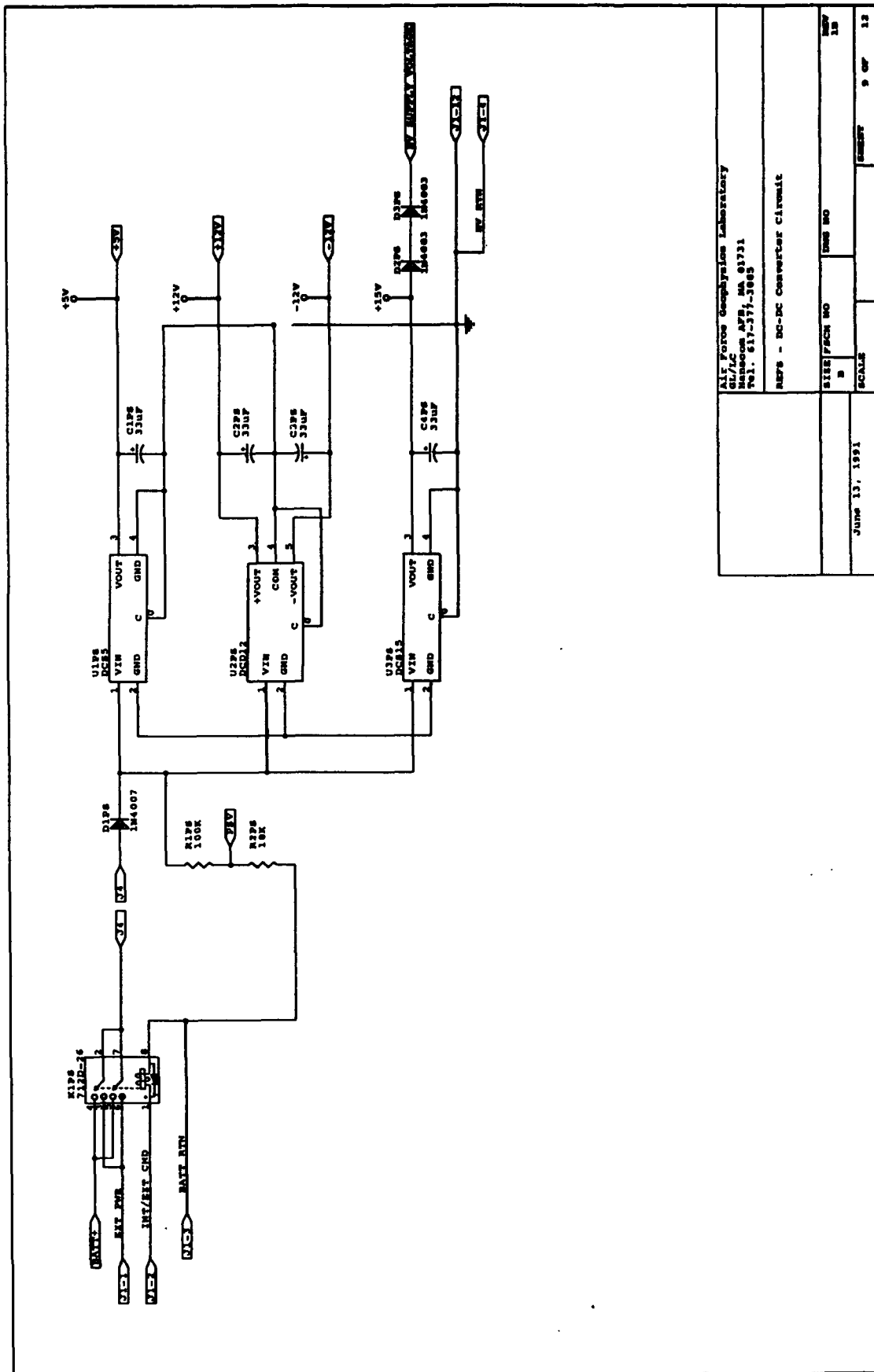
Figure 17. DC-DC Converter Circuit Diagram
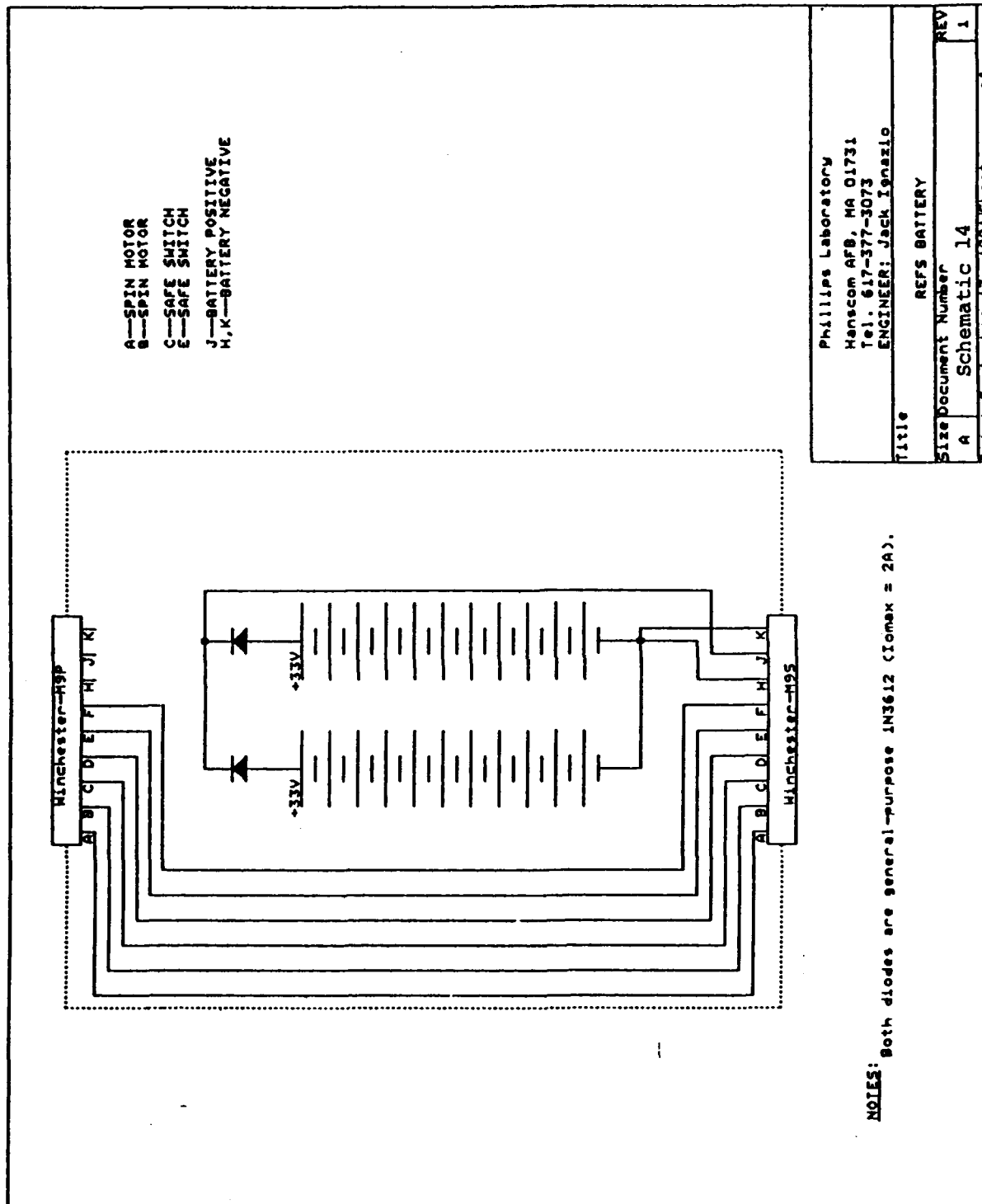
Figure 18. REFS Battery Connection Diagram

3.11 Internal/External Power Circuits and Ground Support Equipment (Figure 19)

The REFS payload has the capability of being powered by either an internal lithium battery or an external source. Our external power was supplied by a Nickel-Cadmium (NiCd) battery in the GSE. The use of internal or external power is controlled by a command that switches an on-board relay. External power and the Int/Ext command are provided to the payload via a 3-wire, pull-away umbilical from the GSE. To actuate the Int/Ext command, +28 V is placed on a line in the umbilical that causes the on-board relay to switch to external power. A non-latching relay is used so that the payload's default position is internal power. The payload is shut off by placing the relay in the external-power position and shutting the external power off. This design permits the payload to be tested on both external and internal power before launch.

Additionally, a "safe plug" located in the nose of the payload actuates a shut-off switch. All power is passed through this switch, so that power cannot reach any of the on-board systems when the safe plug is in position. In practice, the rocket is handled and loaded with the safe plug inserted. The umbilical is connected with external power off and the Int/Ext command in internal mode (no power to the payload). After the rocket motor is armed, the external-power command is actuated at the GSE. Then the safe plug can be removed without starting the payload. The pad area is cleared before any powered tests are conducted. The object of this design is to prevent the payload from being powered up while personnel are near the rocket motor.

4. MECHANICAL DESIGN

The REFS payload weighs approximately 11 lb, is 40 inches long and 2.75 inches in diameter, and is composed of two primary sections (see Figure 20). The first section can be generalized as the rotor/electronics section. This section consists of a rotating shell or rotor and its accompanying spin motor, inner shell, battery pack, electronics boards and nose cone. The second section is the high voltage section. This section contains the telemetry antenna and transmitter, high voltage power supplies, high voltage relays and the umbilical connector.
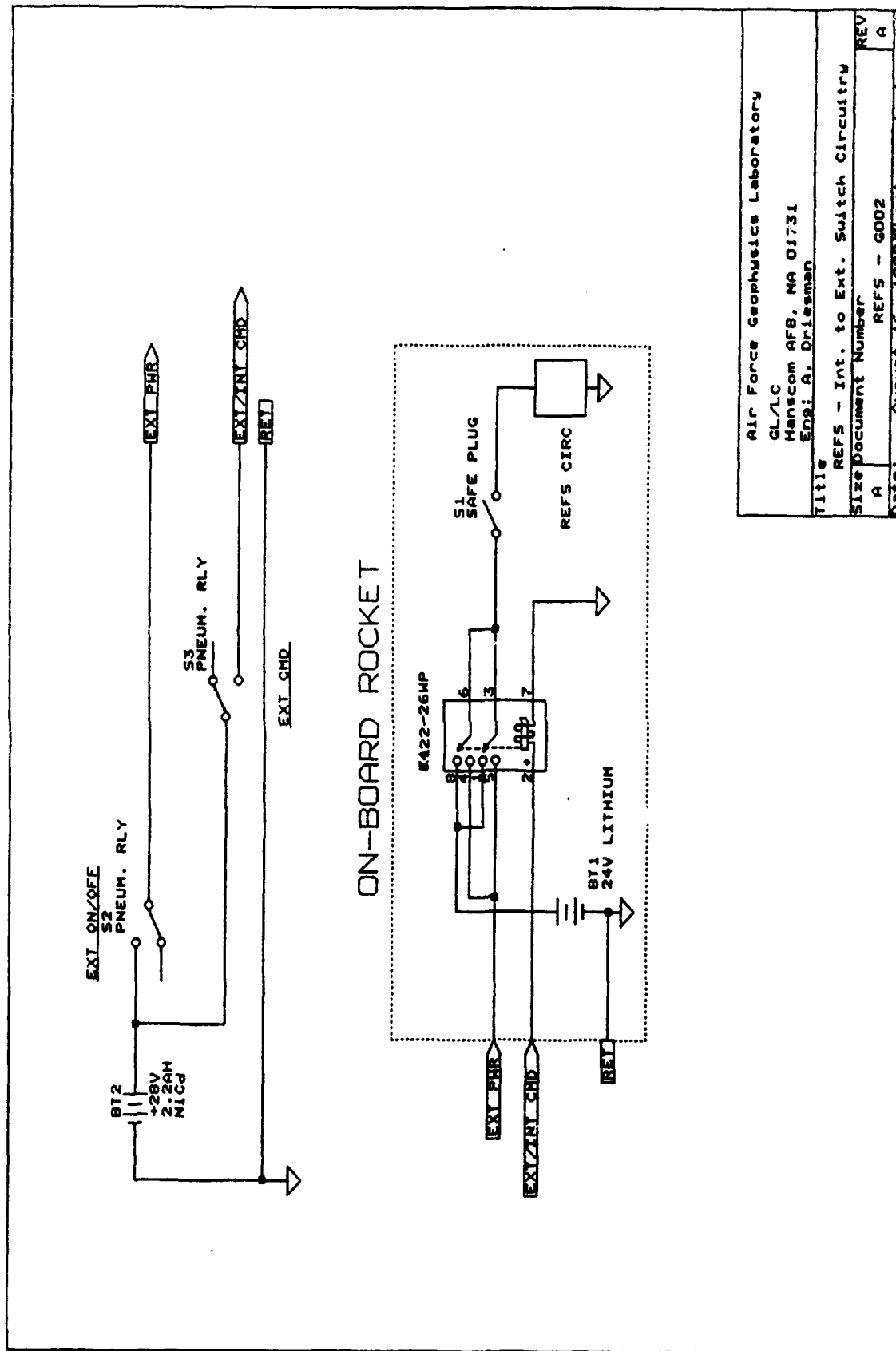
Figure 19. Internal to External Switch Circuitry

REFS

EXPLODED VIEW

NOSE CONE

ROTATING SHELL SPIN MOTOR

ELECTRONIC BOARDS

FORWARD JOINT

BATTERY

ROTATING SHELL BEARING

AFT SHELL- ANTENNA SECTION

ROTATING SHELL

INNER SHELL

AFT JOINT

MID JOINT- AFT

MID JOINT- FORWARD

ROTATING SHELL BEARING
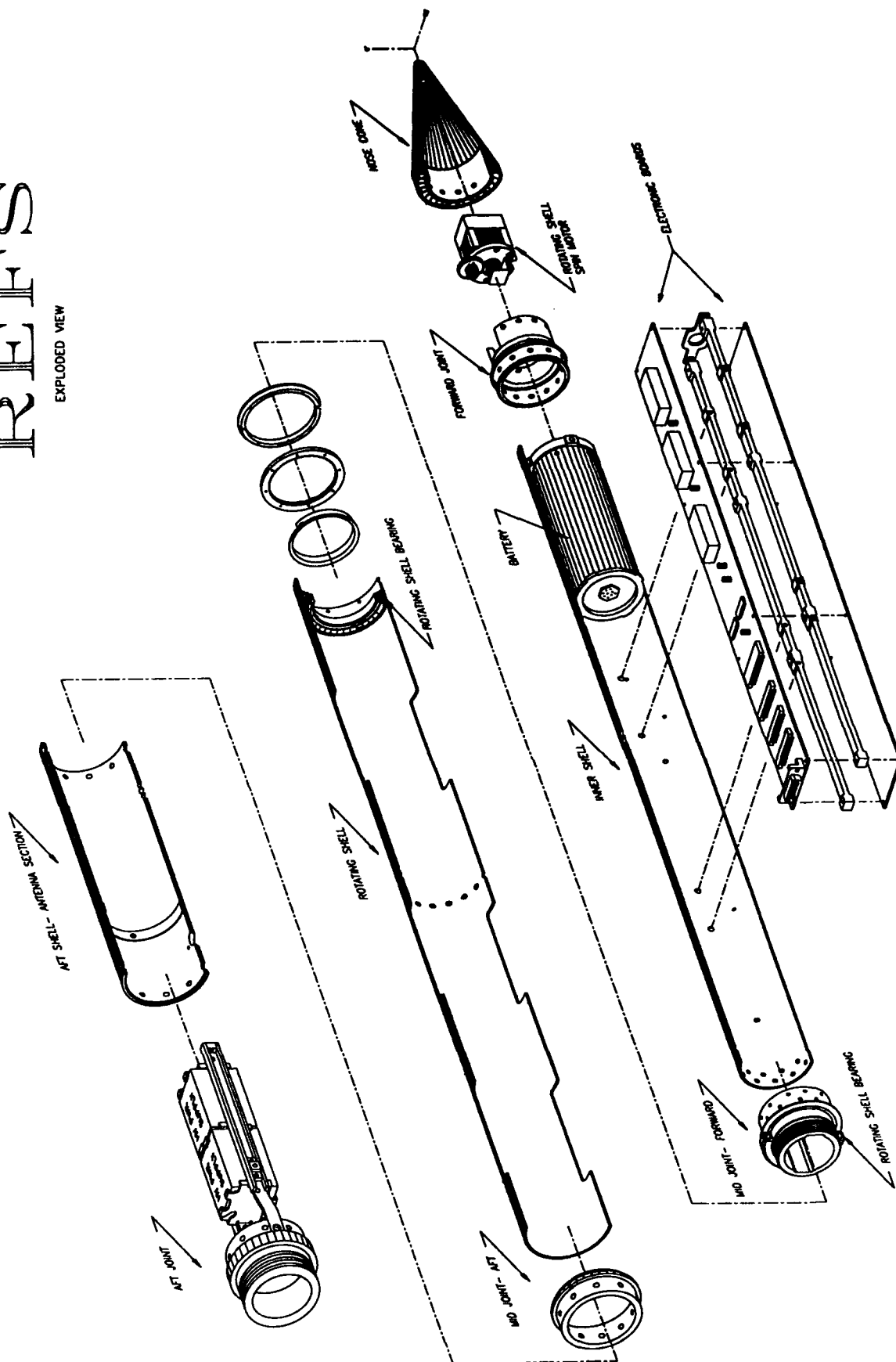
Figure 20. Exploded View of the REFS Payload, Showing all Major Structural Parts and Subsystems Except the S-band Transmitter. For actual mechanical designs and electronics diagrams, see the attached Drawings and Schematics.

39

4.1   Rocket Motor

The REFS payload was designed for launch aboard a 2.75-in. Folding Fin Aircraft Rocket (FFAR, also known as "Mighty Mouse"). This motor is 2.75 inches in diameter and 39 inches long, as measured from the end of the fins (folded) to the motor head cap. The motor was first produced in 1953 and has gone though many upgrades and revisions. Although originally designed for launch from aircraft, these motors have been fired from ground-based launchers by the NASA Wallops Flight Facility (WFF) since 1962 as a radar test rocket. The FFAR has also been used by many other organizations, including the Naval Ordnance Lab, the NASA Langley Research Center, and the Atlantic Research Corporation. The FFAR was chosen as the motor for REFS because it is inexpensive and readily available.

The type of FFAR used in support of this launch was the Mark 40, Mod 4. This rocket produces approximately 734 lbf of thrust for 1.55 seconds. The total impulse is rated at 1170 lbf-sec. The FFAR uses a single motor with 4 exhaust nozzles. The nozzle ends are cut at an angle, forming a "scarfed" edge. This scarfing causes the thrust vector from each nozzle to be slightly misaligned. This intentional thrust misalignment spins the rocket, instead of the fin misalignment more commonly used. The spin helps to stabilize the vehicle, and also reduces errors caused by inadvertent thrust misalignment.

The FFAR incorporates a set of four, symmetrically aligned, folding fins. The fins are deployed by a plunger actuator located between the nozzles. Chamber pressure during the burn phase forces the plunger out, thereby deploying the fins as soon as the rocket leaves its launch tube.

For REFS the motor was slightly modified by the addition of eight teflon bumpers glued to its sides at the top and bottom ends. These bumpers made a snug fit in the modified launch tube (see Section 4.4) while protecting the trailing corona wire from abrasion.

4.2   Rotor/Electronics Section

This section deals with the rotor/electronics section of the payload. As a point of reference in this discussion, the nose cone is considered to be forward and the rocket motor is considered to be located aft. This coordinate system applies to the entire payload. For simplicity, efforts are made to explain the payload starting from the nose cone and moving aft.

The nose cone (see Figure 21) is constructed of 6061 aluminum. It is approximately 5.5 inches long and 2.75 inches at the base, forming a 30 degree cone. The tip of the cone is not sharp but is blunted with a 0.187-inch radius. The interior is hollow to allow space for the outer shell spin motor. The payload safe/arm switch is also incorporated into the nose cone. The nose cone is attached to the inner shell using 6-32 pan head screws.

The rotor (rotating outer shell) spin-motor assembly is housed under the nose cone (see Figures 22 and 23). It consists of a 24 V DC motor, idler gear, drive gear, and mounting

Figure 21. REFS Nose Cone
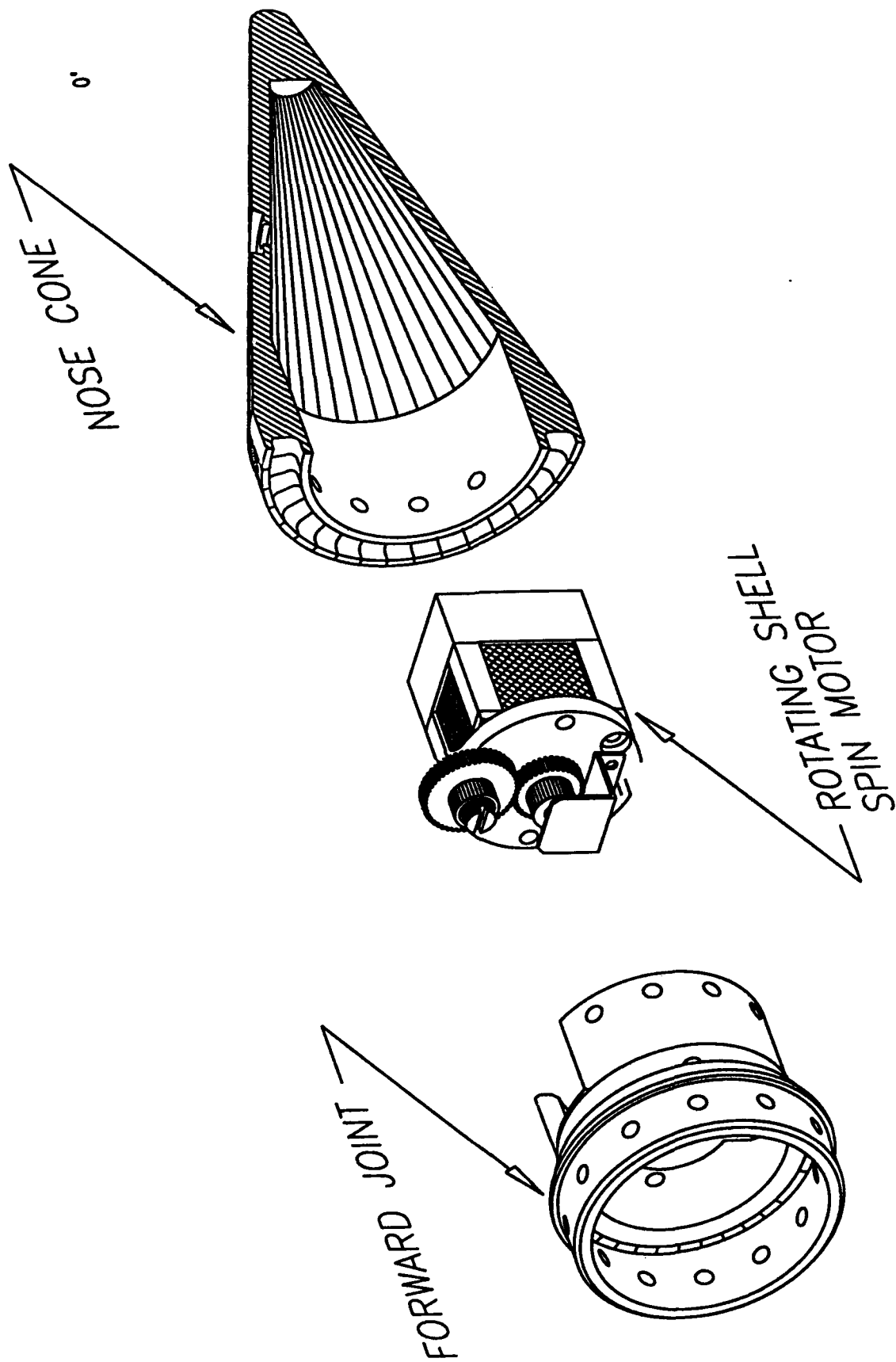
Figure 22. Detail of the Nose Cone, Forward Joint, and Spin Motor

NOSE CONE

ROTATING SHELL
SPIN MOTOR

FORWARD JOINT

42

Figure 23. Motor Mounting Plate and Gearing

bracket. The spin motor drives the rotor through the idle and drive gears. The drive gear is mounted to the motor and has 36 teeth. Power is transferred through the idler gear to a 140-tooth gear mounted on the rotor. This results in a speed reduction of 3.89 to 1 and provides 15 rps (900 rpm) to the rotor under no load. At maximum rocket velocity of about 560 m/s, this corresponds to one rotation (or two field readings) every 37 m of flight.

The rotor (see Figures 20 and 24) is a hollow aluminum cylinder 28 inches long, 2.75 inches in diameter, and 0.063 inches in wall thickness. For simplicity, a stock, "off-the-shelf" tubing was used for the rotor. This shell rotates on two bearings. The forward bearing is mounted to the rotor (see Figure 25), while the aft bearing is mounted to the mid joint (see Figure 26) so that the shell slides over it. The bearings are lubricated by an electrically conducting molybdenum disulfide grease to assure that the shell remains at ground potential. The shell is rotated by the spin motor assembly described previously, through a gear mounted to the inside diameter of the rotor.

Six "windows" or openings are present in the rotor. Each window is approximately 4 inches long (measured along cylinder) and 45 degrees of arc length wide. The windows are located in pairs, the members of each pair being 180 degrees apart (on opposite sides of the rotor). One pair is located near the forward end of the shell, the second pair is near the mid point, and the third is near the aft end. The purpose for the windows and rotation of the outer shell is to provide a "shutter" for the stators mounted on the inner shell, an essential requirement for proper operation of the field mills.

The rotation rate and position of the rotor are measured using optical sensors (photodiodes) located on the electronic boards, as described in Section 3.5. A series of sixteen 0.158 inch diameter holes is drilled in the rotor. The holes are equally spaced circumferentially around the rotor and are located between the forward and middle windows (see Figure 24, Sta. 12.875). A single 0.158-inch diameter hole is located 0.3 inch below the series of 16 (Figure 24, Sta. 13.175).

The inner shell (see Figures 20 and 27) is the support structure for the nose cone, spin motor, electronics boards, battery pack, and rotor. It is constructed of "stock" aluminum tubing, is approximately 26.7 inches long, 2.375 inches in diameter, and has a wall thickness of 0.058 inch. A total of 8 stators is mounted to the outside of the shell using a high strength epoxy. The stators are copper rectangles with an insulating backing and borders. Each stator is approximately 5.5 inches long and 1.85 inches wide, including a 3 mm insulating border on all sides. The stators are arranged in opposing pairs (that is, 180 degrees apart). Two stators are mounted near the forward (nose-cone) end of the inner shell, four stators are mounted near the middle, and the last pair is mounted near the aft (mid-joint) end. Of the four sets of stators, three pairs are arranged in line, while the fourth pair is located at the same longitudinal position as the middle pair, but rotated 90 degrees.

The stator material itself is a PTFE core sandwiched between thin copper sheeting, resembling a raw printed-circuit board. This is the same material used for the telemetry antenna described in Section 3.8. This material is quite pliable and capable of being bent to conform to the curvature of the inner shell. The stators are constructed using conventional PCB fabrication techniques.

Figure 24. Rotating Shell

45
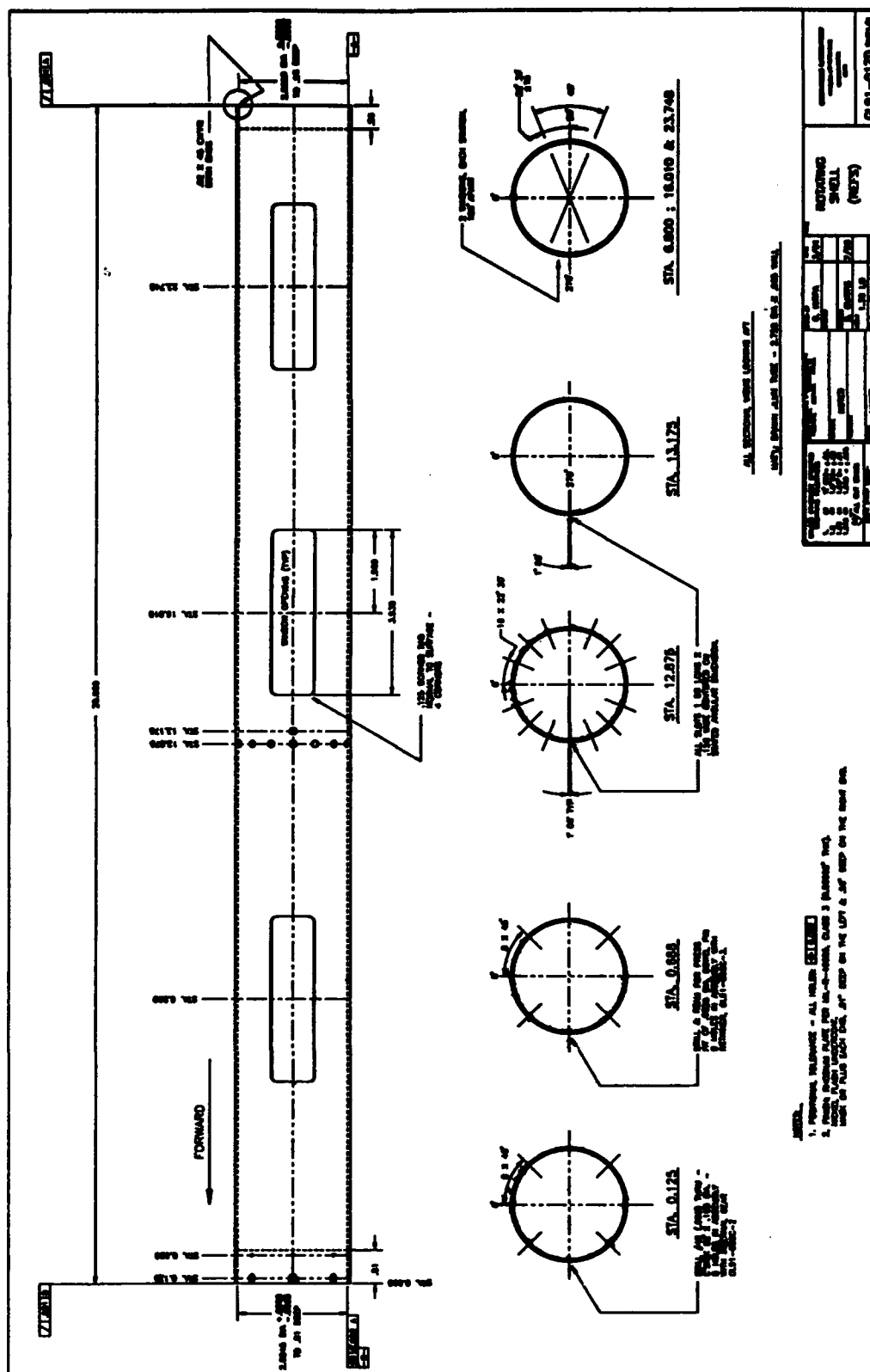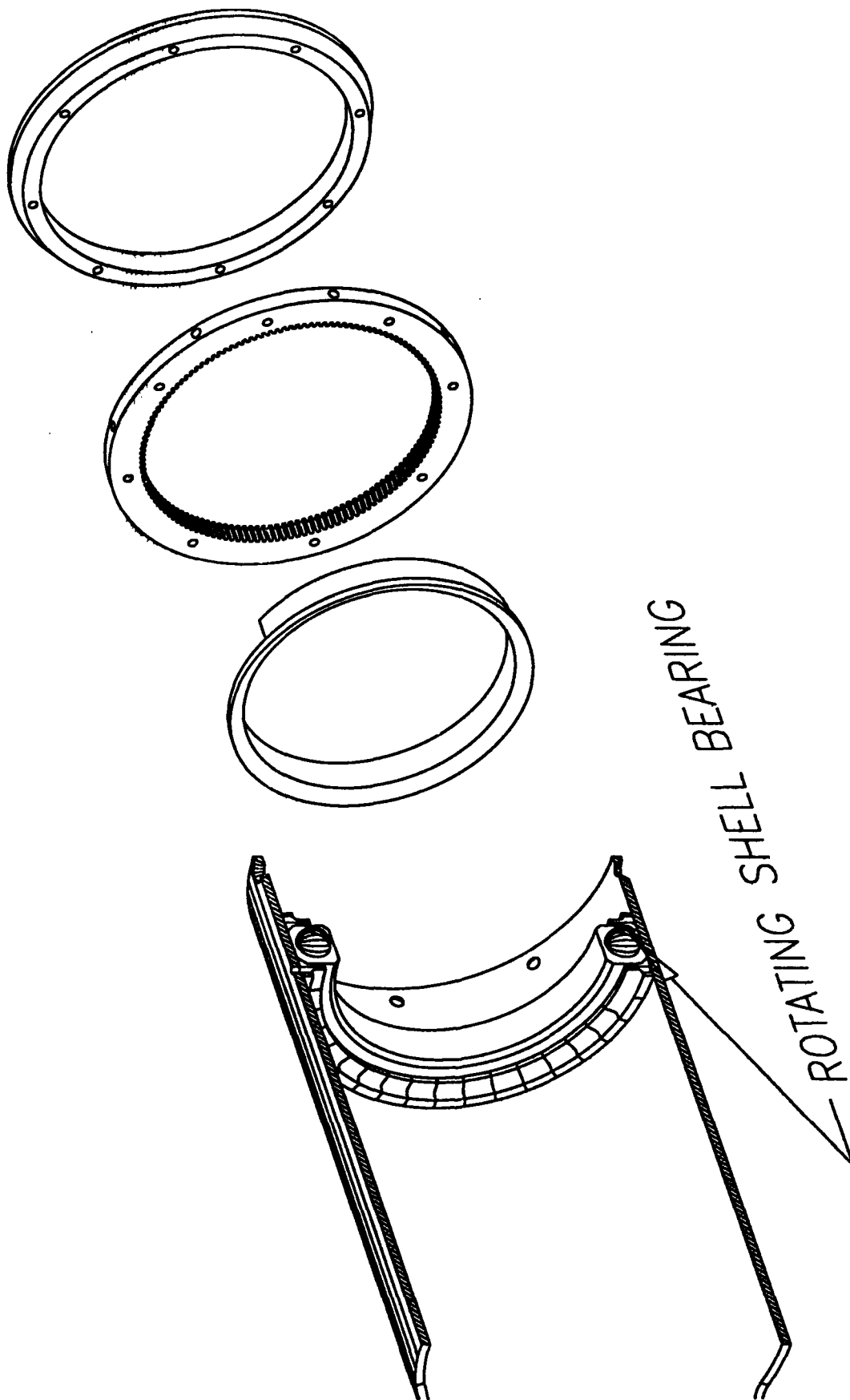
Figure 25. Detail of the Forward End of the Rotating Shell, Showing the Forward Bearing Mounting

ROTATING SHELL BEARING

MID JOINT — FORWARD

ROTATING SHELL BEARING
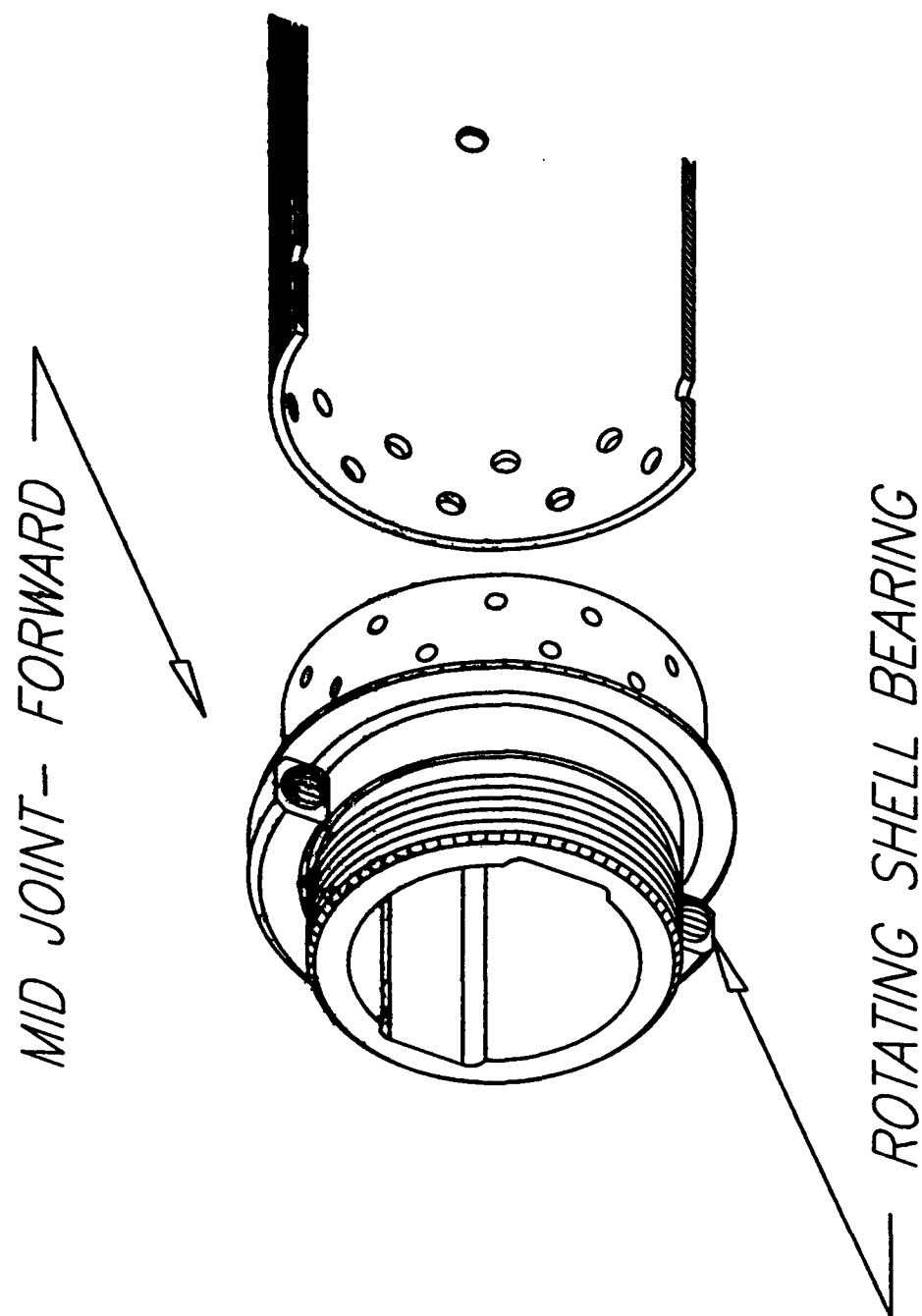
Figure 26. Detail of the Mid-joint, Showing the Mounting of the Aft Bearing and the Aft End of the Inner Shell
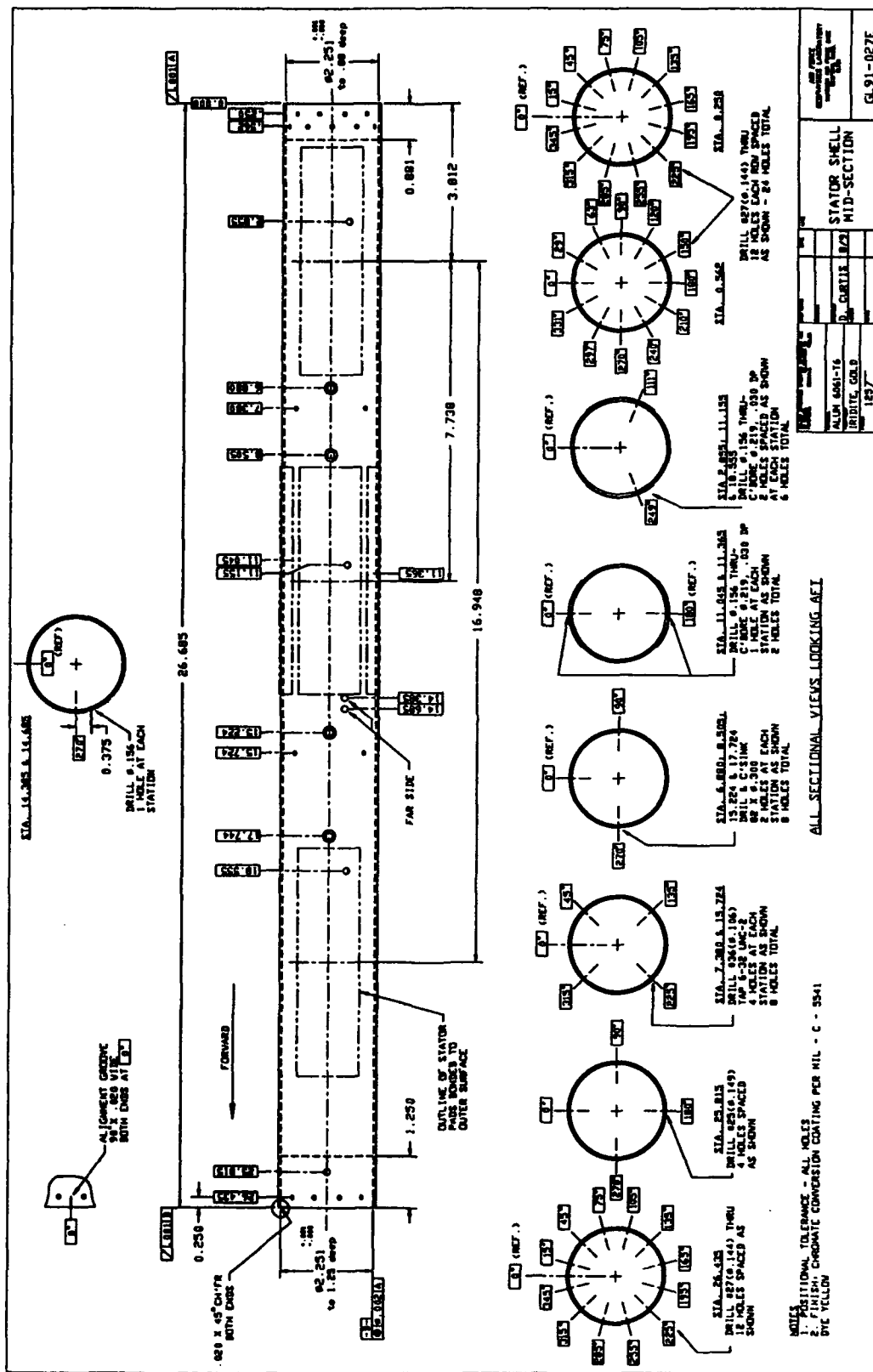
Figure 27. Stator Shell Mid-section

The battery pack is a custom-designed power source (see Section 3.10) consisting of a total of 22 individual cells of approximately 3 V each (see Figures 20 and 28). The cells are packed in a fiberglass cylinder 6 inches long and 2.25 inches in diameter. The ends are sealed with fiberglass caps that incorporate electrical connectors in each. The cells are held in place by vacuum potting the assembly with RTV-11. The battery pack is located in the forward section of the inner shell and is held in place using four 6-32 screws. It should be noted that the battery pack is designed as a self contained unit that allows easy handling and replacement.

The electronics boards are the heart of the REFS payload. They have been described in Section 3 above. Among the features incorporated into the electronics boards are a pressure transducer, a magnetic field sensor, two optical sensors (photo diodes), and an accelerometer. Note that the accelerometer measures only the component of acceleration along the thrust axis and that the magnetic field sensor gives a relative measure of only one transverse component of Earth's field.

The two electronic boards are attached on opposite sides of two aluminum "rails," and each of these rails is then held in place inside the inner shell using four 6-32 flat head screws (see Figure 20). The boards are located below the battery pack and take up the remaining space inside the inner shell. Connections to the stators are made by 2-56 screws that pass through the stators and thread into rigid pick-offs mounted on the boards themselves. This was done to eliminate any spurious signals induced by vibration of interconnecting wires.

4.3   High Voltage Section

The outer shell of the high voltage section is constructed of 6061 aluminum (see Figure 29). It is approximately 10 inches long and 2.75 inches in diameter. The S-band telemetry antenna is set into a wide groove machined in the surface of the HV section so that the antenna is flush with the surface of the payload, thereby providing low drag and no sharp edges to go into corona. The antenna is held in place using high strength epoxy and 2-56 pan head screws.

The internal electronics and hardware of the high voltage section are all mounted to a structure that is attached to the aft joint (see Figures 30 and 31). The aft joint acts not only as a base for the HV internal structure but also as a connection to the rocket motor. This allows the entire internal assembly, which includes the transmitter, umbilical connector, HV power supplies, and HV relays to be removed from the HV outer shell as a unit.

The S-band transmitter is located furthest forward in the HV section (not shown in Figures 20 or 30). It is attached to a small plate that is in turn mounted to the internal support structure. A thermally conductive grease is used between the transmitter and the plate to increase heat dissipation from the transmitter to the rest of the structure.

The high voltage power supplies are held between holding plates. The plates are then attached to the support structure using 4-40 pan head screws (see Figure 30).

Figure 28. Battery Container Assembly

50
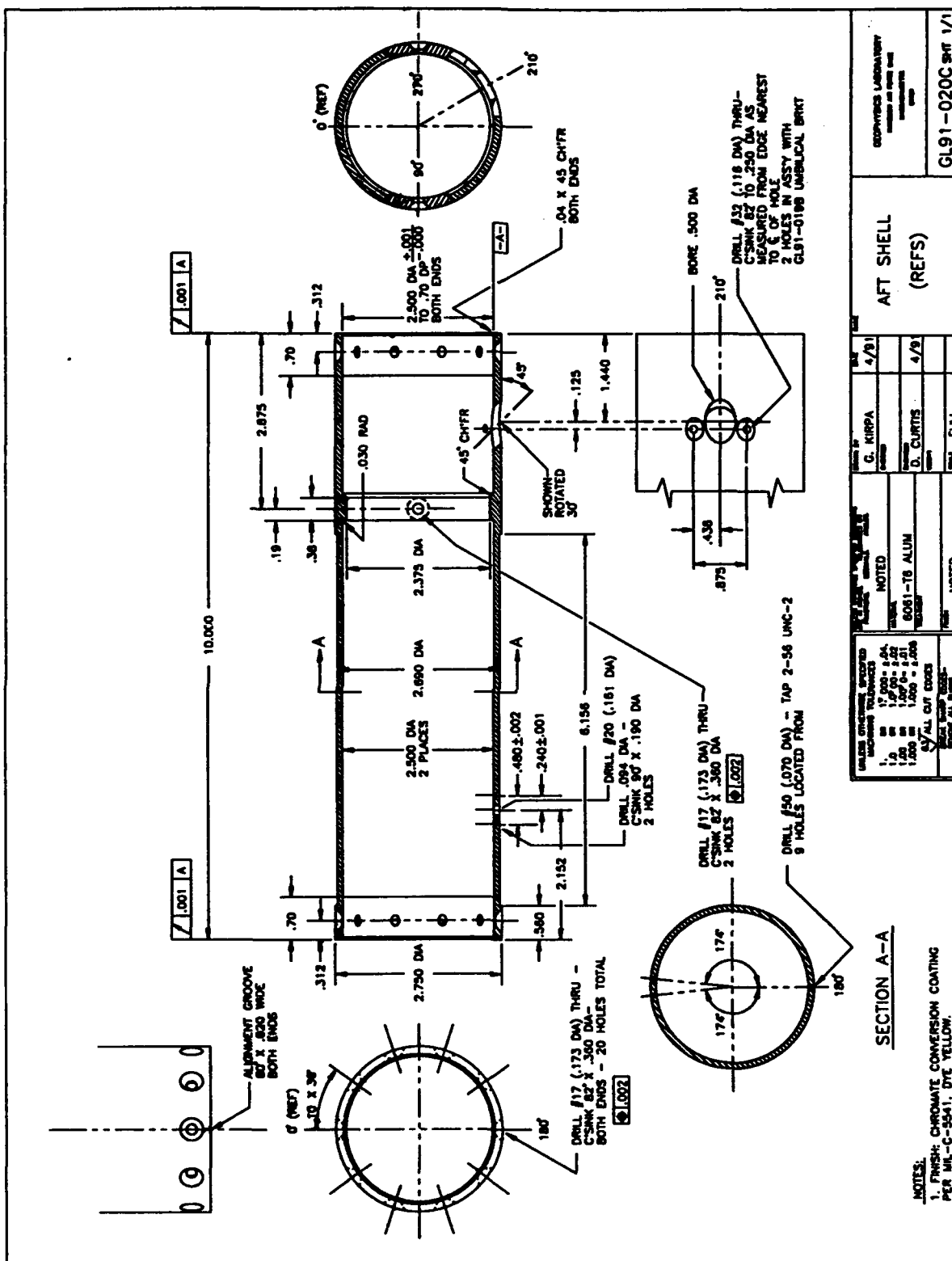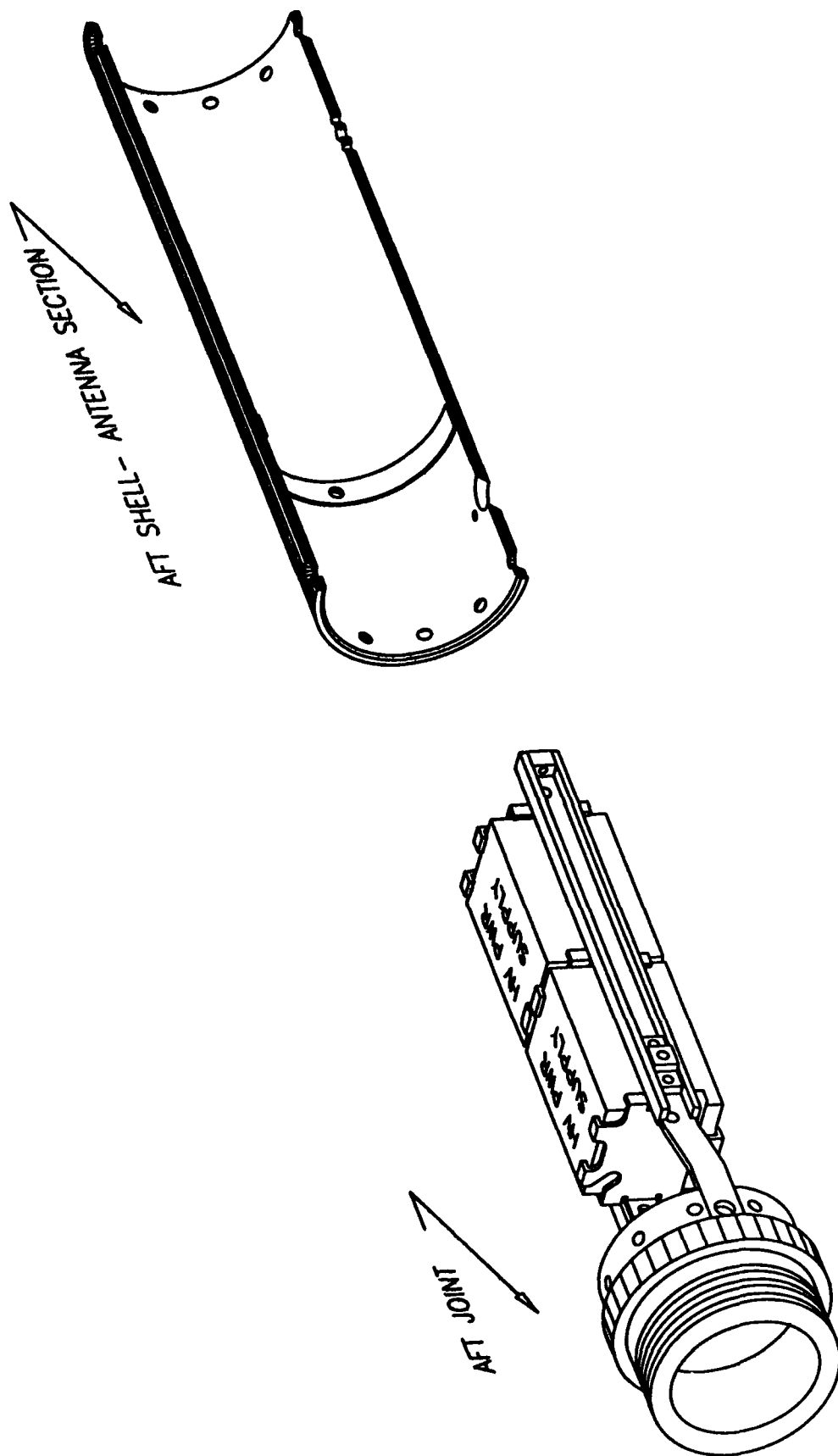
Figure 29. Aft Shell

Figure 30. Detail of the High-voltage Section, Showing the Aft Joint, Mounting Brackets for the High-voltage Power Supplies and S-band Transmitter (not Shown), and the Aft Shell That Carries the Telemetry Antenna

Figure 31. Base Ring Aft Section

The umbilical connector (not shown in Figure 30) is attached to the support structure below the high voltage power supplies. A mounting bracket (see Figure 32) is used to hold the connector in a location such that, when the HV assembly is slid into the HV outer shell, the connector lines up with a hole in the shell (see Figure 29). Screws are then used to fasten the connector to the shell.

The high voltage trailing wire (not shown in Figure 20) exits the HV section through a hole in the aft joint (see Figure 31). The wire travels down the side of the rocket motor and terminates beyond the rocket nozzles. The wire is held in place along the rocket surface with aluminum tape.

The mid joint (Figure 26) is considered a prominent structural member. Much consideration went into the design of this section. Because of the high bending moment experienced during flight and the thin walls of the inner shell, stainless steel was chosen over aluminum for this joint. The stainless steel, while heavier than aluminum, provides significantly more strength, leading to a less bulky design. Analysis of this joint also led to the high number of screws used to secure the inner shell to the joint.

4.4   Launcher

The launcher used for the first flight was supplied by WFF but was modified for use with the REFS program. The launcher is a two-tube design, the tubes being mounted to opposite ends of a horizontal boom approximately 3 ft long.

A special launch tube was fabricated by PL for use with the REFS rocket. The major difference between this tube and the standard launch tube is the inside diameter. The original tubes are approximately 2.85 inches inside diameter, whereas the REFS launch tube is 3.125 inches inside diameter. This larger diameter accommodates the high-voltage trailing wire and motor bumpers that protect it (see Section 4.1).

The new launch tube was mounted between the two existing tubes using brackets supplied by PL. Since the REFS tube was only as long as the rocket motor, the entire payload extended above the launch tube. This allowed free access to the umbilical connector; no specialized hardware was required for the umbilical to pull away from the rocket. The umbilical line was simply taped to the side of the launch tube, so that the rocket pulled the plug from the connector as the rocket was launched.
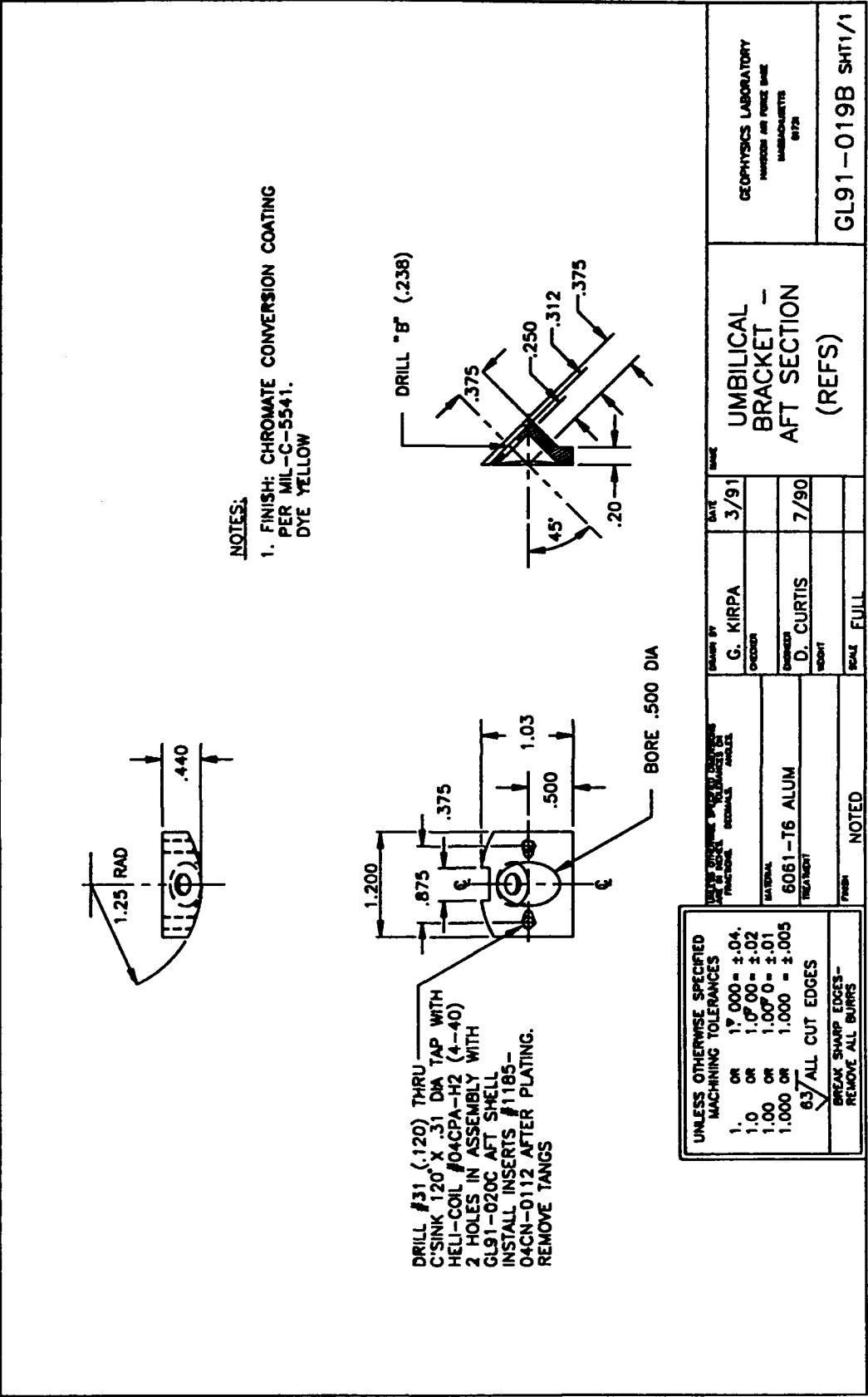
Figure 32. Umbilical Bracket - Aft Section

Figure 33. Forward Ring Mid-section
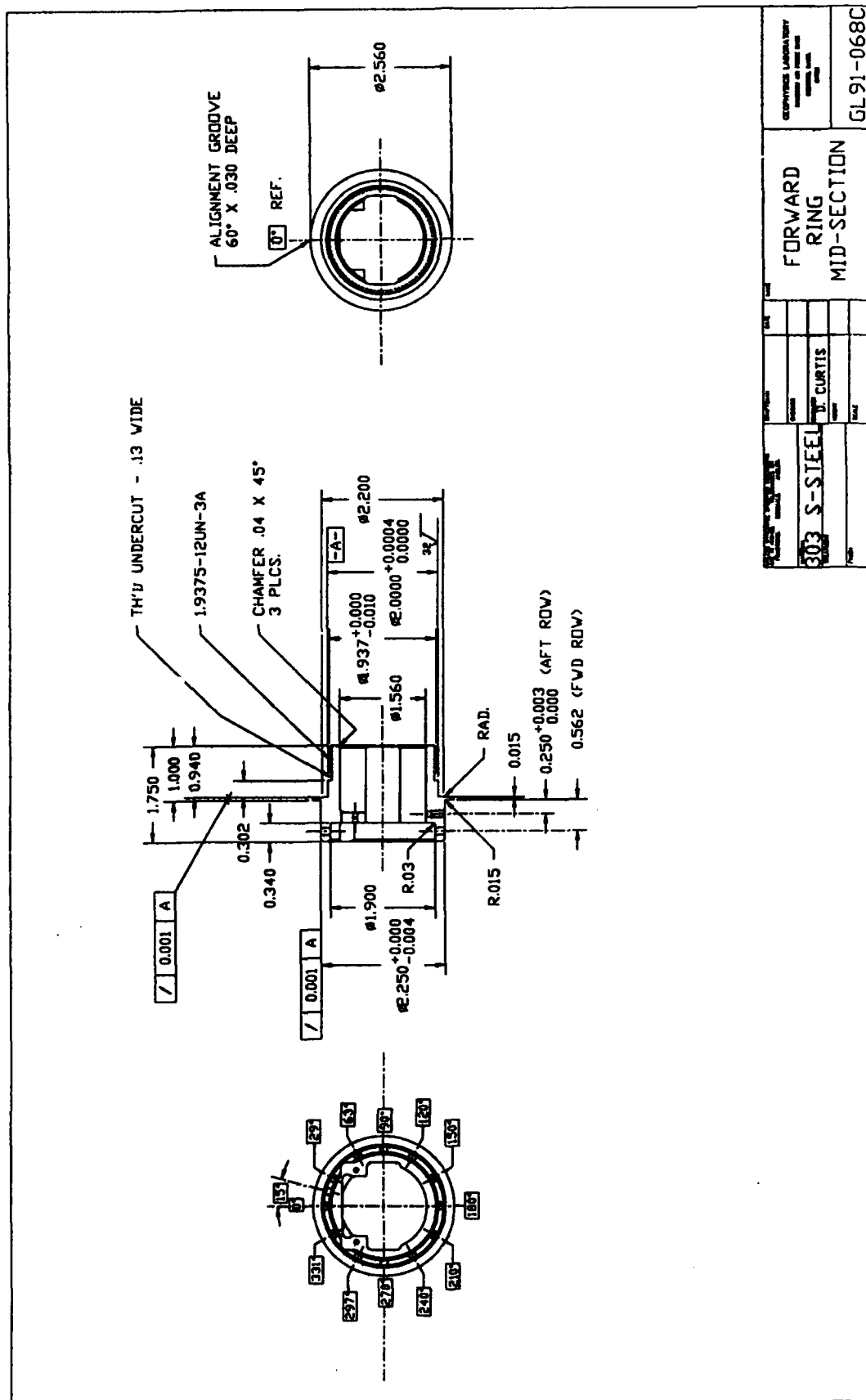
5. PRE-FLIGHT AERODYNAMIC ANALYSIS

Before NASA allows the REFS vehicle to be launched at KSC, a complete pre-flight analysis of the aerodynamic stability and performance is necessary to determine the impact point. The impact point at KSC is critical and must be in a lagoon that is situated between the RTLP launch pad and a public beach. Since the FFAR had never been flown with the REFS payload, KSC also requested that preliminary launches be performed at WFF.

The pre-flight analysis for a KSC launch was performed by Capt Carl Frushon and Capt Robert Longstreth, both of PL/SXA, with much help from Dr. George Jumper, of the Worcester Polytechnic Institute. The pre-flight analysis for the WFF launch was performed by Capt Longstreth and Dr Jumper. The analysis was performed in three parts:

1. Computation of the mass properties of the 2.75-inch FFAR and REFS payload using the Mass Properties program (MASSPROP) written by Capt C.J. Frushon of PL/SXA.
2. Determination of the aerodynamic stability derivatives using the USAF Missile DATCOM program,[28] which was written for the Flight Dynamics Laboratory, Wright-Patterson AFB.
3. Prediction of performance and trajectory using the NASA Goddard Space Flight Center Missile and Satellite Simulation program[29] (MASS). Note: To avoid confusion with MASSPROP, we refer to MASS as SOAR (Simulation Of A Rocket). This practice will be followed throughout this report.

Once the initial prediction of impact point was made, a complete dispersion analysis and sensitivity study was done to study the effects of different uncontrollable variables. The results of this study have been included in the discussion of the performance prediction.

5.1   Computation of the Mass Properties

The mass properties of the REFS rocket were computed for two cases. The first case has a fully loaded motor, and the second case has an expended motor. MASSPROP computes mass properties by breaking the entire structure up into geometrically simple shapes, computing the properties of each of these shapes, and then combining the properties back into a single structure. Because of the complexity of both the REFS payload and the FFAR, the entire REFS

---

[28] Nielsen, J.N., (1960) *Missile Aerodynamics*, McGraw-Hill Book Company, Inc., New York.

[29] AVCO, (1974) *MASS Program User's Manual*, prepared for NASA Goddard Space Flight Center, Greenbelt, MD, under Contract NAS5-23231, by AVCO Systems Division, Maryland Operations, Seabrook MD.

vehicle was broken up into 41 and 42 pieces for the loaded and expended cases respectively. A summary of the mass properties is given in Table 2.

Table 2. Summary of REFS Mass Properties

Full Motor Properties	Expended Motor Properties
CGX = 44.1261 in CGY = -0.0069 in CGZ = -0.0037 in MASS = 24.8870 lbs Ixx = 0.00496 slug-ft^2 Iyy = 2.14652 slug-ft^2 Izz = 2.14651 slug-ft^2 Pxy = -0.000257 slug-ft^2 Pxz = -0.000193 slug-ft^2 Pyz = -0.000257 slug-ft^2	CGX = 38.4369 in CGY = -0.0092 in CGZ = -0.0049 in MASS = 18.5759 lbs Ixx = 0.00363 slug-ft^2 Iyy = 1.51401 slug-ft^2 Izz = 1.51400 slug-ft^2 Pxy = -0.000047 slug-ft^2 Pxz = -0.000081 slug-ft^2 Pyz = -0.000047 slug-ft^2
Note: All measurements are referenced to the origin at the nose tip with the +X axis pointing toward the tail along the longitudinal axis. CG stands for center-of-gravity, and the Is and Ps are the diagonal and off-diagonal elements of the moment of inertia.	

5.2 Determination of the Aerodynamic Stability

The major aerodynamic stability derivatives were determined using the Missile DATCOM computer program. The Missile DATCOM program uses numerical techniques to compute derivatives for axisymmetric or elliptical bodies operating in subsonic, transonic, or supersonic flight regimes. The Missile DATCOM derivatives used in the REFS Program were:

Cx   -   The axial force coefficient.
CNa   -   The normal force coefficient with respect to angle of attack.
Cma   -   The pitch coefficient with respect to angle of attack.
Xcp   -   The center of pressure.

These DATCOM derivatives are for the body and fin combination. DATCOM additionally computes body-only and fin-only derivatives that are used by the program to compute the combination values. Other derivatives were computed by hand using traditional aerodynamic methods. These derivatives were:

CMq   -   The pitch coefficient with respect to pitch velocity (the "pitch-damping" derivative).

Clp   -   The rolling moment coefficient with respect to roll rate.

Mj   -   The "jet-damping" coefficient.

Cld   -   The lift coefficient of the fins with respect to the angle of attack of the fins. (Since the fins and fin set are symmetrical, this was set to zero)

All the derivatives vary with Mach number and the angle of attack. Typical values of the derivatives are shown in Table 3.

Table 3. Aerodynamic Stability Derivatives

```
Cx  = 0.4920 to  1.1680
CNa = 0.1874 to  0.1988 /deg
Cma = -0.9219 to -3.116 /deg
Xcp = 47.265 to 69.144 inches from nose
CMq = -11700 to -16500 /rad
Clp = -0.667
Mj  = -0.606  to -1.1998 ft-lb/rad
Cld = 0
S.M.= -10.3 to -4.9 body diameters
```

The "static margin" (S.M. = CGX - Xcp) shows that the REFS vehicle is much more stable than necessary. As a rule of thumb, the center of pressure should be between one and two body diameters below the center of gravity. Larger static margins result in "weather-cocking" -- the tendency of a rocket to turn into the wind like a weather vane. This should tend to increase the impact dispersion.

5.3 Predicted Performance and Dispersion Analysis

SOAR is a complex, six-degree-of-freedom, rocket-simulation program. It models the trajectory in three dimensions and the orientation of the vehicle (pitch, yaw, and roll relative to the velocity vector) as a function of time, including both rigid-body mechanics and aerodynamic forces. Thus, it is able to simulate the effects of the spin induced by the scarfed nozzles on the FFAR motor and the reaction to an arbitrary ambient wind profile. Following the creation of the SOAR input deck, several simulations were run to determine a nominal trajectory and the effect of varying some of the rocket and environmental parameters. The parameter variations were chosen to represent the typical uncertainties used in sounding-rocket-dispersion studies, as listed in Table 4.

Table 4. Dispersion Analysis Summary

Parameter	Amount Varied
East Wind	+ 10 kt
West Wind	+ 10 kt
North Wind	+ 10 kt
South Wind	+ 10 kt
Elevation Angle	+ 1 deg
Elevation Angle	- 1 deg
Azimuth Angle	+ 1 deg
Azimuth Angle	- 1 deg
Thrust	+ 10 %
Thrust	- 10 %
Weight	+ 1 lb
Weight	- 1 lb
Drag (Cx)	+ 10 %
Drag (Cx)	- 10 %
Spin (entire rocket)	+ 10 %
Spin (entire rocket)	- 10 %
Pitching Moment (Cma)	+ 10 %
Pitching Moment (Cma)	- 10 %
Center of Gravity (Xcg)	Back 10 %
Center of Gravity (Xcg)	Forward 10 %
Thrust Misalignment (See text)	2 deg

Note that SOAR does not simulate the effects of the rotating shell on the REFS payload. Dr. George Jumper performed a separate analysis of the aerodynamics (primarily the "Magnus effect") induced by the relative rotation of rocket body and shell. The conclusion was that the effects were negligible under the REFS operating conditions.

Note that the FFAR motor (see Section 4.1) was modeled using five nozzles, one center nozzle and four surrounding nozzles. The center nozzle provided the total axial thrust specified for the FFAR. The four surrounding nozzles were oriented such that they provided thrust normal to the velocity vector and tangential to the motor shell, imparting spin to the rocket. The thrust of each of these "spin motors" was set at 0.2 percent of the axial thrust, a value found to reproduce the observed spin at burnout. For the dispersion analysis, thrust misalignment was modeled by misaligning only the center nozzle. It is felt that this nozzle model allows a better simulation of manufacturing errors than a direct representation of the four scarfed nozzles.

Note also that the analysis described here assumes a KSC launch. The actual test launch was from WFF, which has a different longitude and latitude. Thus the tabulated geographic coordinates of the impact points do not correspond to the actual flight. Nevertheless, the apogee and range values given below are almost exactly those that would be predicted assuming a WFF launch. This is because the difference in Coriolis parameter between the two sites results in a trivial difference in trajectories for such a short flight.

Table 5 gives the key results from two series of model runs. The first series is for different wind velocities, to illustrate the wind sensitivity, and different launch elevation angles (QE), to determine the optimum launcher setting. These runs were not used in the dispersion analysis. The second series is for the parameter variations making up the dispersion analysis, based on Table 4 above. For all of these runs, the launch azimuth was due East, so that a West wind is directed down range.

Table 6 gives the results of the dispersion analysis. "TH" indicates a variation in average thrust, with a corresponding change to total impulse. "WT" is a change in payload weight. "Spin" is a variation of the roll-torque component of the thrust. "Th. Misalign." is a misalignment of the axial thrust by 2 degrees. Predictions were made for both plus and minus amounts, but only the worse case was reported in Table 6 and used in determining the Root-Sum-Square (RSS) amount.

The 1-sigma (68 percent certainty) parameter ranges assumed for this analysis were based on conventional wisdom, as indicated above, and on our best judgment at the time. Dispersion calculations were also performed for other launcher elevation angles. Based on all this analysis it appears that, even with a 3-sigma (99 percent certainty) dispersion, a due East launch of no greater than 80 degrees elevation would be safe, provided that the surface winds did not exceed 10 knots in any direction.

Table 5. GL REFS 2.75-inch QE = 75 Degrees
Representative Trajectories

QE (deg)	WINDS (knots)	MAXIMUM ALTITUDE (ft)	RADIAL RANGE (ft)	LATITUDE (deg)	LONGITUDE (deg)	IMPACT CROSS RANGE (ft)	IMPACT DOWN RANGE (ft)
75	No Winds	15551	12504	28.3997	-79.9610	-109	12516
75	East 10.0	15044	13667	28.3998	-79.9574	-73	13671
75	West 10.0	15976	11163	28.3997	-79.9652	-109	11168
75	North 10.0	15500	12560	28.4045	-79.9612	1642	12451
75	South 10.0	15498	12580	28.3950	-79.9612	-1824	12452
75	East 20.0	14460	14656	28.3998	-79.9543	-73	14666
75	West 20.0	16308	9645	28.3997	-79.9699	-109	9660
75	North 20.0	15343	12740	28.4092	-79.9617	3356	12290
75	South 20.0	15339	12779	28.3903	-79.9617	-3539	12292
80	No Winds	16196	8673	28.3998	-79.9730	-73	8665
70	No Winds	14691	15839	28.3997	-79.9506	-109	15854

QE (deg)	DISPERSION PARAMETER	MAXIMUM ALTITUDE (ft)	RADIAL RANGE (ft)	LATITUDE (deg)	LONGITUDE (deg)	IMPACT CROSS RANGE (ft)	IMPACT DOWN RANGE (ft)	DELTA CROSS RANGE (ft)	DELTA DOWN RANGE (ft)
75	Baseline	15551	12504	28.3997	-79.9610	-109	12516	---	---
75	East 10.0	15044	13667	28.3998	-79.9574	-73	13671	36	1155
75	West 10.0	15976	11163	28.3997	-79.9652	-109	11168	0	-1348
75	North 10.0	15500	12560	28.4045	-79.9612	1642	12451	1751	-65
75	South 10.0	15498	12580	28.3950	-79.9612	-1824	12452	-1715	-64
76	QE + 1 deg	15699	11776	28.3997	-79.9633	-109	11778	0	-738
75	AZ + 1 deg	15552	12506	28.3991	-79.9610	-328	12516	-219	0
75	TH + 10%	16361	12944	28.3997	-79.9597	-109	12933	0	417
75	WT - 1 lb	15425	12143	28.3998	-79.9622	-73	12131	36	-385
75	DG - 10%	15552	12506	28.3997	-79.9610	-109	12516	0	0
75	Spin + 10 %	15540	12498	28.3997	-79.9611	-109	12484	0	-32
75	CMa + 10 %	15551	12508	28.3997	-79.9610	-109	12516	0	0
75	CMa - 10 %	15553	12500	28.3997	-79.9611	-109	12484	0	-32
75	CG Back 10 %	12552	12505	28.3997	-79.9610	-109	12516	0	0
75	Th. Misalign.	15532	12600	28.4000	-79.9607	0	12612	109	96

Table 6. GL REFS 2.75-inch QE = 75 Degrees Dispersion

Dispersion Parameter	Delta Cross Range (ft)	Delta Down Range (ft)
West 10.0	36	–1348
North 10.0	1751	–65
QE + 1 deg	0	–738
AZ + 1 deg	–219	0
TH + 10%	0	417
WT – 1 lb	36	–385
DG – 10%	0	0
Spin + 10%	0	–32
CMa – 10%	0	–32
CG Back 10%	0	0
Th. Misalign	109	96
RSS	1769	1643

Following the completion of the dispersion analysis for a KSC launch, a no-wind prediction was made for a WFF launch, again assuming due East azimuth and an elevation angle of 75 degrees. The apogee, impact range, and impact coordinates for this simulation are listed below. Evidently, the trajectory is almost identical to that predicted above for a KSC launch.

Apogee(ft)	15552
Range (ft)	12505
Impact Lat. (deg)	37.8382
Impact Long.(deg)	-75.4433

The following pages show all of the input data to the SOAR program that was used to predict the WFF launch performance. It has been included for completeness. If further information is needed about the input data format, syntax, etc., the SOAR (MASS) manual should be consulted.

```
*       2.75 FFAR Model - 6 DOF - REFS Baseline for WFF Launch
*       Five Thruster Model Baseline
*
*
X17*    NUMBER OF TABLES
$
X51*      Table 1:  THRUSTING Cx (Ref: Missile Datcom)
F1,0*    no z -
F23,1*   23 mach numbers
F0.,0.1,0.2,0.3,0.4,0.5,0.6,0.7,0.8,0.9,1.0*    Mach numbers
F1.1,1.2,1.3,1.4,1.5,1.6,1.7,1.8,1.9,2.0,2.5,3.0*
F0.0*    dummy y
F0.6110,0.6110,0.5570,0.5290,0.5100,0.4960,0.4840,0.4790*  Cx
F0.5000,0.5520,0.6960,0.8270,0.9750,0.9380,1.2080,1.5560*
F1.5010,1.3690,1.2210,1.1330,1.0620,0.8460,0.7170*
$
X51*      Table 2:   CN alpha (/deg) (Ref: Missile Datcom)
$ (Note:  Use /deg to /rad scale factor 180/c)
F1,0*      no z
F23,1*   23 mach numbers
F0.,0.1,0.2,0.3,0.4,0.5,0.6,0.7,0.8,0.9,1.0*    Mach numbers
F1.1,1.2,1.3,1.4,1.5,1.6,1.7,1.8,1.9,2.0,2.5,3.0*
F0.0*    dummy y
F0.1647,0.1647,0.1667,0.1703,0.1759,0.1838,0.1955,0.2211*  CN alpha
F0.2288,0.2394,0.2944,0.2515,0.2355,0.2430,0.2078,0.2016*
F0.1934,0.1850,0.1784,0.1725,0.1688,0.1398,0.1171*
$
X51*      Table 3: XCp   (in frm nose) (Ref: Missile Datcom)
F1,0*  no z
F23,1*   23 mach numbers
F0.,0.1,0.2,0.3,0.4,0.5,0.6,0.7,0.8,0.9,1.0*    Mach numbers
F1.1,1.2,1.3,1.4,1.5,1.6,1.7,1.8,1.9,2.0,2.5,3.0*
F0.0* Dummy y
F59.192,59.700,59.931,60.330,60.908,61.709,62.733,64.582*   CP
F65.062,65.068,66.786,67.383,69.144,63.885,59.571,58.846*
F57.035,55.891,54.770,53.690,52.822,48.328,47.265*
$
X11*      Table 4:  Cm q (/rad)   (Based on CN')
F1,0,3,1*  Linear change from start to burnout then const.
F0,1.551,100.*     Times
F0.0*  Dummy y
F-11700,-16500,-16500*
$
X11* Table 5:  XCG vs time (in frm nose) (Ref: NASA Wallops & CF)
F1,0,3,1*  Linear change from start to burnout then const.
F0,1.551,100.*     Times
F0.0*  Dummy y
F41.905,35.905,35.905*
$
X11*    Table 6:  Prop. Weight vs Time (Lbs) (Ref. NASA Wallops)
F1,0*   1d table
F3,1*   3 time values - linear start to burnout, then zero
F0,1.551,100.*  Time values
F0.0*  Dummy y
```

```
F6.4,0.,0.*
$
X11*    Table 7:  Iyy vs. time
F1,0*  no z
F3,1*  3 times - dummy y
F0.0,1.551,100.*  times
F0.*  dummy y
F2.14652,1.51401,1.51401*  Iyys
$
X15*        Table 8:  Thrust vs Time (Ref: Picatinny)
F1,0*  no z
F5,1*  5 time entries (s) - no y  (1d table)
F0.,0.01,1.55,1.551,100.*  Time (s)
F0.*  dummy y value
F734.,734.,734.,0.,0.*  Thrusts (lb)
$
X51*    Table 9:  Coasting Cx - same as Thrusting (Table 1)
F1,0*    no z -
F23,1*    23 mach numbers - 1 dummy y
F0.,0.1,0.2,0.3,0.4,0.5,0.6,0.7,0.8,0.9,1.0*    Mach numbers
F1.1,1.2,1.3,1.4,1.5,1.6,1.7,1.8,1.9,2.0,2.5,3.0*
F0.0*    dummy y
F0.6110,0.6110,0.5570,0.5290,0.5100,0.4960,0.4840,0.4790*  Cx
F0.5000,0.5520,0.6960,0.8270,0.9750,0.9380,1.2080,1.5560*
F1.5010,1.3690,1.2210,1.1330,1.0620,0.8460,0.7170*
$
X33*    Table 10:  Cn alpha/ D (NOT USED)
F1,0,14,1*
F0,.4,.8,1,1.2,1.5,2,3,4,5,6,7,8,9,0*
F2.08,2.107,2.168,2.21,2.193,2.68,2.127,1.848,1.568,1.445,1.323,1.289*
F1.254,1.241*
$
X9*        Table 11:  Winds
F1,0*  no 3rd component
F2,1*  2 x, no y
F0.,1000000.*  altitudes (ft)
F0.*  dummy y value
F-1.6878,-1.6878*  wind speed (ft/sec to knot conversion to allow F994 to be kts.)
$
X99*        Table 12:  Cm alpha (/deg - use multiplier for /rad)
F1,0*  no z
F23,3*    23 mach numbers
F0.,0.1,0.2,0.3,0.4,0.5,0.6,0.7,0.8,0.9,1.0*    Mach numbers
F1.1,1.2,1.3,1.4,1.5,1.6,1.7,1.8,1.9,2.0,2.5,3.0*
F0.0,1.55,100.*    three times
F-0.9192,-0.9192,-0.9444,-0.9891,-1.0580,-1.1580,-1.3040,-1.6210*  Cma (t=0.0)
F-1.7170,-1.7970,-2.3910,-2.5150,-2.1120,-1.7210,-1.1500,-1.0640*
F-0.8950,-0.7800,-0.6804,-0.5914,-0.5199,-0.2106,-0.1318*
F-1.2550,-1.2550,-1.2840,-1.3370,-1.4170,-1.5330,-1.7020,-2.0720*  Cma (t=1.55)
F-2.1840,-2.2850,-2.9920,-2.6090,-2.5920,-2.2170,-1.5740,-1.4750*
F-1.2890,-1.1570,-1.0440,-0.9434,-0.8601,-0.4957,-0.3706*
F-1.2550,-1.2550,-1.2840,-1.3370,-1.4170,-1.5330,-1.7020,-2.0720*  Cma (t=100.0)
F-2.1840,-2.2850,-2.9920,-2.6090,-2.5920,-2.2170,-1.5740,-1.4750*
F-1.2890,-1.1570,-1.0440,-0.9434,-0.8601,-0.4957,-0.3706*
$
```

```
X11*        Table 13:  Ixx
F1,0*    no z
F3,1*  3 times - dummy y
F0.0,1.551,100.*  times
F0.0*  dummy y
F0.00496,0.00363,0.00363*  Ixxs
$
X13*        Table 14:  Y and Z Jet Damping (ft-lb/(rad/s))
F1,0*    no z                          !
F4,1*  4 times - dummy y
F0.0,1.55,1.551,100.*  times
F0.0*  dummy y
F-0.606,-1.1998,0.,0.*  damping coef
$
X51*        Table 15:  XCP of Fin Set
F1,0*    no z
F23,1*  23 mach numbers - 1 dummy y
F0.,0.1,0.2,0.3,0.4,0.5,0.6,0.7,0.8,0.9,1.0*    Mach numbers
F1.1,1.2,1.3,1.4,1.5,1.6,1.7,1.8,1.9,2.0,2.5,3.0*
F0.0*  dummy y
F41.79,41.79,41.79,41.79,41.79,41.79,41.78,41.78,41.78*  X cp
F41.77,41.70,41.92,42.03,42.11,42.18,42.24,42.29,42.31*
F42.30,42.29,42.28,42.24,42.22*
$
X39*     Table 16:  Cl delta
F1,0*    no z
F17,1*    17 Mach numbers - 1 dummy y
F0.,0.1,0.2,0.3,0.4,0.5,0.6,0.7,0.8,0.9,1.0*    Mach numbers
F1.2,1.4,1.5,2.0,2.5,3.0*
F0.0*  dummy y
F16.5,16.52,16.60,16.74,16.93,17.19,17.52,17.95,18.49*  Xld
F19.17,20.04,22.6,22.45,18.57,11.8,9.07,7.50*
X35*        Table 17:  Clp
F1,0*    no z
F15,1*    17 Mach numbers - 1 dummy y
F0.,0.1,0.2,0.3,0.4,0.5,0.6,0.7,0.8,0.9,1.0*    Mach numbers
F1.5,2.0,2.5,3.0*
F0.0*  dummy y
F52.30,52.38,52.63,53.05,53.66,54.49,55.55,56.60,58.60*  Clp's
F60.76,63.52,53.56,36.42,28.24,23.39*
$
$ ------ End of Tables --------
$
$ Start of Phase 1   (Ignition to Tube Exit) -------
$
X1,0*  normal mode, zero A array
 2.75 FFAR   to Tube Exit
X0,141,39,0,0,0,2$  Phase 1 input params 600F
$ (no shifts, 133 inputs and 38 table controls)
$
$    Data shifting inputs - none ------
$
*    A-Array inputs ----------
$
$
```

66

```
$ -------  Initial Conditions for Phase 1 --------
$
F100,0.0$      Clock starts at 0.s.
F64,2$         Position input option 2 - Geodetic
F106,-75.4824$Launch Longitude
F107,37.8385$ Launch Latitude
F108,0.$       Launch altitude (ft) Sea Level +
F65,4$         Velocity input option 4 - wrt Earth
F120,0.$       Velocity mag
F850,5.$       Tower exit altitude (ft) tower constraint
F121,75.$      Path Angle
F122,90.$      Azimuth angle
F173,-75.4824$Latitude of Range Reference
F174,37.8385$ Longitude of Range Reference
F66,2$         Option 2 used for body orientation
F138,0.$       Bank Angle
F139,75.$      Body attitude angle (Same as tower)
F140,90.$      Body azimuth angle (Same as tower)
F175,0.$       Initial roll velocity deg/s
$
$ -------  Termination Controls ------------
$
F60,108$       Control will be altitude
F61,5.0$       Value at termination (ft)
$
$ ------- Output section -------------
$
F58,.01$       Calls to output in seconds
F59,2$         2 = Trajectory printed output and plot files
F650,0$        Printout controlled by 651,652
F651,100$      Time is controlling output calls
F652,0.01$     Time interval
F702,23$       Number of print params   --  Print quantities are:
F703,100$      Time (s)
F704,111$      Vx
F705,493$      Cm_a
F706,887$      XCp
F707,108$      h
F708,402$      Dynamic Pressure (psf)
F709,1$        Vx dot (ft/s^2 inertial)
F710,2$        Vy dot
F711,3$        Vz dot
F712,401$      Mach number
F713,450$      Total Weight (lb)
F714,601$      Thrust  (lb)
F715,428$      Drag Force (lb)
F716,417$      Drag Coef (or Cx)
F717,121$      Flt Path angle (deg)
F718,122$      Az angle (deg)
F719,107$      Latitude (deg)
F720,106$      Longitude
F721,103$      X
F722,104$      Y
F723,105$      Z
F724,120$      Velocity (fps)
```

```
F725,1412$    Roll Rates (rev/s)
$
$ ---------- Plot Calls ----------------
$
F643,0$       Plot output will be controlled by 654 & 655
F654,100$     Time is controlling quantity
F655,.01$     Output interval sec
F1420,10$     Number of output columns
$
$ ---------- Plot Output ----------
$
F1421,100$    Time
F1422,108$    Altitude  ft
F1423,120$    Velocity  ft/s
F1424,578$    Range ft
F1425,121$    Flight Path Angle  deg
F1426,141$    Angle of Attack ' deg
F1427,142$    Angle of Yaw  a deg
F1428,1412$   Roll  angular velocity rev/s
F1429,107$    Latitude (deg)
F1430,106$    Longitude (deg)
F1437,-1$     Column output in a file
$
$ -------- Integration Controls   ---------
$
F56,1$        Adams integration
F42,1$        Printout integration performance - a end of each phase
F53,0.00001$  Init delta T
F40,1.0E-7$   Minimum delta T
$
$ -------- Aerodynamic Properties  ---------
$
F68,3$         Symmetrical Vehicle - linear aero
F63,1$         Compute Aero Loads
F156,.04246$  Aero Reference Area (sq. ft.)
F157,.2325$   Aero Ref length (ft)
F158,.2325$   Ref for Reynolds no. (ft)
$
$ ---------- Fin aerodynamics -------
$
F70,0$         1 = Compute fin aerodynamics
F891,1$        1 fin set
F894,.0$       Fin Cant (deg)
F895,0.$       Fin Misalignment (X-Y)
F896,0.$       Fin Misalignment (X-Z)
F917,100.$     Fin Breakaway (s)
F914,0$        Fin initialization
F915,0.04246$ Fin ref area (ft^2)
F916,0.2325$  Fin ref length (ft)
$
$ -------- Vehicle Parameters -------
$
$ ------- ------- Mass Properties ------
$
F143,14.688$  Structure + Payload Weight (lbs) (Actual measured wt.)
```

```
$
$ -------- -------- Rocket _____
$
F55,1$          Thrusting in this phase
F597,5$         Five rockets
F614,90.0$      Thrust Misalignment (deg) with X Axis- Rocket 1
F616,90.0$      Thrust Misalignment - Rocket 2
F618,90.0$      Thrust Misalignment - Rocket 3
F620,90.0$      Thrust Misalignment - Rocket 4
F622,0.$        Thruster Five  0.0 degs. misaligned
F615,-45.$      Thrust Misalignment wrt XZ plane - Rocket 1
F617,-135.$     Thrust Misalignment wrt XZ plane - Rocket 2
F619,135.$      Thrust Misalignment wrt XZ plane - Rocket 3
F621,45.$       Thrust Misalignment wrt XZ plane - Rocket 4
F623,0.$        Thrust Misalignment wrt XZ plane - Rocket 5
F634,0.01$      Nozzle Exit Area (sq ft) - Rocket 1
F635,0.01$      Nozzle Exit Area (sq ft) - Rocket 2
F636,0.01$      Nozzle Exit Area (sq ft) - Rocket 3
F637,0.01$      Nozzle Exit Area (sq ft) - Rocket 4
F638,0.01$      Nozzle Exit Area (sq ft) - Rocket 5
F639,14.7$      Exit Pressure (psi) - Rocket 1
F640,14.7$      Exit Pressure (psi) - Rocket 2
F641,14.7$      Exit Pressure (psi) - Rocket 3
F642,14.7$      Exit Pressure (psi) - Rocket 4
F643,14.7$      Exit Pressure (psi) - Rocket 5
F830,0.$        Ignition time (s) rocket 1
F831,1.551$     Burnout time (s) rocket 1
F832,0.$        Ignition time (s) rocket 2
F833,1.551$     Burnout time (s) rocket 2
F834,0.$        Ignition time (s) rocket 3
F835,1.551$     Burnout time (s) rocket 3
F836,0.$        Ignition time (s) rocket 4
F837,1.551$     Burnout time (s) rocket 4
F838,0.$        Ignition time (s) rocket 5
F839,1.551$     Burnout time (s) rocket 5
F855,-3.3333$   X Coordinate of Thrust Application - Rocket 1 (ft)
F856,.0417$     Y Coordinate of Thrust Application - Rocket 1
F857,.0417$     Z Coordinate of Thrust Application - Rocket 1
F858,-3.333$    X Coordinate of Thrust Application - Rocket 2 (ft)
F859,-.0417$    Y Coordinate of Thrust Application - Rocket 2
F860,.0417$     Z Coordinate of Thrust Application - Rocket 2
F861,-3.333$    X Coordinate of Thrust Application - Rocket 3 (ft)
F862,-.0417$    Y Coordinate of Thrust Application - Rocket 3
F863,-.0417$    Z Coordinate of Thrust Application - Rocket 3
F864,-3.333$    X Coordinate of Thrust Application - Rocket 4 (ft)
F865,.0417$     Y Coordinate of Thrust Application - Rocket 4
F866,-.0417$    Z Coordinate of Thrust Application - Rocket 4
F867,-3.333$    X Coordinate of Thrust Application - Rocket 5 (ft)
F868,0.$        Y Coordinate of Thrust Application - Rocket 5
F869,0.$        Z Coordinate of Thrust Application - Rocket 5
$
$ ------- Environmental Parameters --------
$
F53,300000$     Max heigth for Atmosphere
F50,0$          Spherical Earth
```

```
F51,0$          Winds (1 yes - 0 no)
F54,1$          1 = rotating Earth
$
$   Table Multipliers
$
F992,57.296$               Conversion factor (/deg to /rad)
F993,-.0833$               CG and CP multiplier (in. to ft.)
F994,1.0$                  Wind Multiplier (Knots)
F995,0.002$                Thrust correction from total to each nozzle
F996,0.,998,1.,999,-1.$    General multipliers
F997,-0.67$                Clp determined from ASDEQ
$
$   Table control cards for Phase 1  (6DOF)   ------
$
F1,0,11,108,0,0,335,0,996,-1,0,0,0*           WEI + north Wind(zero)
F2,0,11,108,0,0,336,0,994,1,0,0,0*            WEJ + East wind
F3,0,14,108,0,0,337,0,996,-1,0,0,0*           WEK + Down wind (zero)
F4,0,2,108,0,0,338,0,998,-1,0,0,0*            P/P inf (zero)
F5,0,2,108,0,0,339,0,998,-1,0,0,0*            rho/rho inf (zero)
F6,0,2,108,0,0,340,0,998,-1,0,0,0*            C infC' inf (zero)
F7,0,2,108,0,0,341,0,998,-1,0,0,0*            mu inf/mu' inf (zero)
F16,0,1,401,108,0,417,0,999,1,0,0,0*          Cx
F25,0,2,401,0,0,426,0,998,1,0,0,0*            CN'
F26,0,14,401,0,0,427,0,996,-1,0,0,0*          CnP alpha
F27,0,14,401,0,0,483,0,996,-1,0,0,0*          Cl (zeroed)
F28,0,17,401,0,0,484,0,997,-1,0,0,0*          Clp set to -.667
F32,0,4,401,0,0,488,0,426,1,0,0,0*            Cmq
F37,0,12,401,0,0,493,0,992,1,0,0,0*           Cm alpha
F38,0,5,100,0,0,494,0,996,-1,0,0,0*           CmP alpha
F39,0,08,100,0,0,601,0,995,1,0,0,0*           Thrust - Rocket 1
F40,0,08,100,0,0,602,0,995,1,0,0,0*           Thrust - Rocket 2
F41,0,08,100,0,0,603,0,995,1,0,0,0*           Thrust - Rocket 3
F42,0,08,100,0,0,604,0,995,1,0,0,0*           Thrust - Rocket 4
F43,0,08,100,0,0,605,0,998,1,0,0,0*           Thrust - Rocket 5
F50,0,17,100,0,0,644,0,996,-1,0,0,0*          Lp - Jet damp coef - XB(zero)
F51,0,14,100,0,0,645,0,998,1,0,0,0*           Mq - Jet damp coef - YB
F52,0,14,100,0,0,646,0,998,1,0,0,0*           Nr - Jet damp coef - ZB
F59,0,5,100,0,0,611,0,993,1,0,0,0*            Xcg
F60,0,7,100,0,0,612,0,996,-1,0,0,0*           Ycg (zero)
F61,0,7,100,0,0,613,0,996,-1,0,0,0*           Zcg (zero)
F62,0,06,100,0,0,160,0,998,1,0,0,0*           Propellant weight
F63,0,13,100,0,0,161,0,998,1,0,0,0$           Ixx (roll)
F64,0,07,100,0,0,165,0,998,1,0,0,0*           Iyy (pitch)
F65,0,07,100,0,0,169,0,998,1,0,0,0*           Izz (yaw)
F75,0,14,100,0,0,851,0,996,-1,0,0,0*          Despin
F90,0,03,401,0,0,887,0,993,1,0,0,0*           Xcp total veh
F91,0,03,401,0,0,888,0,996,-1,0,0,0*          Ycp total veh (zero)
F92,0,03,401,0,0,889,0,996,-1,0,0,0*          Zcp total veh (zero)
F100,0,15,401,0,0,925,0,993,1,0,0,0*          Xcp fin set
F101,0,15,401,0,0,926,0,996,-1,0,0,0*         Ycp fin set (zero)
F102,0,15,401,0,0,927,0,996,-1,0,0,0*         Zcp fin set (zero)
F115,0,15,401,0,0,1001,0,996,-1,0,0,0*        CN delta (zero)
F120,0,16,401,0,0,1006,0,997,-1,0,0,0*        Cl delta
X1,1*
     Phase 2 Tube Exit to BurnOut
```

```
X0,13,0,0,0,2,2$        Phase 2 input params
*                       A-Array inputs
F64,1$                  Use inertial position IC's
F65,1$                  Vel IC  Inertial
F66,2$                  Option 2 used for body orientation
F138,0.$                Bank Angle
F139,75.$               Body attitude angle (Same as tower)
F140,90.$               Body azimuth angle (Same as tower)
F175,0.$                Initial roll velocity deg/s
F53,0.00001$            Init delta T
F60,100,61,1.551$ Phase 2 Stop at apogee
F58,.1$                 Calls to output
F652,.1$                Output reduced to every second
F655,.1$                Plot output every second
X1,1*

    Phase 3 BurnOut to Apogee
X0,10,0,0,0,2,2$  Phase 3 input params
*                       A-Array inputs
F64,1$                  Use inertial position IC's
F65,1$                  Vel IC  Inertial
F66,1$                  Direction Cosines - Body IC's
F53,0.00001$            Init delta T
F55,0$                  No Thrust
F60,121,61,0.0$         Phase 3 Stop at apogee
F160,0.0$               zero propellant wgt
F652,.5$                Output reduced to every second
F655,.5$                Plot output every second
X1,1*
    Phase 4  Apogee to Impact
X0,2,0,0,0,3,2*    Phase 4
F60,108,61,0.0*    End Altitude
/*
```

6. FIELD-MEASUREMENT THEORY AND CALIBRATION

6.1   Theory of Measurement

The theory of measuring ambient electrostatic field from an aircraft with multiple field mills is well developed and has been discussed recently by Laroche,[27] Bailey and Anderson,[26] and Kositsky et al.[24] Here we outline the basic ideas in the context of our rocket design.

Imagine a right-handed, Cartesian coordinate system aligned so that the z-axis lies along the longitudinal (symmetry) axis of the rocket, pointing in the direction of flight (see Figure 4). The x- and y-axes are then similar and transverse to the rocket axis. Consider first a homogeneous (over dimensions large compared to those of the rocket), steady (over times comparable to one shell-rotation period) electric field component E_z directed in the positive z direction. When the rocket is placed in this ambient field, it distorts the field locally in a manner described by Laplace's equation (with boundary conditions specifying a uniform field at infinity and zero potential over the surface of the rocket). Since Laplace's equation is linear, its solution for the surface field contribution F'_i at any set of points on the rocket body (the locations of the field mills) due to component E_z can be expressed as follows:

$$F'_1 = a_{1z}E_z$$

$$F'_2 = a_{2z}E_z$$

$$\cdots$$

$$F'_8 = a_{8z}E_z$$

(1)

Next, suppose that a homogeneous, electrostatic field component E_x is directed in the positive x direction. Again, Laplace's equation gives the field contribution at the same set of points on the rocket body, the only difference in the boundary conditions being the direction of the uniform field at infinity. This yields another set of coefficients a_{ix}. Similarly, a solution can be obtained for an electric field component E_y in the positive y direction. Finally, Laplace's equation can be solved for zero ambient field and potential at infinity but a uniform potential V on the rocket, giving the coefficients a_{iv}. (It should be noted that these potential coefficients have different units from the field coefficients.) By the superposition principle, these four solutions can be added to obtain the total field F_i at each mill due to an arbitrary ambient vector field $\mathbf{E}$ (or to an arbitrary orientation of the rocket) and an arbitrary net charge ($Q = CV$, where C is the capacitance) on the rocket:

72

$$F_1 = a_{1x}E_x + a_{1y}E_y + a_{1z}E_z + a_{1v}V$$

$$F_2 = a_{2x}E_x + a_{2y}E_y + a_{2z}E_z + a_{2v}V$$

(2)

$$\ldots$$

$$F_8 = a_{8x}E_x + a_{8y}E_y + a_{8z}E_z + a_{8v}V$$

Obviously, Eq. (2) can be expressed in matrix notation. Extending the definition of the vector **E** to include the potential V as its fourth component, we have

$$\mathbf{F} = \mathbf{AE}$$

(3)

where **A** is an 8x4 matrix of constants (for a particular rocket geometry). Assuming the symmetry of the rocket described in Section 4.2, we can write this equation as follows:

$$
\begin{pmatrix} F_{tr} \\ F_{tl} \\ F_{mr} \\ F_{ml} \\ F_{br} \\ F_{bl} \\ F_{mt} \\ F_{mb} \end{pmatrix}
=
\begin{pmatrix}
0 & a_{ty} & a_{tz} & a_{tv} \\
0 & -a_{ty} & a_{tz} & a_{tv} \\
0 & a_{my} & a_{mz} & a_{mv} \\
0 & -a_{my} & a_{mz} & a_{mv} \\
0 & a_{by} & a_{bz} & a_{bv} \\
0 & -a_{by} & a_{bz} & a_{bv} \\
a_{my} & 0 & a_{mz} & a_{mv} \\
-a_{my} & 0 & a_{mz} & a_{mv}
\end{pmatrix}
\cdot
\begin{pmatrix} E_x \\ E_y \\ E_z \\ V \end{pmatrix}
$$

(4)

The first subscripts t, m, and b refer to the top, middle, and bottom longitudinal positions along the payload, while the second subscripts r,l,t, and b refer to the right, left, top, and bottom azimuthal positions around its circumference, looking up the tail of the rocket (along the positive z axis). By symmetry, the right and left azimuthal positions see no E_x and

the top and bottom azimuthal positions see no E_y. Furthermore, there are only nine independent, non-zero coefficients: a_{ty}, a_{tz}, a_{tv}, a_{my}, a_{mz}, a_{mv}, a_{by}, a_{bz}, and a_{bv}. In addition, the cylindrical shape of the vehicle guarantees that the approximation

$$a_{ty} = a_{my} = a_{by} = 2 \tag{5}$$

is reasonably accurate, leaving only six independent, unknown coefficients.

Methods of inverting the matrix equation (3) to obtain a good estimate of the ambient field **E** from the measured fields **F** have been discussed by Laroche[27] and Kositsky et al.[24] and will not be repeated here.

In practice, the measured fields must be determined from waveforms representing the charge on each stator as a function of time, telemetered to the ground as described in Section 3. Since the stator electrodes are wider than the holes in the rotating cover, as described in Sections 2.2 and 4, these waveforms approximate a truncated triangle wave (see Figure 34). The data-analysis software was constructed to average successive flat segments on the top and bottom of such a periodic waveform, guided by a knowledge of the shell position deduced from the optical detectors, and to take the difference of these averages for each period. This difference, reported in "digital units" (DU -- one digital unit corresponds to 1.46×10^{-3}V at the input of the A/D converter) is proportional to the change in stator charge caused by uncovering the stator and, hence, to the field at the mill. It is referred to henceforth as the "synchronously rectified" mill signal.

6.2. Laboratory Calibration

Three different calibrations were attempted in the laboratory: (1) The potential coefficients a_{iv} were determined by suspending the entire vehicle (payload and rocket motor) with an insulating line from the ceiling of a large room, nose upward, and connecting the tail to a high-voltage power supply. (2) The longitudinal field coefficients a_{iz} were estimated by mounting the payload protruding through the grounded wall of a test chamber, applying an AC field, and measuring the AC charge induced on each stator electrode. (3) We tried to measure the transverse-field coefficients a_{ty} by hanging the payload in the middle of the same test chamber, but problems associated with electrically floating the payload and measuring instrumentation at a high AC voltage prevented this calibration from being successful. This measurement will have to be made at a future date. It is recognized that none of these laboratory calibrations is ideal, and the final calibration must be performed in flight, as described in Section 2.
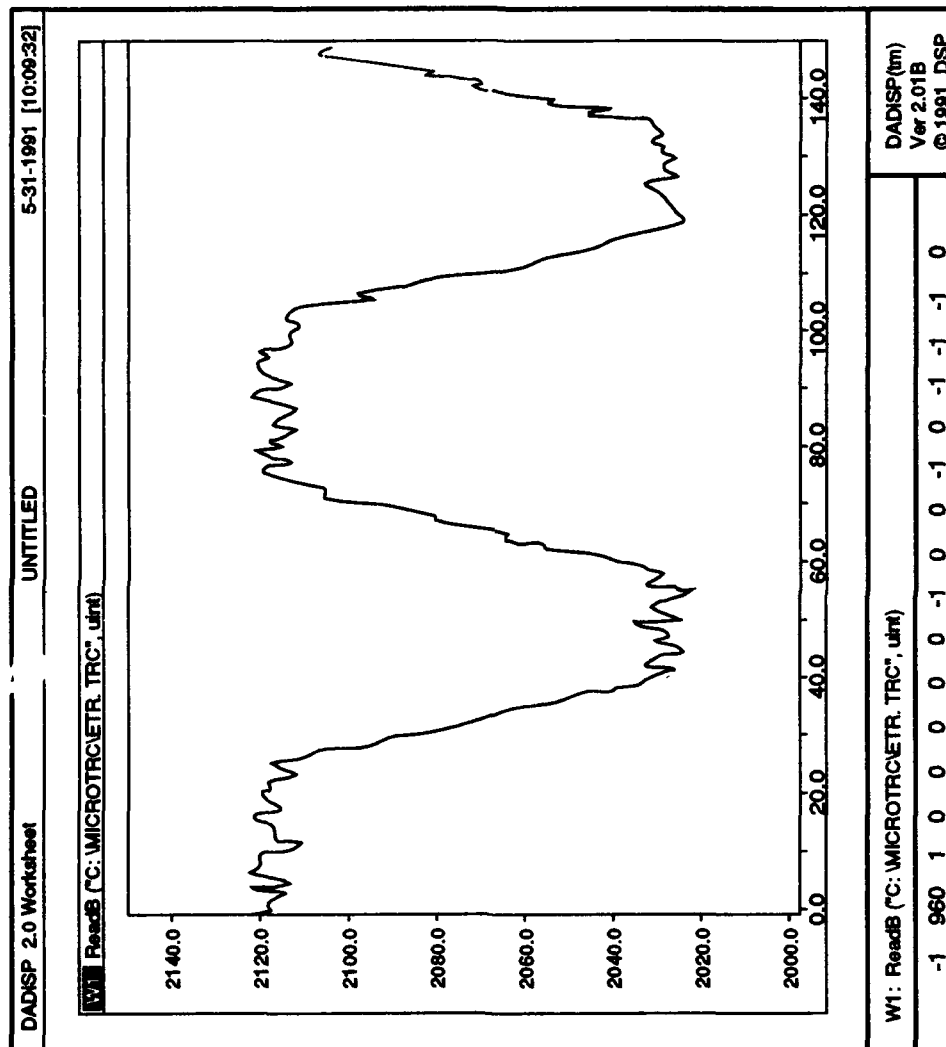
Figure 34. The Output of the Top-right Mill When +10 kv is Applied to the Payload. The vertical axis shows the signal level in digital units. The horizontal axis shows relative sample number. At 2315 samples/s, the figure shows about 6.5 ms.

6.2.1 POTENTIAL CALIBRATION

There were three steps involved in the potential calibration of the payload. First, the rocket was suspended in a large field-free region and raised to a known potential. Voltage was applied to the tail of the rocket by a wire lying along the negative z axis. Since this configuration placed the wire far from all the mills, it is believed that no significant perturbations were introduced. The telemetry was operating during calibration, so that the field signals passed through all the electronics, yielding an end-to-end calibration. Figure 34 shows a sample field-mill waveform obtained in this test. The second, third, and fourth columns of Table 7 give the synchronously rectified signals (in DU) from each of the mills for three different values of applied potential. No time variations were observed that might indicate perturbations due to space charge accumulation around the rocket.

Table 7. Field-Mill Outputs vs. Applied Potential and Stator Charge

Field	Applied Potential			Sensitivity	a_{iv}
Mill	+10 kV	–10 kV	0 kV	(pC/DU)	(m^{-1})
TR	–89.53	89.23	0.17	–11.86	4.37
TL	–89.92	90.11	0.32	–11.81	4.38
MR	–83.82	83.28	0.16	–11.88	4.10
ML	–83.91	84.54	0.18	–11.75	4.08
BR	–84.21	83.96	0.28	–11.74	4.07
BL	–82.91	83.86	0.22	–11.86	4.08
MT	–85.86	86.17	–0.63	–11.82	4.19
MB	–86.06	85.66	–0.45	–11.62	4.12

The second step in this calibration was to measure the sensitivity of each channel of the mill electronics by applying a known charge to the corresponding stator. This was done with a square-wave generator whose voltage output was measured to better than 1 percent and a capacitor calibrated to similar accuracy. The circuit shown in Figure 35 limits the rate of rise of the square wave to a level manageable by the mill charge amplifiers. The results of these measurements are given in the fifth column of Table 7 in pC/DU. It is to be noted that these values are consistent to ± 1.5 percent and agree well with the nominal value of -11.5 pC/DU defined by the electronics described in Section 3.

The third step was to determine the effective surface area of the field mills. This was to be an additional benefit of the measurement of the transverse-field coefficients listed above as laboratory-calibration 3. Since that exercise was not successful, we use the geometrical area A of the holes in the rotating shell. From the drawings in Section 4, A = 2.74 x 10^{-3} m^2. This value is an over estimate, due to fringing, but cannot be off by more than several percent
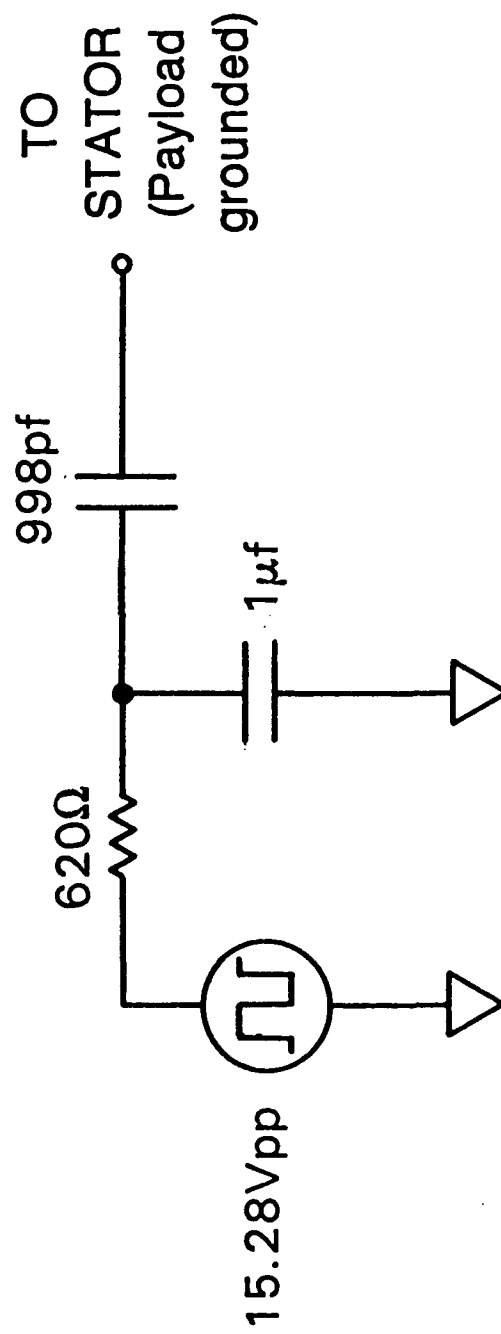
Figure 35. Stator Calibration Circuit. The low-pass filter is needed to reduce the rise time of the square-wave generator.

because the rotor-to-stator spacing is only a small fraction of the other dimensions of the hole. Since the surface field is related to the stator charge by

$$F = Q/\varepsilon_0 A \tag{6}$$

where $\varepsilon_0 = 8.85 \times 10^{-12}$ is the dielectric permittivity of air, the voltage coefficients of the various mills can be tabulated in the last column of Table 7 in units of m^{-1}. The values for different mills at the same longitudinal position are quite consistent, as they should be, except perhaps for mill MT, which seems about 2 percent high. Note that the absolute values of these coefficients are not important because the voltage on the rocket is not a very useful number. Their relative values are unaffected by our over estimate of A, and they can be checked in flight by virtue of the on-board charging system.

6.2.2 LONGITUDINAL FIELD CALIBRATION

The only large electric-field-calibration chamber readily available to us was located at the Naval Research Laboratory (NRL) in Washington, DC. The chamber is an 11 ft cube of which one wall is grounded, an arbitrary potential can be applied to the opposite wall, and the other four sides consist of overlapping guard rings. These rings are connected to successive steps of a resistor ladder between the grounded and active walls to reduce fringing effects by forcing a uniform field along the sides. The entire assembly is shielded from external fields by a grounded Faraday cage. The use of this chamber has been described by Gathman[30] He kindly made it available to us.

Because the NRL chamber was too small to encompass the whole REFS vehicle without introducing significant errors due to image effects in the walls, it was decided to approximate free-field conditions by mounting the payload so that it protruded half a rocket length through the grounded wall. It is well known that an uncharged conductor immersed in a uniform field perpendicular to a plane of symmetry can be correctly represented by replacing one half-space with a grounded plane located in the symmetry plane. Although the rocket is not perfectly symmetrical about any plane perpendicular to its longitudinal axis, the difference between nose cone and tail fins can be neglected to a good approximation, since they are far apart compared to the difference in their dimensions. Thus, there will be a zero-potential surface that is nearly planar and cuts the vehicle near the center of its longitudinal axis. The overall length of the REFS vehicle is about 82 in. from nose tip to fin tip (with the fins deployed in flight configuration), so measurements were made with the payload protruding 39-1/2, 41, and 42-1/2 in. from the chamber wall.

Space charge will accumulate in such a calibration chamber when a DC field is applied -- a result of the "electrode effect". In the worst case, this can lead to a decrease of about a factor of

---

[30] Gathman, S.G. (1968) Guarded double field meter, *Rev. Sci. Instrm.* **39**:43-47.

2 in the field intensity at the center of the chamber relative to that at the walls. In order to eliminate any errors due to the electrode effect, we performed our calibration in an AC field. This was accomplished by stopping the rotating shell, so as to center its holes precisely over the stator plates, and measuring the AC charge induced on the stators by the applied field. To verify that subtraction of the charge induced with the stators fully covered by the rotor, as performed in normal operation of the payload, was unnecessary, measurements were made in the covered position also. In every case, the charge induced on a covered stator was more than two orders of magnitude less than that on the same stator uncovered.

The data were taken with 1045 VRMS at 419 Hz across the chamber, producing a peak ambient field of about 441 V/m. To record the alternating charge induced on the stators by this alternating field, the normal electronics were removed from the payload. Each stator in turn was connected by shielded cable to a charge amplifier followed by a bandpass filter and peak detector (see Figure 36). All eight shielded cables were led down the interior of the payload and out the rear, behind the grounded wall of the chamber. While one stator was being measured, all the others were grounded.

The measuring circuit delivered a voltage V_i proportional to the peak charge on each of the stators. The peak charge induced on a circular plate of area $A_{flush} = 3.90 \times 10^{-3}$ m^2, flush-mounted in the grounded wall was also measured, with the payload removed. Any scale factors that might have been introduced by peculiarities of the measuring circuit or its response to the roughly sinusoidal, chamber-voltage waveform were canceled by recording ratios of stator to flush-mounted charge density, again assuming the stator effective area A given above:

$$a_{iz} = F'_i/E_z = (V_i/A)/(V_{flush}/A_{flush}) \tag{7}$$

The resulting values of the longitudinal field coefficients are given in Table 8 for the three different mounting positions of the payload. Again, the values for different mills at the same longitudinal position are quite consistent. The different values for longitudinal offsets of ± 1.8 percent (relative to the overall rocket length) around the geometric center give some idea of the uncertainty of these coefficients due to the measurement technique. Compared with these differences, which range from ± 5 percent at the top mills to ± 12 percent at the bottom, the absolute under-estimate of a_{iz} due to our incorrect value of A is probably insignificant. Obviously, a better calibration is needed here.
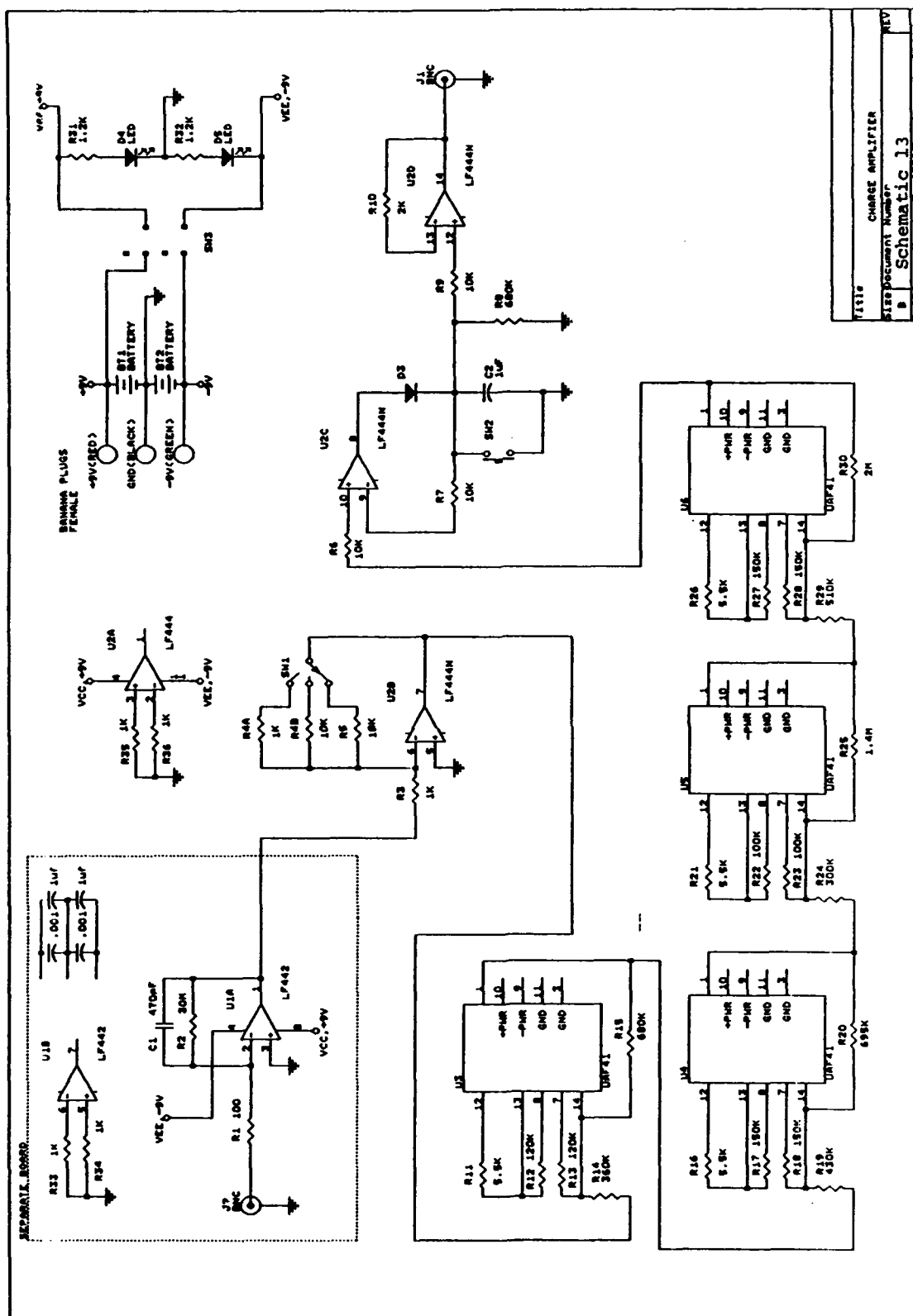
Figure 36. Charge Amplifier Circuit Diagram

Table 8. Estimates of Longitudinal Field Coefficients a_{iz}

Field Mill	Payload Protrusion		
	42.5 in.	41 in.	39.5 in.
TR	3.97	3.78	3.61
TL	4.07	3.90	3.72
MR	2.51	2.35	2.18
ML	2.58	2.42	2.25
BR	1.56	1.40	1.23
BL	1.57	1.42	1.25
MT	2.47	--	--
MB	2.59	--	--

6.3. Theoretical Calibration

Theoretical estimates of the calibration coefficients can be made in various ways. An estimate of the transverse-field coefficients has already been presented in Eq. (5), based on the reasonable assumption that the payload approximates an infinite circular cylinder. This can be checked in flight, since the transverse field is measured independently at three different longitudinal positions.

The REFS vehicle can also be crudely approximated by a prolate conducting spheroid, a boundary condition for which Laplace's equation has been solved analytically. Moore[31] has given expressions for the electrostatic field around such a body, uncharged and immersed in a uniform ambient field parallel to its axis of symmetry. Using the notation of Smythe[32] (Chapter 5), we can write the surface field intensity on the spheroid as

$$E_s = \frac{E_z}{\eta_o \left(\eta_o^2 - 1\right)^{1/2} \left[\frac{1}{2} \ln\left(\frac{\eta_o + 1}{\eta_o - 1}\right) - \frac{1}{\eta_o}\right]} \frac{\frac{z}{c}}{\left(\eta_o^2 - \frac{z^2}{c^2}\right)^{1/2}} \tag{8}$$

$$\eta_o = \left(1 - \frac{b^2}{c^2}\right)^{-1/2} \tag{9}$$

[31] Moore, C.B. (1983) Improved configurations of lightning rods and air terminals, *J. Franklin Inst.*, **315**:61-65.

[32] Smythe, W.R. (1968) *Static and Dynamic Electricity*, Third Edition, McGraw-Hill Book Company, New York.

where b is the semi-major-axis length (half the rocket length), c is the semi-minor-axis length (half the diameter), η_0 refers to the surface of the spheroid, and z is the height above its center, measured along the semi-major axis. Stratton,[33] has given expressions for the charge-density distribution and potential on such a body if it is charged but in a field-free region. Converting surface-charge density to surface field and using the notation of Smythe,[32] (Chapter 5), we have

$$E_s = \frac{Q}{4\pi\varepsilon_0 cb}\left(1 - \frac{z^2}{c^2\eta_0^2}\right)^{-1/2} \tag{10}$$

$$V = \frac{Q}{4\pi\varepsilon_0 c}\frac{\eta_0}{2}\ln\left(\frac{\eta_0+1}{\eta_0-1}\right). \tag{11}$$

Thus, the capacitance and voltage coefficient of the spheroid become

$$C = 4\pi\varepsilon_0 c\frac{2}{\eta_0\ln\left(\frac{\eta_0+1}{\eta_0-1}\right)} \tag{12}$$

$$\frac{E_s}{V} = \frac{2}{b\eta_0\ln\left(\frac{\eta_0+1}{\eta_0-1}\right)}\left(1 - \frac{z^2}{c^2\eta_0^2}\right)^{-1/2}. \tag{13}$$

Heckman and Williams[34] [Eq. (2)] have derived an approximate expression for the linear charge density on a long, thin, cylindrically symmetric conductor in an ambient field parallel to its symmetry axis. They place no other restrictions on the diameter of their conductor, except that it must vary slowly with z. Although our rocket is probably not thin enough to satisfy their approximations, its diameter is constant over nearly its entire length, making the spheroid a poor match for computing the surface field far from its center. Therefore, we convert the Heckman and Williams expression to give the surface field on our rocket as follows:

[33] Stratton, J.A. (1941) *Electromagnetic Theory*, McGraw-Hill Book Company, New York.
[34] Heckman, S.J., and Williams, E.R. (1989) Corona envelopes and lightning currents. *J. Geophys. Res.*, **94**:13, 287-13, 294.

$$E_s \sim \frac{E_z}{R\ln(L/R)} \, z \qquad\qquad (14)$$

where $2L$ is the longitudinal length and $2R$ is the diameter.

We chose two different spheroids in an attempt to match the REFS vehicle. Both have $c = 1.05$ m. Spheroid 1 has $b = 0.035$ m to match the rocket diameter, giving $\eta_0 = 1.000549$ and a radius-of-curvature at the tip of only 1.2 mm. For Spheroid 2, $b = 0.071$ m was chosen to match the actual 4.75 mm radius-of-curvature of the nose, giving $\eta_0 = 1.00226$. (Note that the maximum possible nose radius-of-curvature of 2.75 in./2 implies $b = 7.5$ in., which is nearly 5-1/2 times as fat as the actual rocket.) For the Heckman and Williams formula, we chose $L = 1.05$ m and $R = 0.035$ m.

Table 9 gives the theoretical potential and longitudinal-field coefficients for the two spheroids at the three longitudinal positions where field mills are located on REFS. Also given are the field-enhancement factor and potential coefficient at the tip and the total capacitance of the spheroids, as well as the longitudinal-field coefficients from the Heckman and Williams formula.

Table 9. Analytic and Measured Field and Potential Coefficients

Longitudinal Position	Spheroid 1 a_{iz}	Spheroid 1 $a_{iz}(m^{-1})$	Spheroid 2 a_{iz}	Spheroid 2 $a_{iz}(m^{-1})$	H&W a_{iz}	Measured a_{iz}	Measured $a_{iz}(m^{-1})$
Tip	293.	211.	92.	61.9	--	--	--
T (z=0.75m)	9.89	9.96	6.28	5.92	6.32	3.84	4.38
M (z=0.52m)	5.48	8.01	3.48	4.77	4.35	2.39	4.12
B (z=0.32m)	3.11	7.33	1.98	4.36	2.70	1.41	4.08
C (pf)	28.6		34.5			--	

In the last two columns of this table we list the average of the coefficients measured at each longitudinal position, derived from Tables 7 and 8, for comparison.

It is evident from Table 9 that both the longitudinal-field and the potential coefficients for spheroids are very dependent on height above the center and that these coefficients increase (in proportion at different heights) as b/c becomes small. This is primarily because the diameter of the horizontal cross section decreases with increasing height as well as with decreasing axis ratio. In fact, it turns out that the linear charge density along the major axis of a spheroid in a uniform axial field varies only slowly with axis ratio and increases almost linearly with z, as predicted by the Heckman and Williams formula. For a charged spheroid, the linear charge density is almost constant with height, as suggested by our potential coefficients. Thus, the poor match of surface fields on a spheroid to those on REFS appears to result from the strong taper of the spheroidal shape.

6.4 Summary of Matrix Coefficients

In summary, our current best estimates of the matrix coefficients in Eq. 4 are:

$$A = \begin{pmatrix} 0.00 & 2.0 & 3.8 & 4.38 \\ 0.00 & -2.0 & 3.8 & 4.38 \\ 0.00 & 2.0 & 2.4 & 4.12 \\ 0.00 & -2.0 & 2.4 & 4.12 \\ 0.00 & 2.0 & 1.4 & 4.08 \\ 0.00 & -2.0 & 1.4 & 4.08 \\ 2.0 & 0.00 & 2.4 & 4.12 \\ -2.0 & 0.00 & 2.4 & 4.12 \end{pmatrix} \qquad (15)$$

Refinement of these numbers will have to await actual flight data in high fields.

7. TEST FLIGHT

7.1 Post-Flight Aerodynamic Analysis

The REFS rocket was launched from Wallops Flight Facility, Virginia, on 5 November, 1990, at 2036 UT. The launcher azimuth and elevation angles were 130 and 75 degrees, respectively. The flight lasted 61 seconds. WFF used multiple radars to track the REFS payload. Because of the small size and high acceleration of the vehicle, however, the first radar was not able to lock on until 8 seconds into the flight. This part of the report will discuss how the predicted performance compared to the actual performance, as determined from the radar data.

After the launch, a new model run was made based on the actual flight conditions, (that is, observed profile of wind speed and direction, launcher elevation and azimuth, launcher latitude and longitude, and air temperature). The actual and predicted apogee and range are compared below:

	Actual	Predicted	Percent Error
Apogee (ft)	12936	14981	15.8
Range (ft)	13833	14286	3.3

Recall that the no-wind prediction in Section 5.3 was for an apogee of 15,552 ft and range of 12,505 ft -- higher and shorter than either the actual or the present prediction. At launch time, the wind was blowing at 16 ft/s from 162 degrees at the surface and was increasing and turning toward the South with height. Because of the large static margin of the REFS rocket, this head wind caused the rocket to "weather cock" into the wind, thereby reducing its effective elevation angle and causing it to fly lower and longer than predicted. Evidently, the computer model accounted fairly well for this wind effect.

The next four figures compare the actual and predicted (including wind effects) trajectories for this flight. The observed (actual) curves in each figure can be recognized by the fact that the first approximately 8 seconds of the trajectory are missing from the radar data. Figure 37 shows the predicted and actual altitudes vs elapsed time. Throughout the flight the rocket was lower than predicted, and the flight duration was shorter than predicted. Figures 38 and 39 show that, at any given time, the predicted range and velocity were very close to their actual values. Thus, the thrust/drag functions used in our computer model agree well with the actual rocket. Figure 40 presents the comparison in the form of altitude versus range.

7.2   Payload Mechanical Performance

The accelerometer was intended to be used for a number of measurements, including acceleration and deceleration profiles and rocket-motor ignition and burn-out times. Using these data, it would be possible to calculate parameters such as maximum velocity and drag coefficient. Some of these measurements could not be performed, however, due to the saturation and calibration problems described in Section 3.3 above. Nevertheless, the accelerometer did provide an accurate indication of time of launch, which will be critical during the program's operational phase, and the duration of motor burn (1.5 seconds).

The magnetic field sensor operated as planned. As mentioned before, the rocket motor utilizes scarfed nozzles to apply spin during the burn phase of the flight. The data obtained showed no unexpected results. A maximum spin rate of 17 RPS occurred at motor burn out (see Figure 41). Rapid rotational deceleration was noted after motor burnout until the vehicle reached a steady spin rate of about 1 RPS throughout the remainder of the flight (see Figure 42).
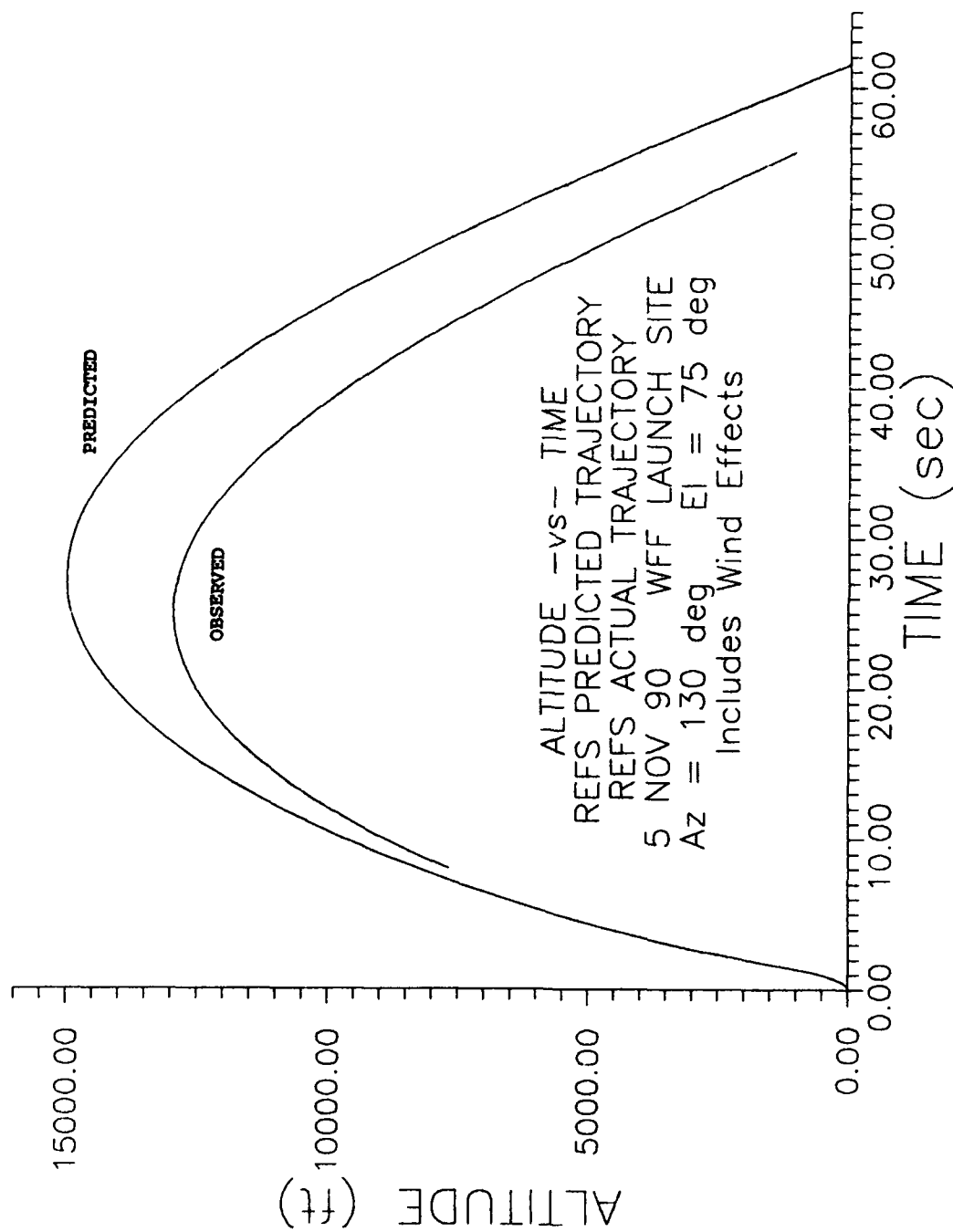
Figure 37. Altitude vs Time Predicted and Observed (Observed Trajectory Begins About 8 Seconds After Launch Because of Delays in Radar Acquisition) for the REFS Flight on on 5 Nov 91 From WFF
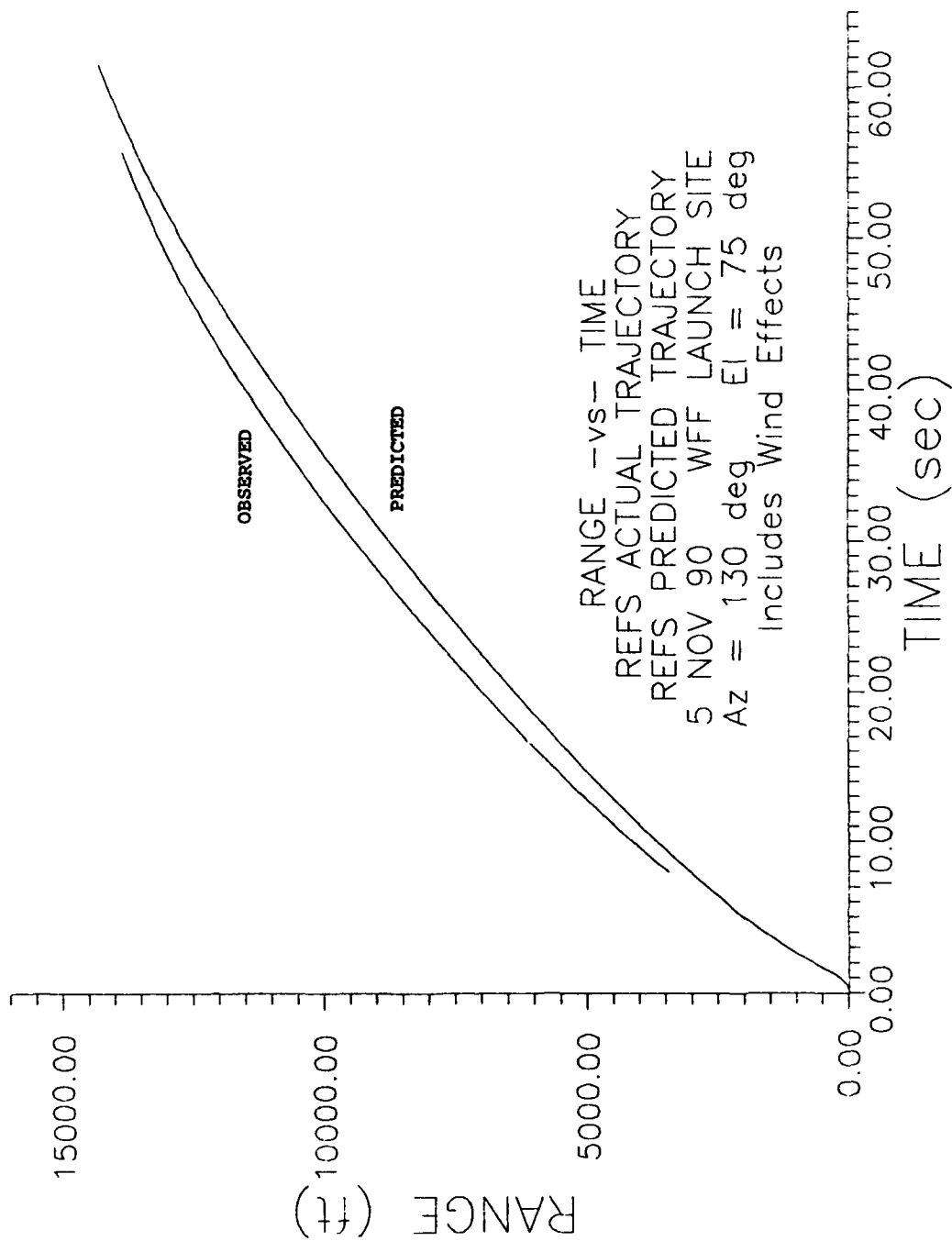
Figure 38. Range vs Time Predicted and Observed (Observed Trajectory Begins About 8 Seconds After Launch Because of Delays in Radar Acquisition) for the REFS Flight on 5 Nov 91 From WFF
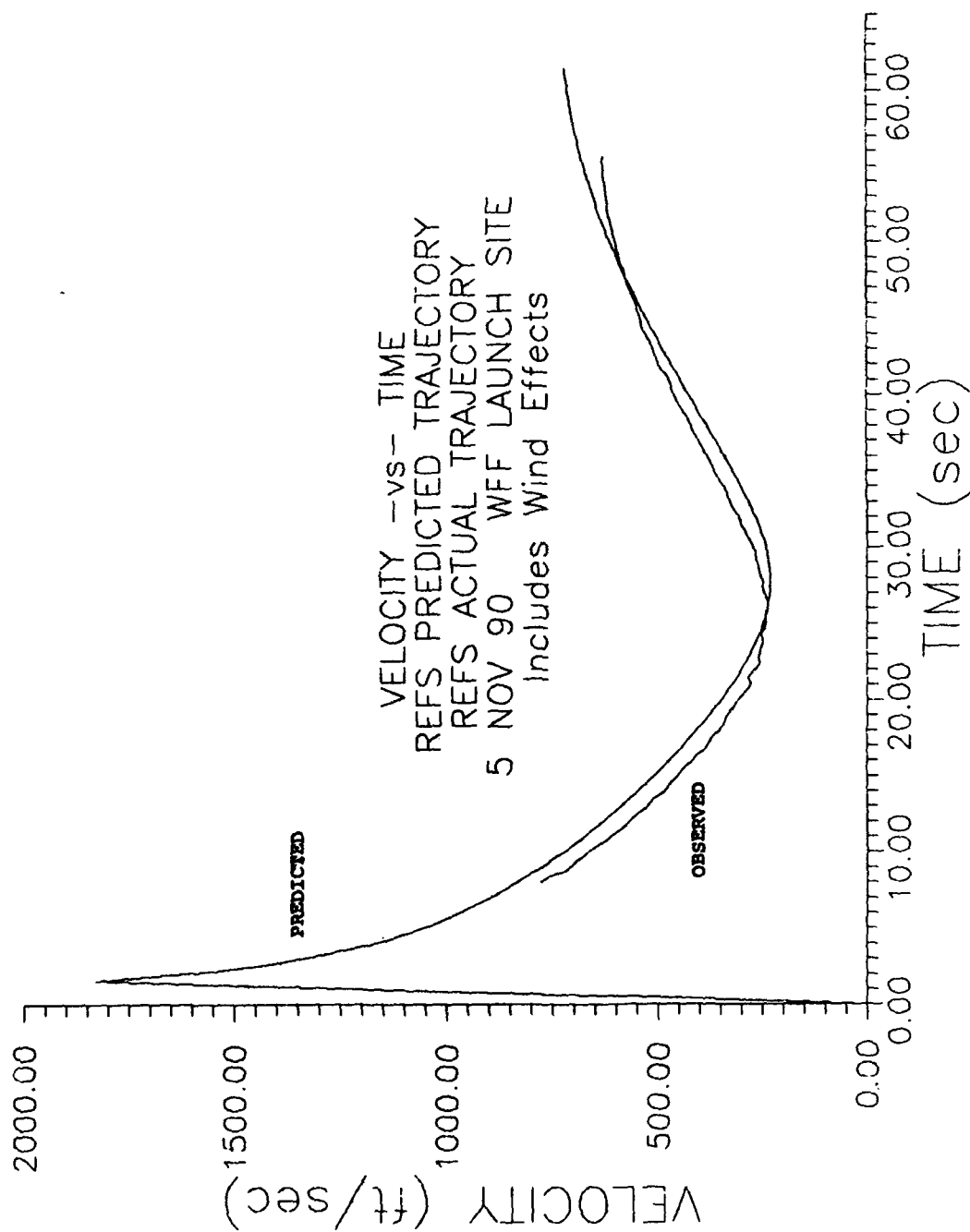
Figure 39. Velocity vs Time Predicted and Observed (Observed Trajectory Begins About 8 Seconds After Launch Because of Delays in Radar Acquisition) for the REFS Flight on 5 Nov 91 From WFF
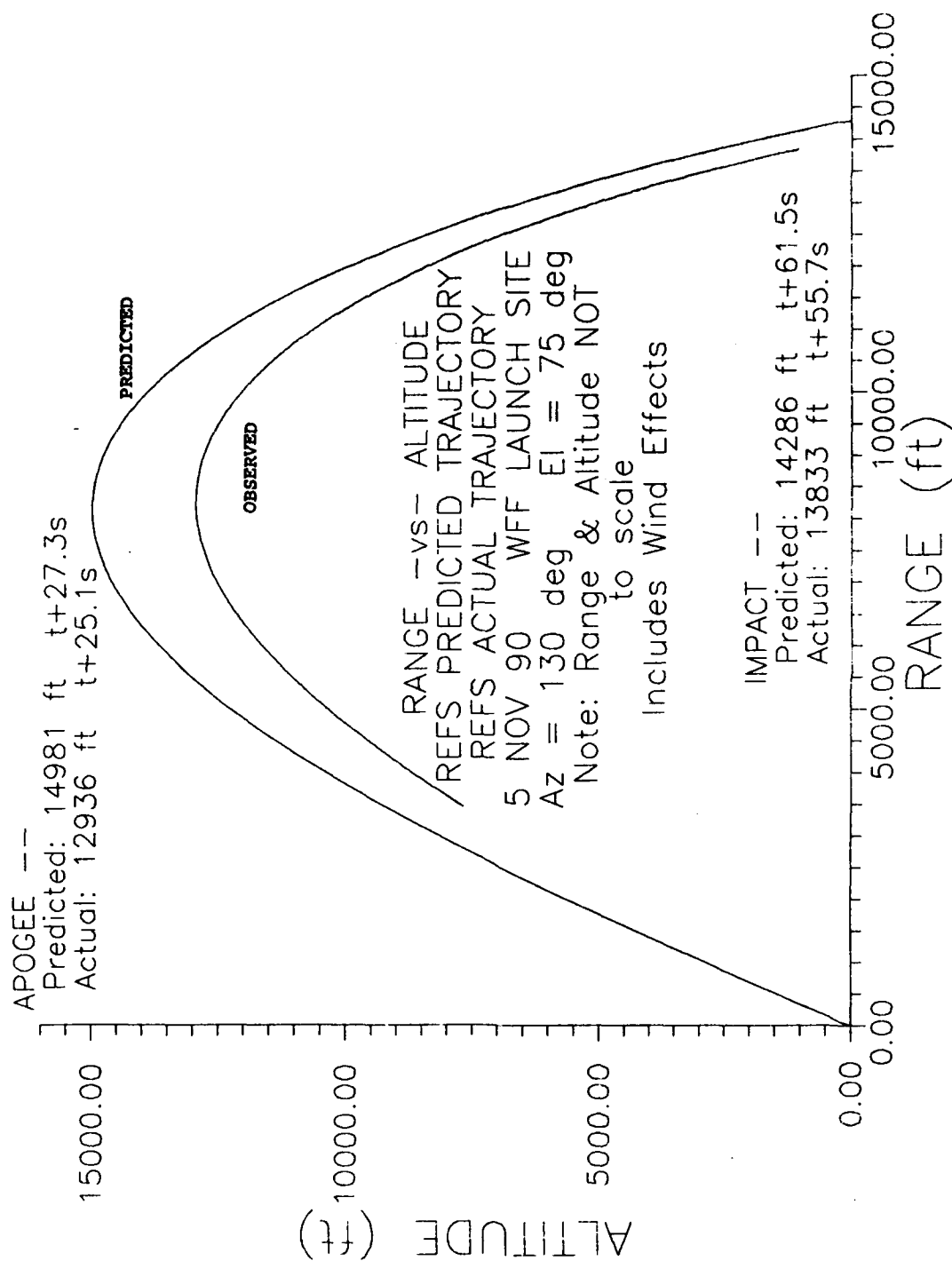
Figure 40. Altitude vs Range Predicted and Observed (Observed Trajector Begins at About 7700 ft Altitude Because of Delays in Radar Acquisition for the REFS Flight on 5 Nov 91 From WFF

VEHICLE ROTATION RATE
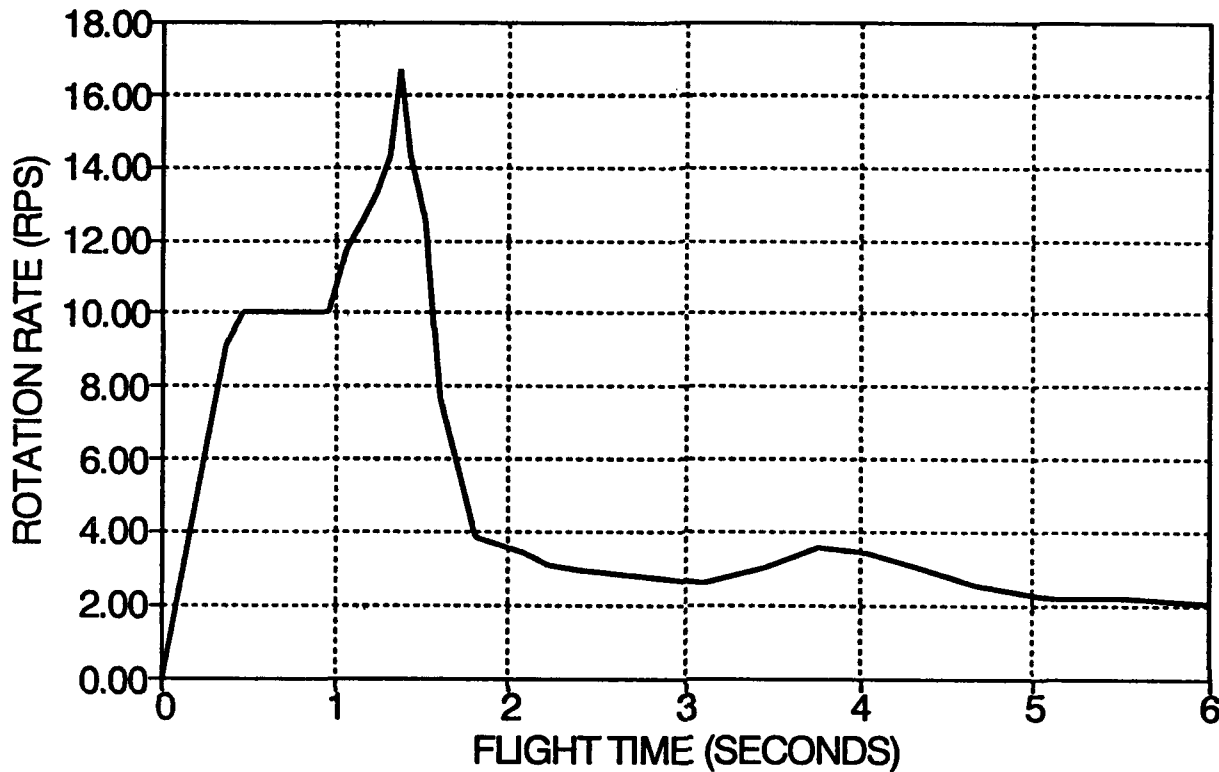## FIRST 6 SECONDS OF FLIGHT

Figure 41. Vehicle Spin Rate Around its Longitudinal Axis (Determined From the Magnetic Field Sensor) as a Function of Time During the First Six Seconds of the REFS Flight on 5 Nov 91 From WFF

The pressure transducer is located on the electronics boards and measures ambient pressure *inside* of the payload only. Calculations showed that the holes for the optical detectors alone were sufficient to vent the internal volume during both the ascent and the descent phases of the flight. Figure 43 compares the altitude vs flight time given by the pressure transducer with that from the radar data. There is good agreement. The primary anomaly is the bump centered approximately 5 s. into the flight. Analysis of trajectory predictions indicates this is the time of supersonic to sub-sonic velocity transition. It would appear that, during the super-sonic portion of flight, the pressure data are unreliable. The pressure data for the sub-sonic regime (from about 8 s. on) appear to be accurate.
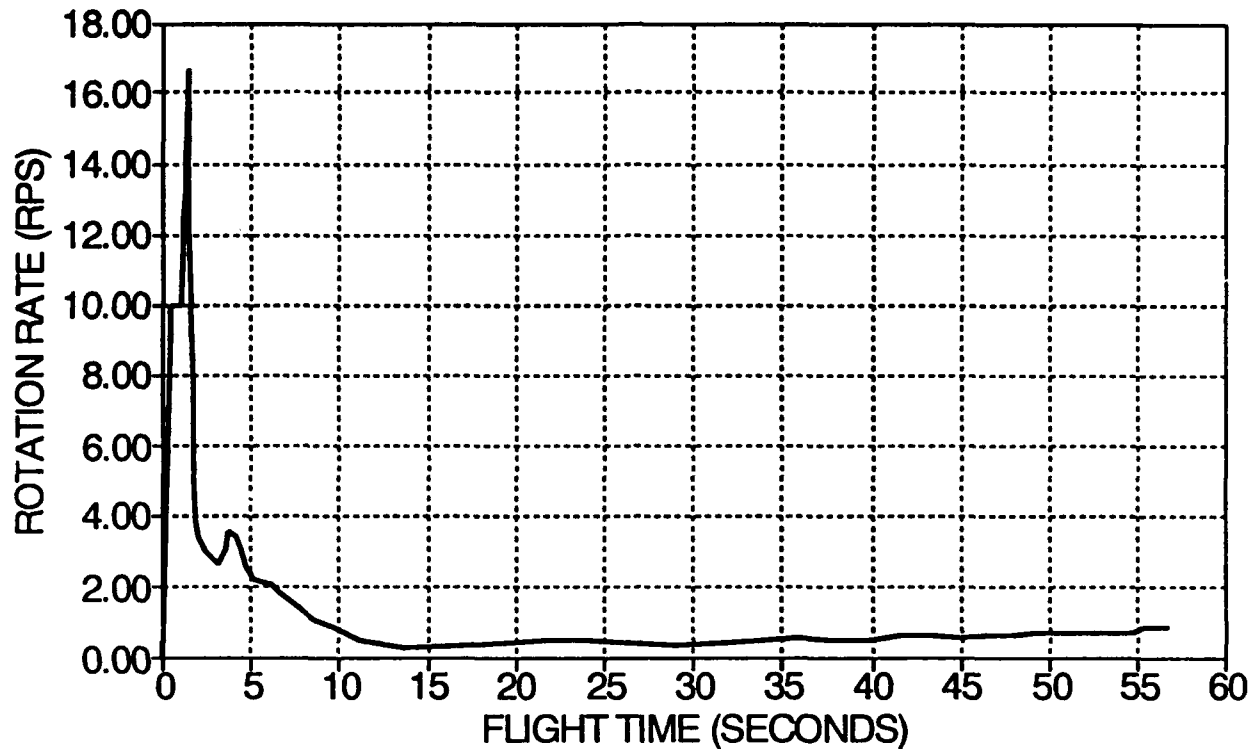
VEHICLE ROTATION RATE
ENTIRE FLIGHT

Figure 42. Vehicle Spin Rate Around its Longitudinal Axis (Determined From the Magnetic Field Sensor) as a Function of Time During the Entire REFS Flight on 5 Nov 91 From WFF

The rotor (outer shell) spin rate, obtained from the optical detectors, is compared with the vehicle spin rate in Figures 44 and 45. The rotor is spinning about 17 RPS at launch. During the burn phase of flight, the rocket motor imparts a spin to the vehicle. The direction of the vehicle rotation is the same as that of the rotor. It was therefore expected that the rotor would slow down during this phase of flight. Figure 44 shows this occurring. The outer shell regains most of its rotational rate quickly after motor burn out.

The outer shell then begins a gradual slowdown throughout the middle part of the flight (see Figure 45). This phenomenon was not expected and has yet to be explained. Several possibilities have been suggested. One is that ice or cooling might have affected the bearings. The vehicle is known to have flown through a cloud about the time that the slowdown began, and this could have supplied the moisture for ice formation. Another possibility is that the payload might have experienced high angles of attack at the lower velocities near apogee. This

91

might have caused high drag on the windows of the rotating shell or bending of the payload. In any case, the shell regains its rotation rate approximately 15 seconds before impact. It is at this point that radar boresight video shows the vehicle appearing out of the bottom of the cloud. The flight looks stable (low angle of attack) from there to impact.

Excellent photographic coverage of the entire flight was planned by WFF. Unfortunately, launch delays due to boats in the impact area resulted in unexpected cloud cover at launch time. Therefore, the tracking cameras were never able to acquire the vehicle, and much of the high speed film of the launch itself was badly under-exposed. Two 70 mm fixed cameras, one operating at 20 frames/s and the other at 30 frames/s, obtained good images of the initial 20 to 30 m of the flight. These photos show smooth and straight exit of the vehicle from the launch tube and proper deployment of the folding fins. They also allow calculation of an approximately constant acceleration of 34g during this part of the flight.
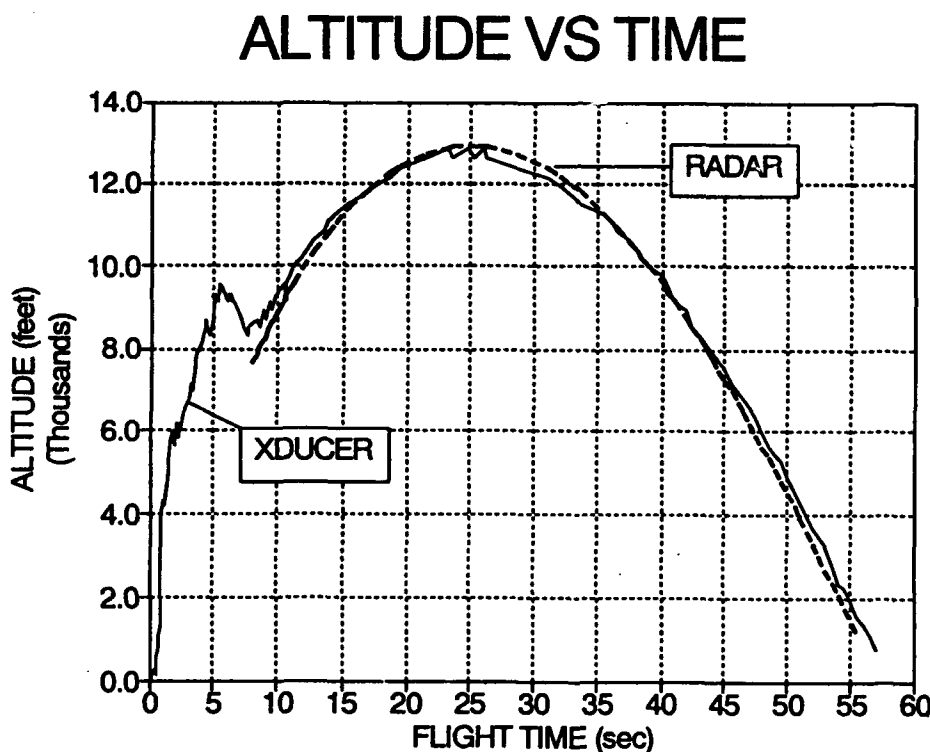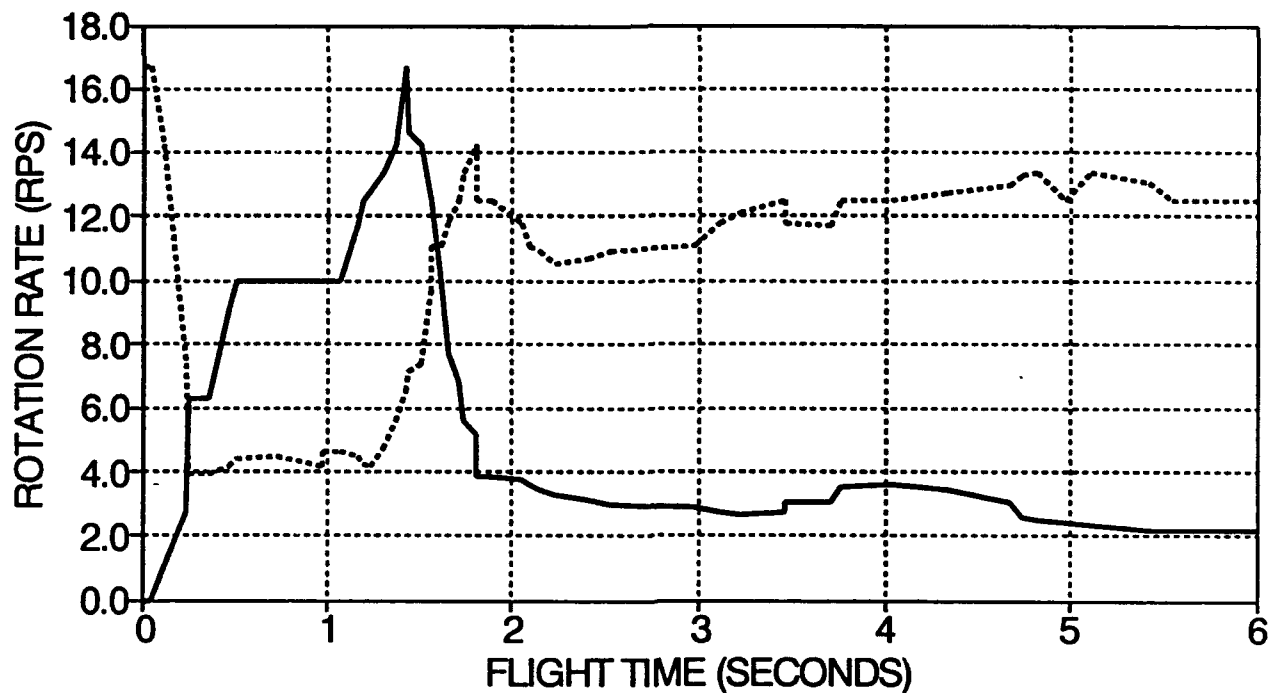
ALTITUDE VS TIME

Figure 43. Altitude Determined From the Pressure Transducer, Compared With Altitude From the Tracking Radars, as a Function of Time for the REFS Flight on 5 Nov 91 From WFF Pressure has been converted to altitude according to the US Standard Atmosphere for 30 deg. N. July.

ROTOR VS ROCKET ROTATION RATE
FIRST 6 SECONDS

Figure 44. Outer Shell (Rotor) Rotation Rate (Determined From the Optical Detectors), Compared With Vehicle Spin Rate, as a Function of Time During the First Six Seconds of the REFS Flight on 5 Nov 91 From WFF

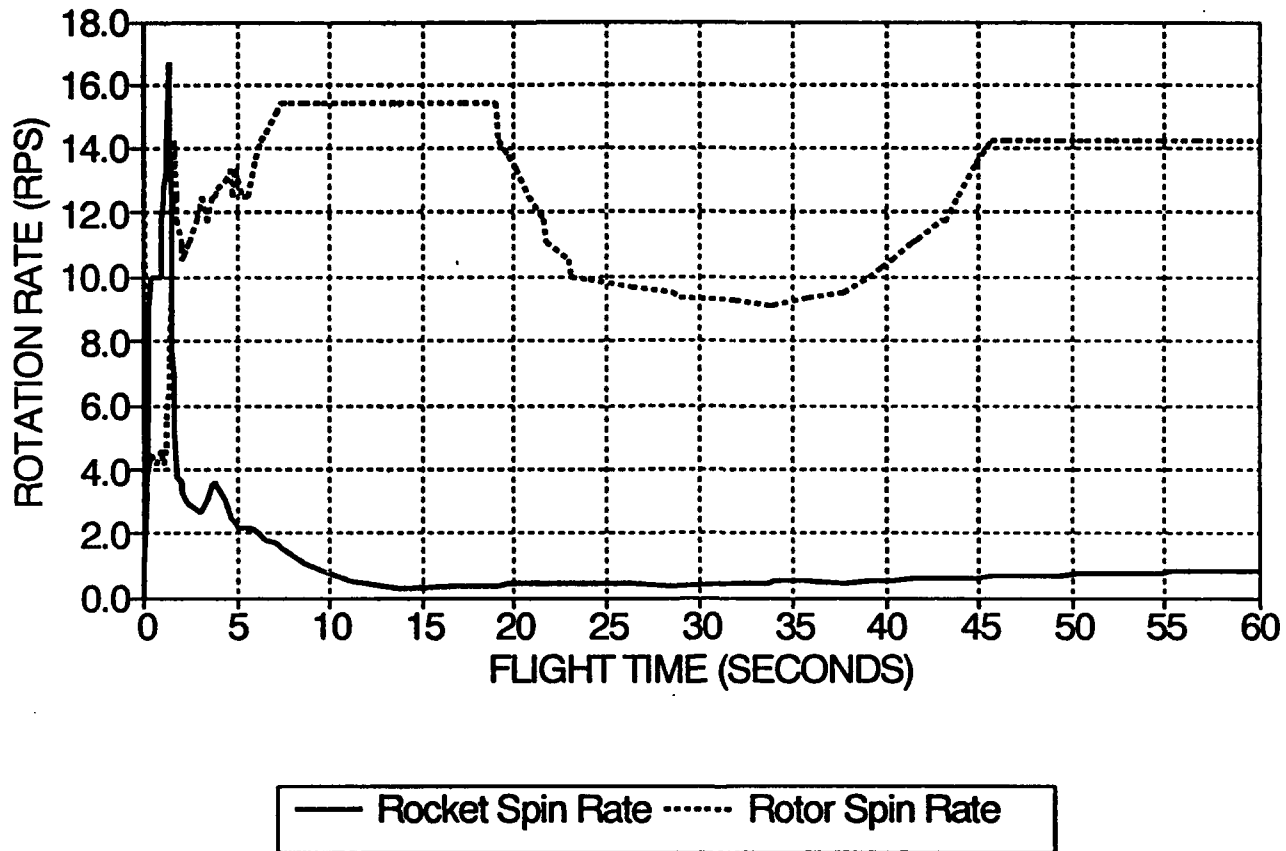# ROTOR VS ROCKET ROTATION RATE
ENTIRE FLIGHT

Figure 45. Outer Shell (Rotor) Rotation Rate (Determined From the Optical Detectors), Compared With Vehicle Spin Rate, as a Function of Time During the Entire REFS Flight on 5 Nov 91 From WFF

94

7.3 Payload Electrical Performance

7.3.1 CHARGING SYSTEM

The high voltage system encountered several problems during flight. The first problem was that the voltage levels monitored on the corona wire were approximately 1/8 of the nominal 10 kV level. Secondly, on five occasions the period between the high voltage pulses increased by exactly 1.5 times. Finally, the voltage supplied to the corona wire was nearly always negative after launch.

Part of the first problem (low voltage) was caused by the design error discussed in Section 3.7. It is thought that the remainder of this problem might be due to a partial short of the corona point to the rocket motor. The corona wire was exposed very close to the plume of the motor. It is plausible that the insulation around the corona wire partially melted and fused to the motor skin. This melting could cause a decrease in the corona voltage because of either ohmic conduction or breakdown between the wire and the motor. Further evidence of this is that the time of failure was between T+0.4 s. and T+2 s. The motor fired until T+1.5 s.

The second and third problems are difficult to explain, but both seem related to problems in the high voltage control circuitry. The timing problem might be explained by an erratic logic signal. If Q11 (see Figures 12 and 46) were stuck in the high position, then all the conditions would be met to provide charging pulses at 1.5-period intervals.
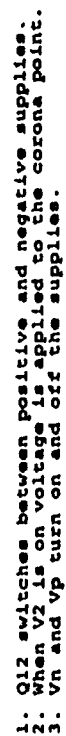
The over-abundance of negative going pulses could be explained by logic signal Q12 being stuck in the off position. If this happened, the negative supply would stay on and the relay that switches between the supplies would stay in the negative position.

7.3.2 FIELD MILLS

Figure 47 gives an overview of the entire REFS flight at 2036 UT on 5 Nov 91. The signals from three representative mills, TR, MB, and BR, are shown as the middle three traces. The signals from the optical detector with one pulse per revolution and from the high-voltage monitor are also shown for reference.

The most obvious aspect of these signals is the abrupt step-and-decay observed on TR and, even more, on MB. These transients represent a malfunction that did not occur in the laboratory and that has not been fully diagnosed. They are discussed further in Section 7.3.2.1.

Field at a given mill is indicated by a high-frequency broadening of the trace due to an increase in the amplitude of the mill signal (nominally 30 Hz). Elevated fields occurred at all the mills at three times in the data (see Figure 26). The first is prior to launch, when significant fields are indicated in spite of the fact that the weather was fair. This paradox is discussed further in Section 7.3.2.3. The second and third periods of elevated fields occur in mid flight, both before and after apogee. These events turned out to be caused by penetration of a cloud and are analyzed in Section 7.3.2.5.

95

Figure 46. High Voltage Timing Diagram
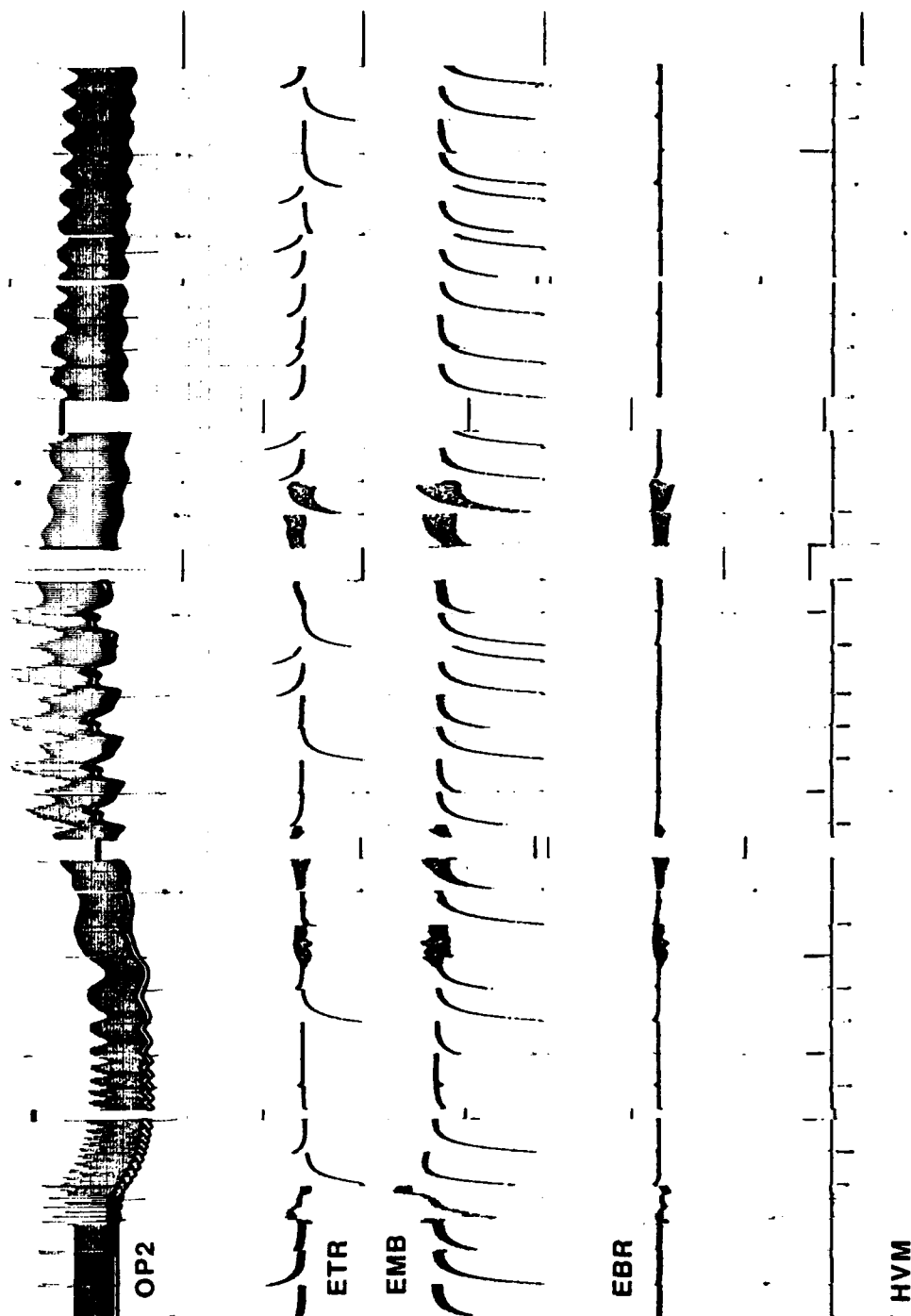
OP2

ETR

EMB

EBR

HVM

Figure 47. Overview of the Entire REFS Flight on 5 Nov 91. The top trace is from the optical detector that gives a pulse once per revolution of the outer shell. The launch is evident near the left end of this trace, where the pulses become less frequent as the shell slows down during motor burn. The middle three traces are from TR, MB, and BR, respectively. Field at a given mill is indicated by a broadening of the trace due to an increase in the amplitude of the mill signal (approximately 30 Hz). The abrupt step-and-decay on some of the mills appears to be the result of net charge being deposited on the stators by some unknown mechanism. The bottom trace is from the high-voltage monitor. The gaps in all the traces are due to telemetry dropouts. The termination of data near the right end of the traces is due to impact. Note that all the traces except MB are inverted.

7.3.2.1   Stator-Charging Events

As noted above, an abrupt step-and-decay pattern was observed on TR and, even more, on MB. Similar waveforms appeared on TL and MT as well. These transients are precisely synchronous with the energizing of the corona wire by the high-voltage relays. The waveforms first appeared on MB and MT when power was applied to the payload on the launch pad at 2018 UT. Transients began to appear on TR and TL at 2021 UT.

The cause of the transients is not understood. On MT and MB they are always negative in polarity, independent of the sign of the corona voltage, and they occur on every high-voltage application except one. The waveforms on TR and TL are also similar to each other, but they are different from those on MT and MB, being less frequent and occasionally, but not always, of positive polarity when the high voltage is positive. The transients on all four mills decay with a time constant of 310 ms --- exactly that of the charge amplifiers (see Schematics 1, 2, and 3). Thus, they appear to be the result of net charge deposited on the stators. There was condensation on the ground around the launcher, and probably on the payload, before launch due to radiative cooling and advection of warm air off the ocean. This suggests the deterioration of insulation integrity somewhere in or on the payload.

7.3.2.2   Noise Levels

The noise levels on the field-mill signals are excessive on the prototype -- typically around 6 DU peak-to-peak, which corresponds to about 3 kV/m, throughout the test flight. In an effort to determine the source of this noise, we compared the signals among the different mills in detail (see Figure 48). As the figure shows, the noise levels were similar on all eight mills and were independent of whether their respective stators were covered or uncovered. This implies that the noise was not due to fluctuations in the vehicle potential, which would have been invisible with the stators covered, and suggests that it was not due to poor grounding of the rotor, which would have produced a stronger signal on covered than on uncovered stators.

Further evidence for an internal, electronic source of noise is provided by the strong similarity of the noise waveforms among different stator channels. In fact, close examination of Figure 48 indicates that the fluctuations have not only similar frequency content but also nearly identical waveforms. The sole exception is the middle-bottom mill (MB), whose noise appears to be un-correlated with that on the other channels (see Figure 49), although its amplitude and frequency content are similar. At present, we do not have an explanation for the anomalous behavior of this one mill.
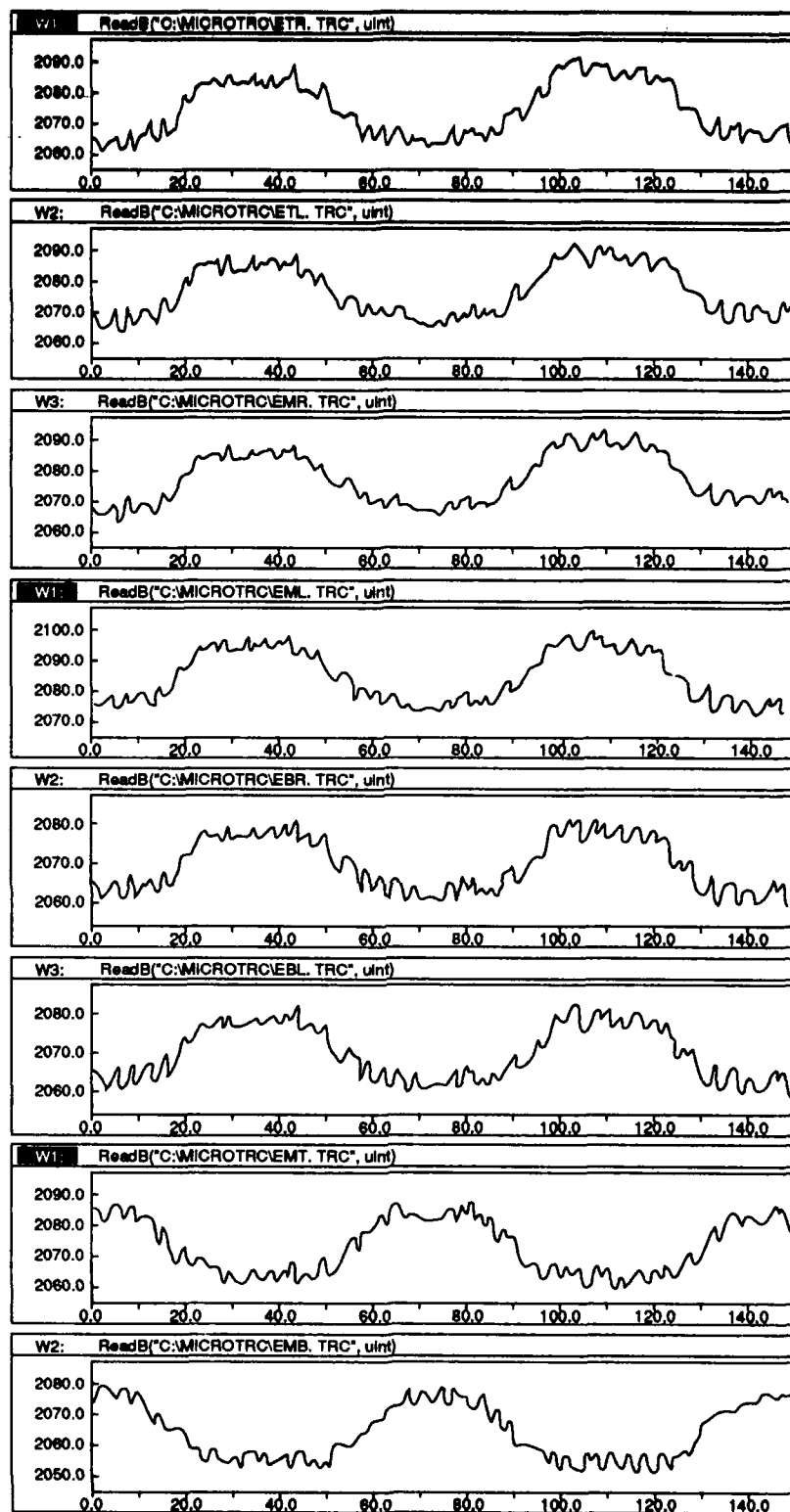
Figure 48. The Outputs of all of the Mills During the Period of Maximum Field
in the REFS Flight of 5 Nov 91. The vertical axes show the signal levels in digital
units. The horizontal axis shows relative sample number. At 2315 samples/s,
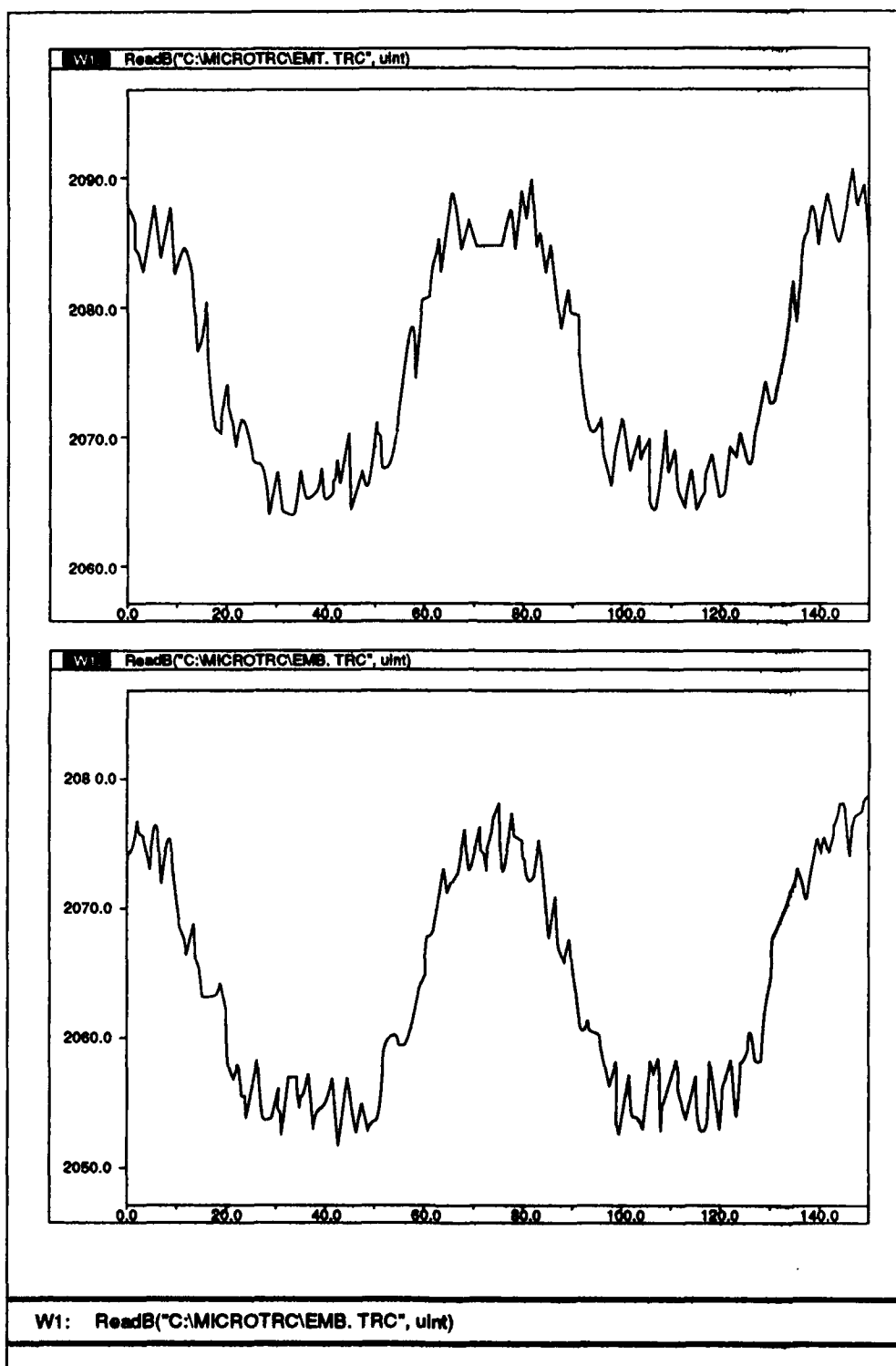the figure shows about 6.5 ms of time.

Figure 49. A Magnification of MT (top) and MB (Bottom) From Figure 48, Showing the Difference in Noise Waveforms

7.3.2.3   Fields Prior to Launch

From Figure 47 it is clear that the mills all registered significant fields when the rocket was in the launcher prior to ignition. Table 10 gives readings from each of the eight mills averaged over five full shell rotations (ten mill periods) between 20:35:59.648 and 20:35:59.886 UT. The average outputs in digital units in column 2 have been multiplied by their respective calibrations in column 4 (from column 5 of Table 7, using Eq. (6) and the geometrical value of A) to give the fields at the various stators in column 5.

Table 10. Mill Outputs, Stator Calibration, and Field Intensity

Field Mill	Output Average (DU)	Standard Deviation (DU)	Field Cal. (V/m/DU)	Field Intensity (kV/m)
TR	9.00	1.17	-489	-4.40
TL	8.54	1.16	-487	-4.16
MR	6.69	0.86	-490	-3.28
ML	6.30	0.96	-485	-3.05
BR	5.23	1.03	-484	-2.53
BL	4.90	0.91	-489	-2.40
MT	6.84	1.25	-487	-3.33
MB	6.44	0.94	-479	-3.09

The surprisingly large magnitude of the observed fields is explained by the fact that the payload is grounded when the rocket is in its launcher. Thus, the fair-weather field is enhanced considerably by the geometry of the launcher-vehicle combination (see Figure 50). The situation can be modeled crudely by the Heckman and Williams formula[34] of Eq. (14). We take R = 0.035 m, as before, and L = 2.1 m, because the entire vehicle extends above the conducting ground plane. Table 11 compares the predictions of Eq. (14) with the average fields observed at each longitudinal position on the payload, from the last column of Table 10.

Table 11. Analytic and Measured Field and Apparent E_z

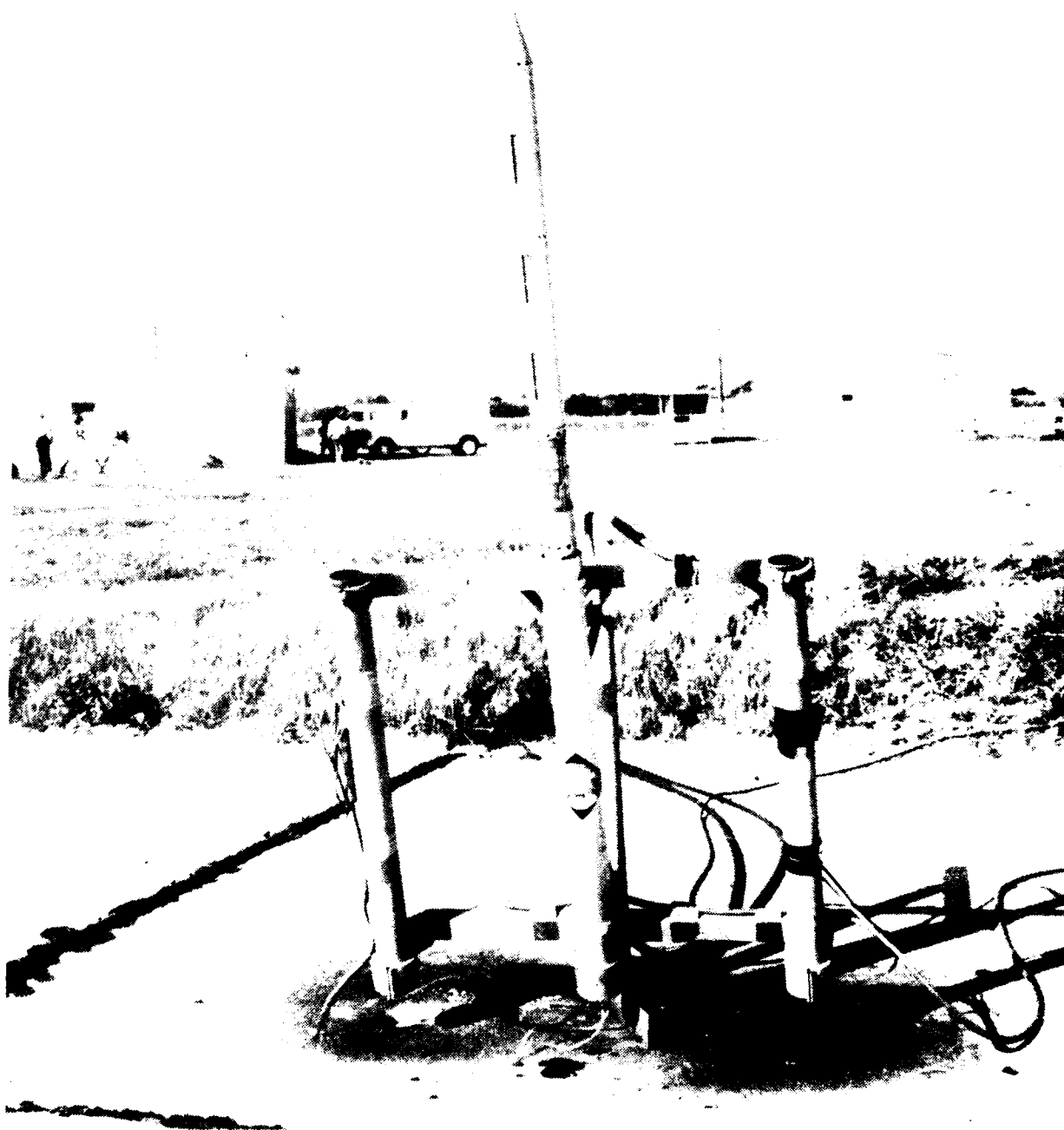| Longitudinal Position	H & W E_S/E_z	Average E_S (kV/m)	Apparent E_z (V/m)
T (z=1.80m)	12.6	-4.28	-341
M (z=1.57m)	11.0	-3.19	-291
B (z=1.37m)	9.6	-2.46	-257

Figure 50. Photograph of the REFS Vehicle in its Launch Tube at WFF

One may obtain rough estimates of the ambient vertical field (column 4) by dividing the measured fields in column 3 by the Heckman and Williams field-enhancement factors in column 2. These estimates are as consistent from position to position as can be expected in view of the complex geometry of Figure 50 and the approximations involved in Eq. (14). Although they are large for fair-weather fields, they are entirely reasonable for fields downwind from a salt-water surf zone.[35] The launch site was just tens of meters from the Atlantic Ocean, and the wind was on shore at launch time.

7.3.2.4 Response to Charging System

The response of the vehicle potential to corona pulses from the charging system was less than satisfactory. At the lowered voltages measured on the corona wire during flight, the few positive-polarity pulses that occurred had little effect. (The last "full voltage" pulse of about 4.6 kV was positive, but it occurred during motor burn so that its result was ambiguous.) Negative-polarity corona pulses generally had a noticeable effect, especially toward the end of the flight. One example is reproduced in Figure 51, which shows positive fields appearing on a representative set of mills during the high-voltage pulse and lasting for a few hundred milliseconds thereafter. Although the magnitude of the fields measured during these events was too small to read accurately, they were consistent with the expectation that positive charge was deposited on the rocket.

It was observed that the field always decayed away in a fraction of a second after the high voltage was turned off. This was not expected, since the conductivity of air is extremely low. It is assumed that net charge on the vehicle was carried away by smoke emerging from the rocket motor after burnout.

7.3.2.5 In-Flight Potential Calibration

Since the first flight of REFS occurred during fair weather, there were no measurable ambient fields with which to test the accuracy of the matrix coefficients in Eq. (15) or to calibrate the longitudinal component of the field. As noted above, artificial charging from the internal high-voltage supplies was also too weak during this flight to allow accurate calibration of the mills' potential coefficients. Fortunately, the vehicle passed through a thin altocumulus layer at about 13,000 ft altitude both before and after apogee (see Figure 47). Cloud penetration was indicated by reduced variation of the optical-detector amplitude with rocket rotation (as deduced from the magnetic detector). During both of these cloud penetrations, all the field mills indicated significant local fields due to charging of the vehicle by particle impaction. The largest fields were recorded at about 20:36:36.5 UT, on the ascending leg, when the various mills registered between -17 and -20 kV/m at the surface of the payload.

[35] Gathman, S.G., and Hoppel, W.A. (1970) Surf electrification, *J. Geophys. Res.*, **75**:4525-4529.

EMR

EML

EBR

EBL

OP2   CHART NO 0511-3042   CHART NO 0511-3042

HVM
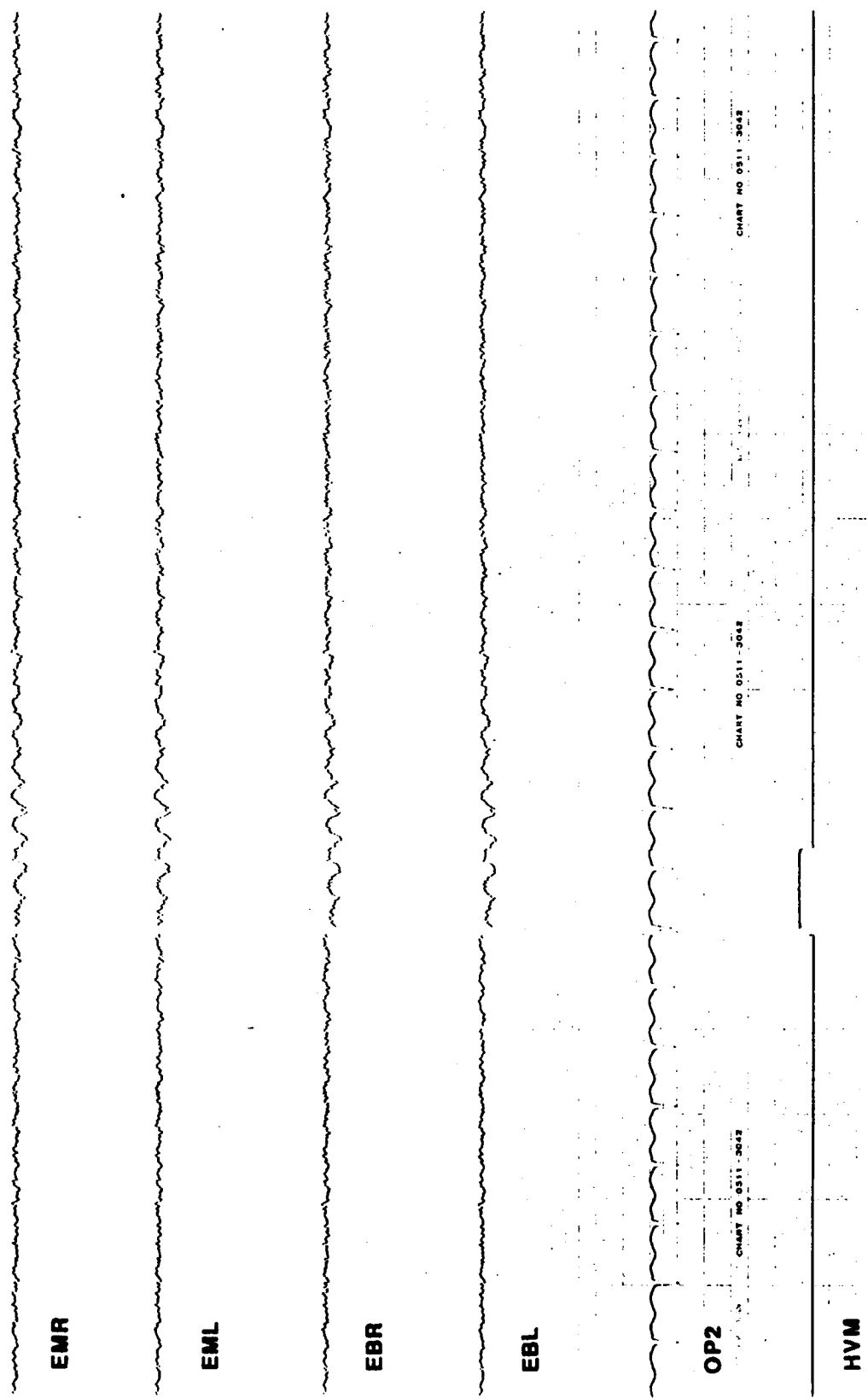
Figure 51. The Effect of a Typical Negative-polarity Corona Pulse on Four of the Field Mills. This event occurred late in the flight, when the rocket was descending through clear air below the cloud deck. The top four traces are from MR, ML, BR, and BL, respectively. The fifth trace is from the optical detector that gives one pulse per revolution of the outer shell, and the bottom trace is from the high-voltage monitor. About 1.6 seconds of data are shown.

104

Table 12 gives readings from each of the eight mills averaged over two full shell rotations (four mill periods) between 20:36:36.440 and 20:36:36.661 UT. The outputs in digital units have been multiplied, first, by the measured sensitivities of the various channels (from column 5 of Table 7) to give the charge amplitude on the stators, and second, by the inverse of the laboratory potential coefficients (from column 6 of Table 7, using Eq. (6) and the geometrical value of A) to give eight independent estimates of the apparent vehicle potential (assuming no ambient field). It is noteworthy that these potential estimates cover a range of only 4.6 percent relative to a mean of -4.33 kV, while the stator charges range 11.6 percent relative to their mean. Thus, most of the observed variation from mill to mill is explained by their laboratory response to net charge on the vehicle. This is taken as a corroboration of both the assumption that the ambient field in the cloud was negligible and the laboratory potential coefficients summarized in Eq. (15).

Table 12. Mill Outputs, Stator Charge, and Apparent Potential

Field Mill	Output (DU)	Charge (pC)	Potential (kV)
TR	39.8	-472	-4.45
TL	39.5	-466	-4.39
MR	36.4	-432	-4.35
ML	36.4	-428	-4.32
BR	36.1	-424	-4.29
BL	35.5	-421	-4.26
MT	37.2	-439	-4.32
MB	36.5	-424	-4.25

Similar, but not quite as clean, results were obtained on the upward pass through the cloud at about 20:36:14.0, when the vehicle potential peaked near -2.9 kV.

Note again that there is evidence for a mechanism that removes net charge from the vehicle. After the rocket emerges from the cloud, as indicated by resumption of variations in the light level measured by the optical detectors, the fields measured by the mills decrease rapidly toward zero (see Figure 47).

7.3.3 SUPPORTING SENSORS

7.3.3.1 Battery and Power System

The REFS power system worked as specified throughout the flight. The on-board voltage monitor showed a battery voltage of 23.8 V just prior to launch. During flight the battery voltage dropped to 22.4 V during acceleration and dropped again to 22.3 V just after apogee (see

Figure 52). These drops in battery voltage were due to the extra power required to drive the rotor spin motor (see Section 7.2), which was running slower than its optimal rate at these times. Note that the slowdown near apogee has not been explained.

The DC-DC converters appeared to operate nominally during the entire flight. There was no loss of any of the voltage supplies during flight. Though there was no direct monitoring of these converters, loss of any one converter would be apparent as a severe degradation of on-board systems.

7.3.3.2   PCM Encoder

The PCM encoder functioned well throughout the flight. Telemetry dropouts of approximately 10 ms duration were evident every 1.6 s, due to the switching of the high voltage relays. This was expected and has been discussed in Section 3.6. The large telemetry dropout that occurs at T+32 seconds cannot be attributed to the encoder. A review of the S-Band receivers' Automatic Gain Control (AGC) output shows that there was no RF power received during this dropout.

Noise levels in all of the encoder channels during flight were about 10 mV pp out of the -3 to +3 V scale. This represents a jitter of 6.8 counts out of 4096. The correlated noise waveforms on the field-mill channels discussed in Section 7.3.2.2 do not appear to match the apparently uncorrelated noise on the various support channels, however. Since all the analog signals except the field mills are sampled at different times, this lack of correlation might indicate that the base frequency of the noise is above the Nyquist sampling rate of the encoder. (The highest discernible frequency would be 1157 Hz.) Laboratory testing on other payloads shows noise levels to be approximately 6 counts with a base frequency of 300 kHz.

7.3.3.3   RF System

The RF system appeared to work nominally during the flight. The RF carrier and its modulations were received with good signal strength throughout the flight except for five instances. The most notable case was at T+32 s when the receiver AGC dropped abruptly to zero for 1.45 s and no data were received. The other dropouts were for durations of less than 0.1 s. At this point the cause of these RF dropouts is unknown. The outer shell would completely stop rotation in 1.45 s or less, if battery power were interrupted. If power were then restored, the data would show the shell "spinning up" to its nominal rotation rate. The outer shell requires approximately 1.2 s to go from 0 rps to 15 rps. The fact that the data show no "spin up" occurring implies that the power was not interrupted and the cause lies elsewhere in the system. The dropouts were probably not due to an antenna null either. The nulls out of the fore and aft end of the rocket (see Figure 16b) could not have been in the receiving antenna's beam width during this portion of the flight.
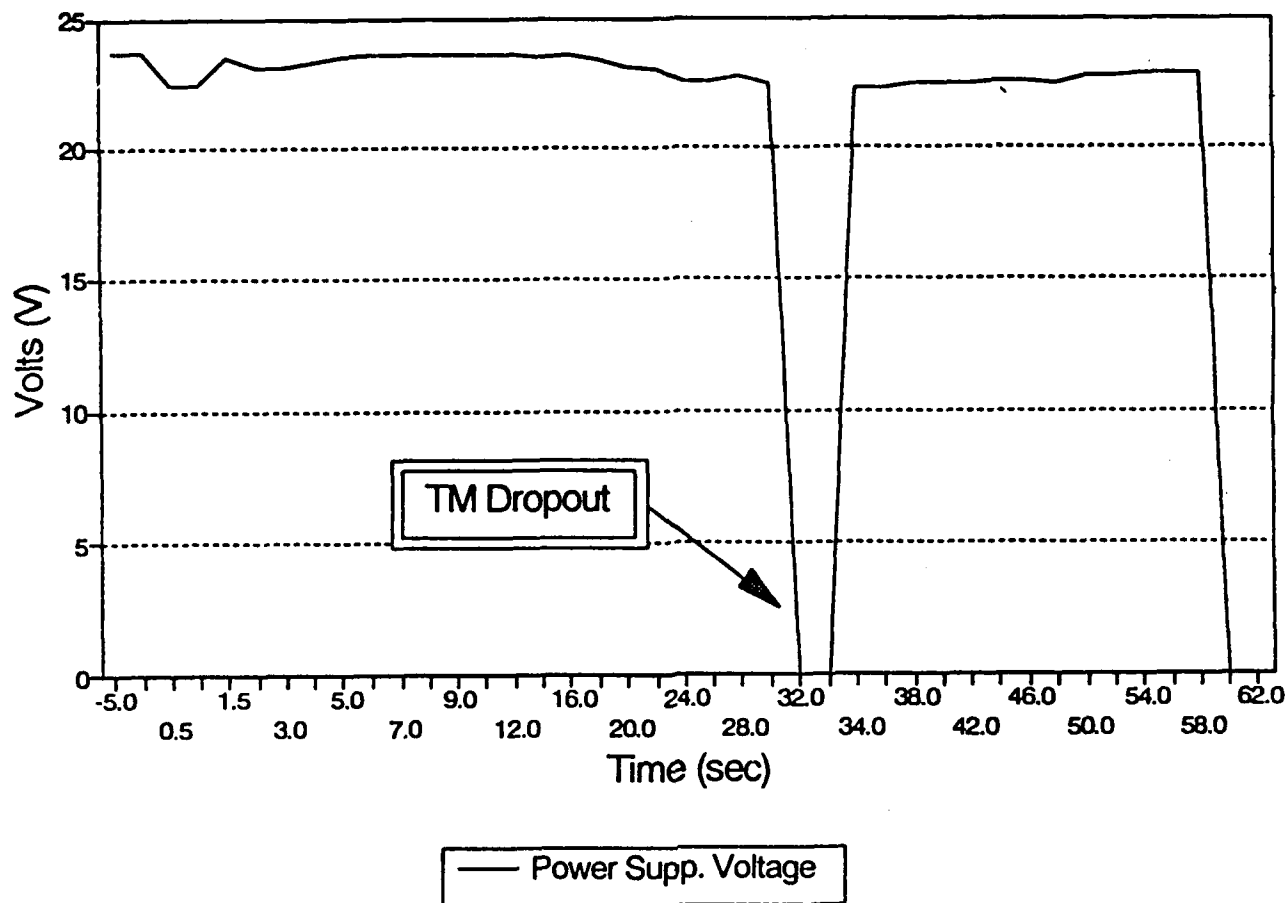
106

REFS Power Supply Voltage

Figure 52. Power-supply Voltage as a Function of Time During the Flight on 5 Nov. 91 From WFF

8. CONCLUSIONS AND FUTURE PLANS

In spite of several problems, the first flight of the REFS payload is considered a success. The flight was stable on a near-nominal trajectory. The outer shell spun properly and chopped the field so that it could be detected by the mills. Rocket rotation was indicated well by the magnetic field sensor and continued throughout the flight. The field mills themselves measured fields consistent with our laboratory calibration for net charge on the vehicle. The optical detectors proved capable of both measuring the rotor position and detecting cloud penetrations. The telemetry system performed satisfactorily.

Aside from the need to fix several minor problems before the next launch, two important lessons were learned. First, the dual-polarity high-voltage system did not operate properly in flight. Apparently, a complete re-design is required. Second, net charge bleeds off the vehicle

107

very rapidly in flight. This eliminates the need, discussed in Section 2.2, for a dual-polarity supply. Therefore, the next generation of REFS will have only a single high-voltage supply that will be directly connected to the corona emitter. A major advantage of this design simplification is the elimination of the high-voltage relays, which failed to perform as expected.

In an effort to further increase the efficiency and reliability of the corona-charging system, the emitter has been re-designed as illustrated in Figure 53. This assembly is to be slid over the motor shell and glued in place near the aft end, eliminating the insulated wire trailing near the exhaust plume. Four corona points (as opposed to the single point in the first launch) will spring out when the rocket leaves the launch tube. They will be oriented so as to produce plumes of ions that are carried between the fins and away from the vehicle by the rocket's motion through the air.

The next step in the development of REFS is to carry out some flights in high fields, thick clouds, and precipitation. Three more launches were planned for August, 1991, at KSC to test the modified design and verify proper performance under thunderstorm conditions. Unfortunately, unfavorable weather and ordnance-safety issues prevented these launches, which are now planned for July 1992.

Figure 53. Corona Point (REFS)

109
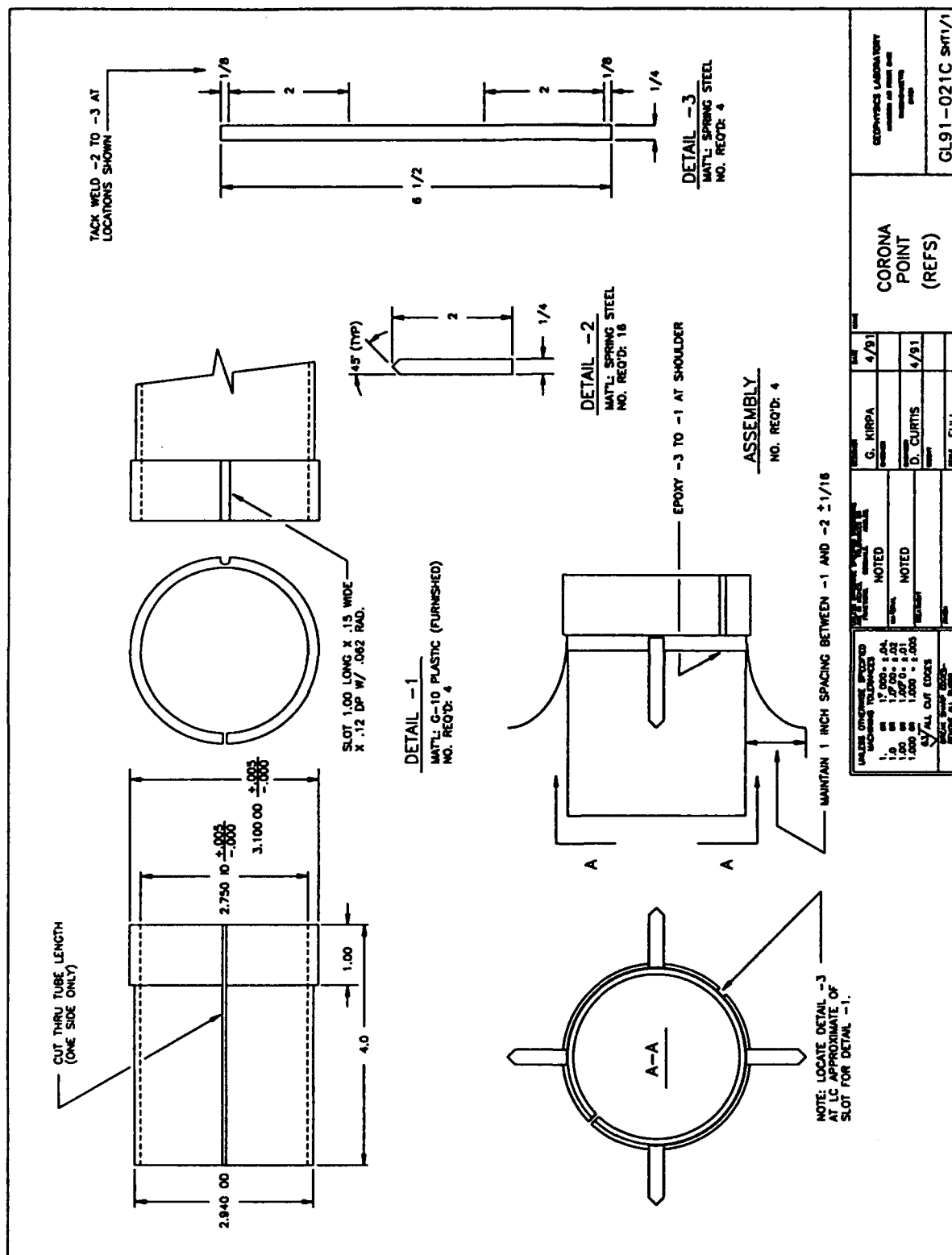
References

1. NASA Goddard Space Flight Center (1987) Atlas/Centaur-67 FLTSATCOM F-6 Investigation Board, Report, NASA Goddard Space Flight Center, Greenbelt. MD 20771, 15 July 1987.

2. Mazur, V., Fisher, B.D., and Gerlach, J.C. (1984) Lightning Strikes to an airplane in a thunderstorm, *J. Aircraft*, **21**:607-611.

3. Boulay, J.L., Moreau, J.P., Asselineau, A., and Rustan, P.L. (1988) Analysis of recent in-flight lightning measurements on different aircraft, paper presented at the International Aerospace and Ground Conference on Lightning and Static Electricity, National Oceanic and Atmospheric Administration, Oklahoma City, OK.

4. Heritage, H., (1988) *Launch vehicle lightning/atmospheric electrical constraints post-Atlas/Centaur 67 incident*, Report No. TOR-0088(3441-45)-2, The Aerospace Corporation, El Segundo, CA 90245.

5. Bailey, J., Mach, D.M., and Christian, H.J. (1990) In flight vector calibration of shutter type field mills aboard a Lear 28/29 aircraft, presented at the Fall Annual Meeting of the American Geophysical Union, Dec. 4, 1990, San Francisco, CA.

6. Mach, D.M., and Christian, H.J. (1990) Initial electrification of a Florida cumulus, presented at the Fall Annual Meeting of the American Geophysical Union, Dec. 4, 1990, San Francisco, CA.

7. Fieux, R.P., Gary, C.H., Hutzler, B.P., Eybert-Berard, A.R., Hubert, P.L., Meesters, A.C., Perroud, P.H., Hamelin, J.H., and Person, J.M. (1978) Research on artificially triggered lightning in France, *IEEE Trans. Power Appar. Syst.*, **PAS-97**:725-733.

8. Laroche, P., Eybert-Berard, A., and Barret, L. (1985) Triggered lightning flash characterization, in *Tenth International Aerospace and Ground Conference on Lightning and Static Electricity (ICOLSE)*, Paris, pp.231-239, Les Editions de Physique, Les Ulis, France.

9. Leteinturier, C., Weidman, C., and Hamelin, J. (1990) Current and electric field derivatives in triggered lightning return strokes, *J. Geophys. Res.*, **95**:811-828.

10. Idone, V.P., Orville, R.E., Hubert, P., Barret, L., and Eybert-Berard, A. (1984) Correlated observations of three triggered lightning flashes, *J. Geophys. Res.*, **89**:1385-1394.

11. Laroche, P., Boudiou, A., Eybert-Berard, A., Barret, L., Berlandis, J.P., Terrier, G., and Jafferis, W. (1989) Lightning flashes triggered in altitude by the rocket and wire technique, paper presented at the International Conference on Lightning and Static Electricity, Ministry of Defense Procurement Executive, U.K., Bath, England, Sept., 1989.

12. Mazur, V., (1988) Lightning initiation on aircraft in thunderstorms, paper presented at the 26th AIAA Meeting, Reno, NV, Jan.

13. Jackson, J.D., (1975) *Classical Electrodynamics*, John Wiley & Sons, New York.

14. Standler, R.B., and Winn, W.P. (1979) Effects of coronae on electric fields beneath thunderstorms, *Quart. J. Roy. Met. Soc.*, **105**:285-302.

15. Thayer, J.S., Nanevics, J.E., and Giori, K.L. (1989) *Triggering of lightning by launch vehicles: determination of the ambient field vehicle enhancement factors*, SRI International, Menlo Park, CA 94025.

16. Anderson, R.V., and Bailey, J.C. (1987) *Vector electric fields measured in a lightning environment*, Memorandum Report 5899, Naval Research Laboratory, Washington, DC 20375.

17. Laroche, P., Delannoy, A., and Le Court de Beru, H. (1989) Electrostatic field conditions on an aircraft stricken by lightning, paper presented at the International Conference on Lightning and Static Electricity, Ministry of Defense Procurement Executive, U.K., Bath, England, Sept.

18. Latham, D.J., (1974) *Atmospheric Electrical Effects of an on Tethered Balloon Systems*, Report 2176, Advanced Research Projects Agency, Arlington, Va. 22209.

19. Jonsson, H.H., (1990) Possible errors in electrical measurements made in thunderclouds with balloon-borne instrumentation, submitted to *J. Geophys. Res.*

20. Winn, W.P., Schwede, G.W., and Moore, C.B. (1974) Measurements of electric fields in thunderclouds, *J. Geophys. Res.*, **79**:1761-1767.

21. Ruhnke, L.H., (1971) *A Rocket Borne Instrument to Measure Electric Fields Inside Electrified Clouds*, NOAA/ERL, Boulder, CO.

22. Idone, V.P. and Orville, R.E. (1988) Channel tortuosity variation in Florida triggered lightning, *Geophys. Res. Lett.*, **15**:645-648.

23. Laroche, P., Eybert-Berard, A., Barret, L., Berlandis, J.P. (1988) Observations of preliminary discharges initiating flashes triggered by the rocket and wire technique, paper presented at the 8th International Conference on Lightning and Atmospheric Electricity, National Science Research Council, Uppsala, Sweden.

24. Kositsky, J., Giori, K.L., Maffione, R.A., Cronin, D.H., Nanevicz, J.E., and Harris-Hobbs, R. (1991) *Airborne Field Mill (ABFM) System Calibration Report*, Project 1449, SRI International, Menlo Park, CA.

25. Jones, J.J., (1990) Electric charge acquired by airplanes penetrating thunderstorms, *J. Geophys. Res.*, **95**:16,589-16,600.

26. Bailey, J.C., and Anderson, R.V. (1987) *Experimental Calibration of a Vector Electric Field Meter Measurement System on an Aircraft*, Memorandum Report 5900, Naval Research Laboratory, Washington, DC.

27. Laroche, P., (1986) Airborne measurements of electrical atmospheric field produced by convective clouds, *Rev. Phys. Appl*, **21**:809-815.

28. Nielsen, J.N., (1960) *Missile Aerodynamics*, McGraw-Hill Book Company, Inc., New York.

29. AVCO, (1974) *MASS Program User's Manual*, prepared for NASA Goddard Space Flight Center, Greenbelt, MD, under Contract NAS5-23231, by AVCO Systems Division, Maryland Operations, Seabrook MD.

30. Gathman, S.G. (1968) Guarded double field meter, *Rev. Sci. Instm.*, **39**:43-⟨⟩.

31. Moore, C.B. (1983) Improved configurations of lightning rods and air terminals, *J. Franklin Inst.*, **315**:61-65.

32. Smythe, W.R. (1968) *Static and Dynamic Electricity*, Third Edition, McGraw-Hill Book Company, New York.

33. Stratton, J.A. (1941) *Electromagnetic Theory*, McGraw-Hill Book Company, New York.

34. Heckman, S.J., and Williams, E.R. (1989) Corona envelopes and lightning currents, *J. Geophys. Res.*, **94**:13, 287-13, 294.

35. Gathman, S.G., and Hoppel, W.A. (1970) Surf electrification, *J. Geophys. Res.*, **75**:4525-4529.